A Comparative Study on the Performance of Bio-inspired Slippery Lubricant Impregnated and Superhydrophobic surfaces in Droplet Impact and Shedding

Firoozeh Yeganehdoust

A Thesis

in

The Department

of

Mechanical, Industrial and Aerospace Engineering

Presented in Partial Fulfillment of the Requirements

for the Degree of

Doctor of Philosophy (Mechanical Engineering) at

Concordia University

Montréal, Québec, Canada

May 2021

CONCORDIA UNIVERSITY

School of Graduate Studies

This is to certify that the thesis prepared,

By: **Firoozeh Yeganehdoust**

Entitled: **A Comparative Study on the Performance of Bio-inspired Slippery Lubricant Impregnated and Superhydrophobic surfaces in Droplet Impact and Shedding**

and submitted in partial fulfillment of the requirements for the degree of

Doctor of Philosophy (Mechanical Engineering)

complies with the regulations of this University and meets the accepted standards with respect to originality and quality.

Signed by the Final Examining Committee:

_____ Chair
Dr. Anjan Bhowmick

_____ External Examiner
Dr. Mina Hoorfar

_____ External to the Program
Dr. Alex De Visscher

_____ Examiner
Dr. Christian Moreau

_____ Examiner
Dr. Marius Paraschivoiu

_____ Thesis Supervisor(s)
Dr. Ali Dolatabadi

_____
Dr. Ida Karimfazli

Approved by _____
Martin D. Pugh, Chair
Department of Mechanical, Industrial and Aerospace Engineering

May6^{th}, 2021
Date of Defence

_____
Mourad Debbabi, Dean
Gina Cody School of Engineering and Computer Science

Abstract

A Comparative Study on the Performance of Bio-inspired Slippery Lubricant Impregnated and Superhydrophobic surfaces in Droplet Impact and Shedding

Firoozeh Yeganehdoust, Ph.D.

Concordia University, 2021

The development of robust surfaces that repel liquid droplets has a broad impact on enhancing surfaces in several applications of anti-icing/fogging, anti-biofouling, and anti-dewing. Despite high repellency features in superhydrophobic surfaces, these surfaces may be ineffective when they are used in harsh environments. Inspiration from the natural non-wetting behavior of slippery surfaces of the pitcher plant has led to the development of slippery lubricant impregnated surfaces (SLIPS/LIS). They are designed by creating micro/nano-structured surfaces that are infused with a low surface tension lubricant which can enhance droplet mobility for a wide range of liquids with low surface tension properties. Designing slippery lubricant impregnated surfaces is still ongoing research as it involves several parameters. The physics of the impact and shedding of the liquid droplet on slippery surfaces remains elusive. In this regard, both experimental and numerical tools have been used in this work to explore the associated physics in slippery surfaces and their advantages and disadvantages compared to superhydrophobic surfaces.

The first goal was to evaluate the effect of an immiscible lubricant with different thicknesses on the impact of a millimeter-sized water droplet for different impact velocities. A three-phase flow numerical simulation based on a finite volume solution coupled with a volume of fluid method has been implemented. The numerical model showed that the droplet spontaneous bouncing occurred due to the air entrapment because of the deformation in both droplet and liquid film surface in which the details of the gas layer thickness and dynamics of fluid motions were illustrated. It is observed that liquid film surfaces can enhance the probability of droplet spontaneous bouncing.

The performance of superhydrophobic surfaces might fail their functions for micro-scale droplets as both

the micro-structured surfaces and droplets are on the same scale. Thus, the anti-wetting performance of slippery lubricant impregnated surfaces compared to superhydrophobic surfaces for different surface morphologies have been numerically investigated during droplet impingement. The effect of the surface structure has been studied by considering different series of square-pillar arrays. A three-phase flow solver in conjunction with an accurate contact angle method has been implemented. It was observed that slippery surfaces with low–density micro-textured surfaces enhanced droplet mobility and repellency compared to superhydrophobic surfaces. Additionally, the quantitative results indicated that the droplet pinning decreased significantly compared to superhydrophobic surfaces.

In order to assess the mobility of droplets under the effect of air shear flow on slippery surfaces and superhydrophobic surfaces, an experimental study in conjunction with a numerical model has been conducted. It is observed that the hydrodynamics of droplet motion is completely different on superhydrophobic compared to slippery surfaces. The wetting length and position of a droplet on all surfaces have been measured. Although similar trends are observed in quantitative measurements for slippery surfaces, the speed of droplets is greatly affected by the lubricant properties. A numerical simulation based on the VOF method coupled with the Large Eddy Simulation turbulent model in conjunction with the dynamic contact angle method has been used. A developed boundary condition is also implemented to consider the effect of lubricant on slippery surfaces. The numerical simulations are compared with the experimental study to provide further information on the experimental results.

Contribution of Authors

This thesis is prepared in manuscript format. Chapters 1 and 5 are the introduction and conclusion of the thesis, respectively. The rest of the chapters are reprinted from the papers published or submitted to scientific journals. The first author of these manuscripts is Ms. Firoozeh Yeganehdoust who is the author of this thesis and the manuscripts. She has implemented and developed numerical simulations and post-processed the results. She was also responsible for designing, conducting, and post-processing the experimental results. The paper titles, journal names, volume numbers, page numbers, and the contribution of the co-authors will be given in detail as follows.

Chapter 2 entitled "A Numerical Analysis of Air Entrapment during Droplet Impact on an Immiscible Liquid Film" is a published paper in the International Journal of Multiphase Flow, Volume 124, pages 103175, 2020 (`https://doi.org/10.1016/j.ijmultiphaseflow.2019.103175`). This work has been co-authored by Dr. Reza Attarzadeh, Prof. Ida Karimfazli, and Prof. Ali Dolatabadi. Dr. Attarzadeh advised with the methodology and analysis. Prof. Ida Karimfazli and Prof. Ali Dolatabadi are the supervisors of the project.

Chapter 3 entitled "A Comparison of Bioinspired Slippery and Superhydrophobic Surfaces: Micro-droplet Impact" is a published paper in Physics of Fluids Journal, volume 33, pages 022105, 2021 (Reproduced from Yeganehdoust, F., Attarzadeh, R., Dolatabadi, A., Karimfazli, I. (2021). A comparison of bioinspired slippery and superhydrophobic surfaces: Micro-droplet impact. Physics of Fluids, 33(2), 022105, with the permission of AIP Publishing). This work has been co-authored by Dr. Reza Attarzadeh, Prof. Ali Dolatabadi, and Prof. Ida Karimfazli. Dr. Attarzadeh advised in the methodology of simulations. Prof. Ida Karimfazli and Prof. Ali Dolatabadi are the research supervisors.

Chapter 4 entitled "Droplet Mobility on Slippery Lubricant Impregnated and Superhydrophobic Surfaces under the Effect of Air Shear Flow" is an accepted paper in the Langmuir Journal ("Reproduced

(or'Reproduced in part') with permission from (Yeganehdoust F., Amer A., Sharifi N., Karimfazli I., Dolatabadi A., Droplet Mobility on Slippery Lubricant Impregnated and Superhydrophobic Surfaces under the Effect of Air Shear Flow, Langmuir, https://doi.org/10.1021/acs.langmuir.1c00726) Copyright 2021 American Chemical Society.") This work has been co-authored by Mr. Adham Amer, Dr. Navid Sharifi, Prof. Ida Karimfazli, and Prof. Ali Dolatabadi. Mr. Adham Amer helped the first author with conducting the experimental work. Dr. Navid Sharifi helped with the preparation of samples and advised the experimental work. Prof. Ida Karimfazli and Prof. Ali Dolatabadi are the supervisors of the project.

Acknowledgments

Many thanks to my supervisors, Prof. Ali Dolatabadi and Prof. Ida Karimfazli for their support and guidance throughout all stages of the work. Without their continuous encouragement, the research would not be possible. I would also like to express my gratitude to my committee members for their helpful comments and suggestions to improve the thesis. Many thanks to my colleagues Reza Attarzadeh, Adham Amer, and Navid Sharifi for their suggestions and scientific collaborations. Finally, I would like to thank my parents, family and friends (especially at the TSMF lab) for their unconditional support.

Thank you, Lord, for being with me every step of the way, especially in the storms of life.

"As one journey ends, Another begins..."

Dedication

To my wonderful mother, Nasrin,for her measureless support and constant love ;

And my husband, Mani;

Contents

List of Figures

List of Tables

Chapter 1

Introduction

1.1 Background

Extensive research has been recently directed toward engineering and designing surfaces to enhance liquid repellency i.e. hydro/oleo-phobic surfaces. These surfaces have been used in several industrial applications, such as self-cleaning [1, 2] and anti-biofouling coatings [3–5], anti-fogging/icing [6–9], microfluidics [10–12] and to enhanced heat transfer [13, 14]. Researchers have been inspired by the structures and materials of biological surfaces such as butterfly wings, lotus leaf, water strider leg, Nepenthe's leaf, etc. For instance, water striders can stand and move quickly on water because of their remarkable non-wetting legs due to the surface tension effect by secreted wax [15, 16]. Thus, bio-inspired surfaces can generate properties such as low adhesion and liquid repellency features.

In superhydrophobic surfaces (SHSs), the fabrication of liquid-repellent surfaces has been imitated by the micro/nano-structures of lotus leaves [17] (Figure 1.1a). These surfaces can hold air pockets underneath a droplet placing on it and results in the forming of spherical shape droplet that reduces the adhesion between the liquid and solid surface. Besides the hierarchical roughness in SHS, the high droplet mobility is due to the chemical hydrophobic material of surfaces [18]. In parallel with the superhydrophobic surfaces, other recent non–wetting surfaces have been developed to enable repelling various liquids that are inspired by the pitcher plant (Figure 1.1b), known as slippery lubricant impregnate surfaces (SLIPS/LIS) [19]. Interestingly, the inner surface of these plants is in micro-structure patterns where extremely wettable by a nectar wax which results in slippery liquid surfaces and insects able to slide easily within the plants. Slippery lubricant impregnate surfaces are composed of lubricant which is locked within the micro/nano-structure

surfaces. Thus, as most of the working liquids are immiscible with the lubricant, slippery surfaces can repel or slide various liquids. Researchers have been analyzed SLIPS design in various applications such as anti-biofouling [3], anti-icing [7, 8], and drag reduction [20].

Figure 1.1: (a) Lotus leaves and SEM image of its surface structure [21] (b) pitcher plant

There has been extensive research on the non-wetting superhydrophobic surfaces including the fundamental physics and design of surfaces. However, there have been still issues with the collapse of air pockets or droplet pinning in SHSs [5, 22, 23]. The pinning might occur because of high droplet impact velocity, or under high-pressure conditions or the droplets might be in the scale of the textured surface. Additionally, despite their ice-phobic behavior in frost-free environments [24, 25], superhydrophobic surfaces may induce ice nucleation at high humidity conditions at even a faster rate compared to smooth surfaces. This is due to their higher surface area and thus larger nucleation sites, which result in droplet condensation [23, 26, 27].

It has been proved that slippery surfaces might overcome some limitations asspciated with SHS [28, 29], however, there are still complications in designing and understanding the physics of liquid droplets in contact with the slippery surfaces. As the basic configuration of slippery lubricant impregnated surfaces involve solid/lubricant/immiscible working liquid/air, it makes SLIPS more complicated to analyze compared to superhydrophobic surfaces. There are still questions regarding the SLIPS performance compared to SHS such as how the lubricant can play the role in the SLIPS? how the structure of the surface can affect droplet hydrodynamics? how the SLIPS can be effective compared to SHS in case of droplet impact or shedding situations? This dissertation aims to answer some of the questions outlined above and to explore and compare the fundamental physics underlying these low adhesion surfaces.

1.2 Fundamentals of surface wettability

Once a droplet is in contact with a solid surface, several parameters such as surface tension, capillary length, surface texture, and its chemistry can affect droplet formation and its dynamics. Specifically for small droplets, the interfacial tension forces can be dominant compared to all other parameters. When a liquid droplet is placed on a surface, depending on the capillary length, it can either shape as a spherical droplet (sessile droplet) or it might spread on the surface. Once the radius of a droplet becomes less than the capillary length $\kappa^{-1} = \sqrt{\sigma/\rho g}$, where σ and ρ are the surface tension coefficient and droplet density, the shape of the droplet is governed by the interfacial tension force whereas the gravitational force becomes negligible (for a water droplet condition, $\kappa^{-1} = 2.7\ mm$). The wetting behavior of a surface is conventionally quantified by the equilibrium contact angle which is defined as a result of the interaction between all three interfacial tensions in the x-direction (along the surface) determining by Young's equation, $\cos\theta_e = \frac{\sigma_{sg} - \sigma_{ls}}{\sigma_{lg}}$, where σ_{sg}, σ_{sl} and σ_{lv} are the surface tension between solid-gas, liquid-gas, and liquid-gas (as shown in Figure 1.2a). If the surface energy is high, a droplet spreads on the surface and forms a contact angle less than 90°, such a surface is defined as a hydrophilic surface. On extremely low-energy surfaces, known as superhydrophobic surface or a water-repellent surface, a droplet tends to keep its spherical shape and forms an angle greater than 150°. It is worth mentioning that surface energy is the energy needed for bringing molecules out from the bulk to the surface. According to Young's equation, lower surface energy leads to higher contact angles.

Surface patterning or surface roughness is also a substantial contributing property that can affect the wetting behavior of the surface. Thus, when a droplet comes in contact with a rough surface, there are two distinct outcomes: a Wenzel state or a Cassie–Baxter state. In the Wenzel state, the droplet penetrates the roughness and forms a higher apparent contact angle (Figure 1.2b). The apparent contact angle of a Wenzel state is defined by taking into account the surface roughness and modifying Young's equation, $\cos\theta_w = R_w \cos\theta_e$, where θ_w and θ_e are the apparent contact angle and contact angle on a smooth surface (Young's equation) and R_w is the roughness factor which is the ratio of an actual contact area of the solid-liquid interface divided by its projection on a flat surface. Thus, surface roughness enhances the philic/phobic behavior. Despite the Wenzel state, air pockets may trap between the liquid and solid surface. In a Cassie–Baxter state, the droplet remains on top of the surface asperities and forms a higher apparent contact angle (Figure 1.2c). In this case, the effect of the heterogeneous interface is integrated into the

calculation of contact angle. The apparent contact angle for a Cassie–Baxter state, θ_{CB}, can be defined as $\cos\theta_{CB} = \phi_s(\cos\theta_e + 1) - 1$, where ϕ_s is the solid-liquid fraction. Thus, the contact area between liquid and solid is reduced compared to a flat surface.

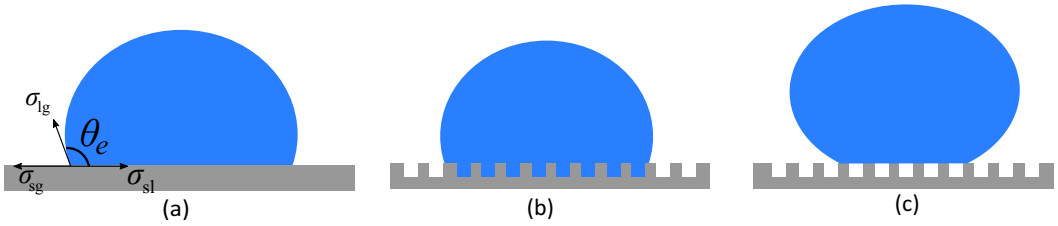

Figure 1.2: Droplet on (a) a flat solid surface-in an equilibrium state, (b) rough surface-Wenzel state and (c) surface roughness- Cassie-Baxter state

A droplet can be transited from a Cassie-Baxter to Wenzel state if enough activation energy is provided. For instance, by applying pressure to a droplet or if the liquid droplet has low surface tensions. Regarding the surface free energy equations, the transition occurs when the contact angle reaches the critical value. If the droplet wants to remain in the Cassie-Baxter state, its energy must be lower than in Wenzel state, $\Delta E_w > \Delta E_{CB}$. In other words, the contact angle must be greater than the critical value, $\cos\theta_e > \frac{(\phi_s - 1)}{R_w - \phi_s}$.

Besides the equilibrium apparent contact angle, another wetting parameter known as contact angle hysteresis (CAH) is required to describe the surface properties. A high contact angle cannot be alone results in high droplet mobility and CAH is required to be small. Contact angle hysteresis is affected by surface roughness and chemical heterogeneity. CAH is defined based on the difference between the advancing (θ_A) and receding contact angle (θ_R). Advancing and receding contact angle is originally determined by the angle of a droplet when starts to condensate (until it advances with a constant contact angle) and evaporate (until it recedes with a constant CA), respectively. Similarly, the CAH can be obtained experimentally. Two standard methods have been used to measure the θ_A and θ_R (as shown in Figure 1.2); (a) by adding and withdrawing a droplet through a syringe, in which the liquid is pumping at a very slow rate (θ_A) and then the droplet is slowly withdrawn (θ_R), as shown in Figure 1.3a and, (b) by placing a droplet on a substrate and tilt the surface until at a certain inclination angle, the contact line starts depinning and the droplet deform from a spherical cap to a tear shape. Prior to the detachment, θ_A and θ_R are denoted by the leading edge and the trailing edge of a droplet, as shown in Figure 1.3b. Then, CAH is measured by taking the difference between the advancing and receding angles.

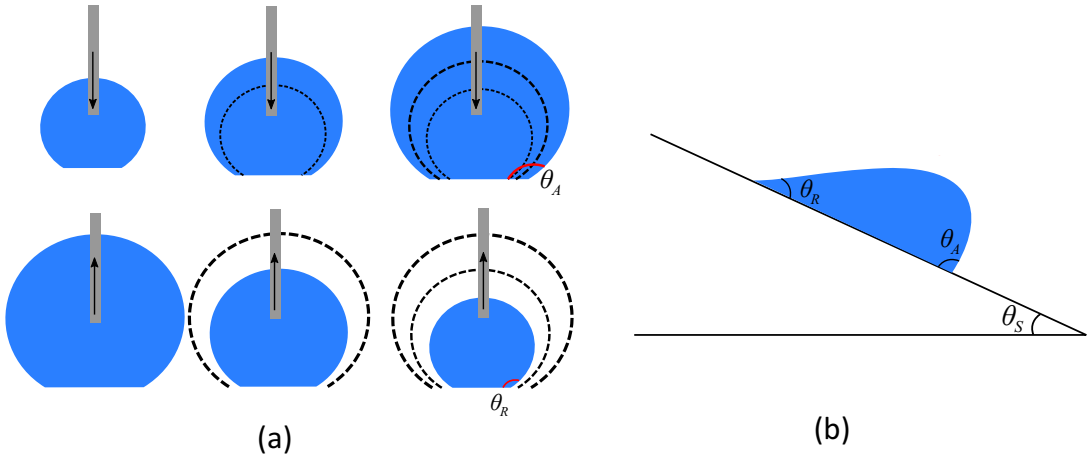

Figure 1.3: Contact angle hysteresis measurements by (a) needle method and (b) tilting method

Another important wetting parameter especially in slippery lubricant impregnated surfaces where a working liquid is in contact with an immiscible lubricant is the spreading coefficient (S). This parameter indicates whether the oil is able to completely wet the surface or not. Additionally, it implies whether the droplet is cloaked by an immiscible lubricant or not. The spreading coefficient shows the ability of a liquid to spread on a solid surface or another immiscible liquid, which is defined as the difference between the adhesion work and cohesion work of two phases. For a complete spreading of a liquid on a solid surface, the liquid must be energetically favorable to be in contact with the solid and air, rather than the air with solid. Thus, the interfacial tensions results in $\sigma_{la} + \sigma_{ls} < \sigma_{sa}$. It can be indicated by the spreading coefficient, $S = \sigma_{la} + \sigma_{ls} < \sigma_{sa}$, in which for $S < 0$, the liquid tends to spread on a surface. Accordingly, it can be deduced the water droplet cloaking by the oil layer based on the spreading coefficient, $S_{ow(a)} = \sigma_{wa} - \sigma_{wo} - \sigma_{oa}$. If the $S > 0$, it implies that the oil cloaks the water droplet.

When a droplet is deposited on SLIPS, it would be either in Wenzel or Cassie-Baxter state while the lubricant can be in encapsulated or impregnated condition, as shown in Figure 1.4.

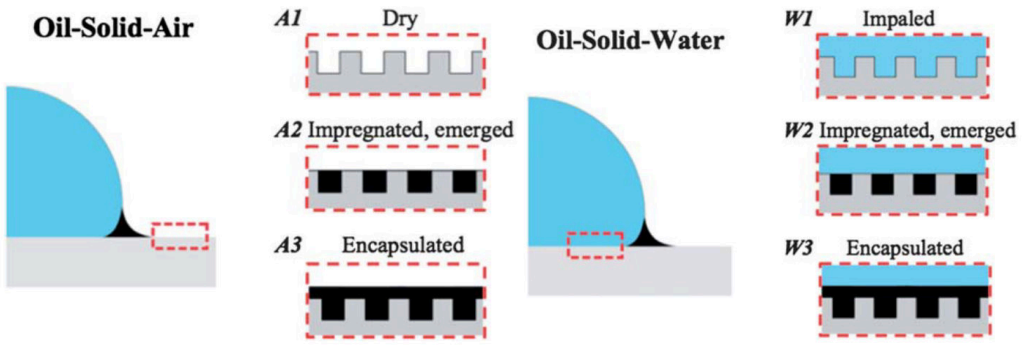

Figure 1.4: Schematics of possible wetting states outside and underneath a droplet [30]

Considering the liquids energies with the surface and their interactions, 12 states have been found by Smith et al. [30] that indicated which states are more favorable in SLIPS. Total interface energy per unit area is described in Table 1.1 where $A1$ is the energy of the system which depends only on surface roughness. $A2$ is the energy of a system where the oil is impregnated within the surface (Hemi-wicked by the oil) and the tops of the pillars are exposed to the air. $A3$ indicates the energy for the encapsulated situation where it depends on both the oil-air surface tension and surface roughness. $W1$ is completely impaled within the surface and is replaced by the surrounding air. $W2$ and $W3$ are similar to $A2$ and $A3$ situations where the surrounding air is replaced by another immiscible liquid (water).

Table 1.1: The total possible interface energies for a liquid droplet on a SLIPS [30]

Oil–Solid–Air	**Oil–Solid–Water**
$E_{A1} = r\sigma_{sa}$	$E_{W1} = r\sigma_{ws}$
$E_{A2} = (r - \phi_s)\,\sigma_{os} + \phi_s\sigma_{sa} + (1 - \phi_s)\,\sigma_{oa}$	$E_{W2} = (r - \phi_s)\,\sigma_{os} + \phi_s\sigma_{ws} + (1 - \phi_s)\,\sigma_{ow}$
$E_{A3} = r\sigma_{os} + \sigma_{oa}$	$E_{W3} = r\sigma_{os} + \sigma_{ow}$

Adding the possibility of droplet cloaking to the 6 mentioned possible states, the total possible states rise to 12 states as shown in Figure 1.5 depicted by Smith et al. [30]. The high pinning effect in $A3W1$ and $A2W1$ results in the lowest droplet mobility, while the highest droplet mobility occurs for $A3W3$ where the lubricant layer is in encapsulated condition. However one of the challenges in SLIPS is to maintain the lubricant layer. It has been observed that droplets are mostly meet the tops of the pillars without displacing the oil within the substrate.

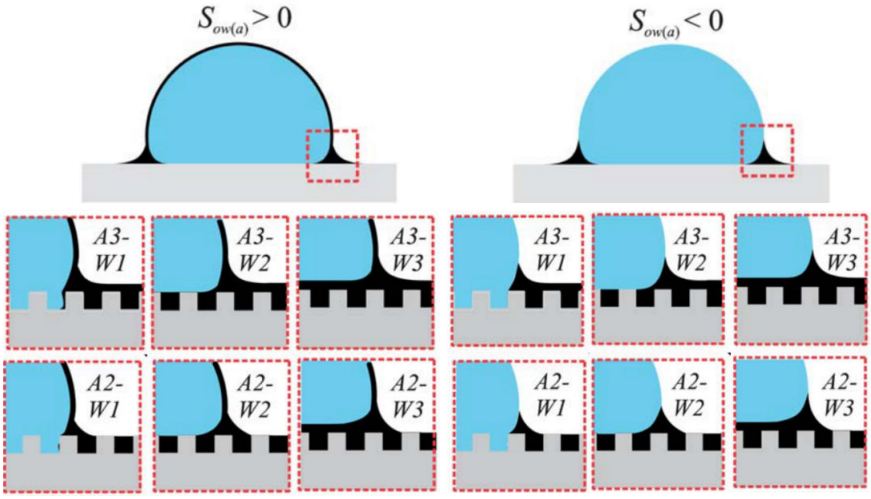

Figure 1.5: Thermodynamic stable states for SLIPS [30]

Different methods have been used in terms of coating the lubricant layer, such as spin–coating or dipping the surface within the oil liquid. It has been observed that the oil layer thickness change by the withdrawn speed and the thickness will increase as the speed increases, according to Landau – Levich – Derjaguin (LLD) equation. Based on this method, the thickness can be obtained as $h_o \approx 0.94\kappa^{-1}Ca^{2/3}$ for a flat surface, where Capillary number is $Ca = \frac{\mu V}{\sigma}$. Moreover, a ridge of lubricant may occur around the droplet during contact between the lubricant and droplet [30–32], as schematically shown in Figure 1.6 which is an important issue in droplet mobility since most viscous dissipation occurs in this region.

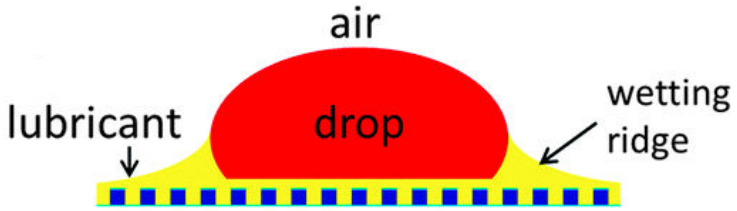

Figure 1.6: Droplet resting on SLIPS surrounded by a wetting ridge [33]

The wetting ridge might rise complications in contact angle measurement and Young's equation can no longer predict the contact angle. One way to find the contact angle is to extrapolate the apparent SLIPS contact angle by fitting a circle to droplet where it fits surface intersect which is introduced by Guan et al. [34]. Semprebon et al. [35] demonstrated a correction to Young's equation and derive a closed-form expression for predicting the contact angle of the vanishing wetting ridge.

1.3 Droplet impact dynamics

1.3.1 Droplet impact on solid surfaces

Droplet impact has been a topic of interest for a long time due to its countless applications such as inkjet technology [36], fuel injection, spray coating and cooling systems [37, 38]. When a droplet impinges the surface, different scenarios may occur as shown in Figure 1.7 [38, 39]. These different behaviors mainly depend on the liquid and surface properties and their initial conditions such as droplet size and impact velocity.

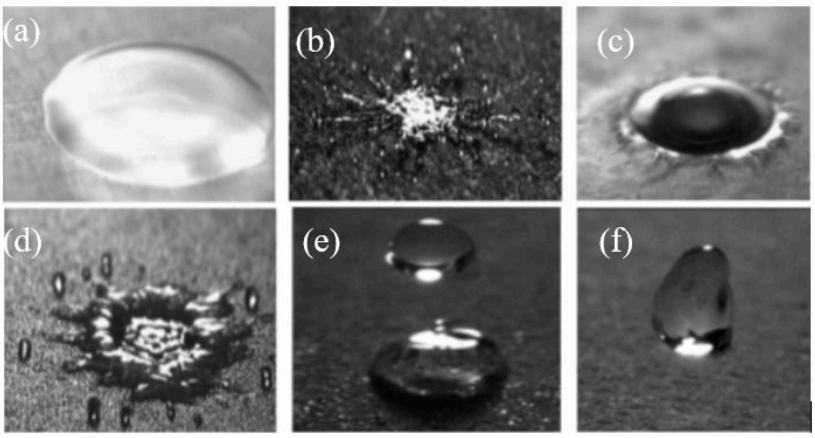

Figure 1.7: Droplet impact outcome on a solid surface (a) deposition (b) prompt splash (c) corona splash (d) receding break-up (e) partial rebound (f) complete rebound [38]

Various non-dimensional numbers have been introduced that characterize the relative magnitude of forces acting on the droplet during impact. These dimensionless numbers represent forces corresponding to droplet impact dynamics such as Weber number($We = \frac{\rho V^2 D}{\sigma}$), Reynolds number ($Re = \frac{\rho V D}{\mu}$) and Ohnesorge number ($Oh = \frac{\mu}{\sqrt{\rho \sigma D}}$). In the deposition, droplet spreads and remains on a solid surface without any breakup which mostly happens when the surface has no asperities that might affect the deposition process. When the droplet impact velocity is high and the surface has a roughness, prompt splash might occur which leads to generating many small droplets. In the corona splash, small droplets generate around the rim after droplet collision, which mostly occurs when the droplet impact with high velocity on a smooth surface. The receding breakup occurs when the receding contact angle decreases while the liquid retracts from the maximum spreading. Thus, some small droplets are left behind during the receding stage. Partial and complete rebound is mostly attributed to the impact on a superhydrophobic substrate which is due to the

patterns of surface roughness which results in air entrapment and exhibits high contact angles. If the droplet impact velocity reaches a high value, the air traps might collapse and the droplet can penetrate within the asperities and partial rebound can occur.

Several studies have been investigated droplets bouncing on surfaces without the use of external forces. The thickness of the air layer trapped between the droplet and the solid (which is typically on the order of micro/nano–meters) is a key parameter that has a large influence on droplet dynamics. This air layer exerts a lubrication force, which causes the droplet to bounce. It has been shown that droplets performed their bouncing process as long as the air layer sustained its action as a lubrication force [40–45]. This situation can be obtained in cases when external forces are acting on the system by vibration on liquid substrates or gradual evaporation of Leidenfrost drops on heated substrates [46]. As a droplet approaches the surface, pressure in the air gap increases, which results in bubble entrapment. Once the air gap thickness decreases, the maximum air pressure below the droplet surface increases and the area of high pressure expands. This high pressure deforms the droplet interface and causes the droplet to recoil from the surface before it makes contact.

1.3.2 Droplet impact on liquid surfaces

Droplet impact dynamics on liquid surfaces might rise the complexity of droplet impact due to the interacting dynamics of both liquids (droplet and liquid film). Further parameters such as Ohnesorge number ($Oh = \sqrt{We}/Re$) and dimensionless film thickness ($h^* = h/D_0$, where h is the initial height of liquid film) are also involved. Additionally, impact on liquid film accompanies different bubble entrapment depending on the velocity and diameter of a droplet. Depending on the liquid film thickness (thin, shallow, and deep liquid film), the droplet might bounce, coalesce with the liquid surface, or splash from the surface. There have been several studies on the impact of liquid surfaces [47, 48]. However, few studies have been dedicated to droplet impact on immiscible liquid film [45, 49, 50].

Tang et al. [50] illustrated the transition of bouncing-to-merging of droplet impact on liquid film with different range of viscosities. The higher viscous liquid film tends to merge less due to the dissipation of the impact kinetic energy. Their experimental and mathematical expressions demonstrated the prediction for merging/bouncing for different liquids. Che and Matar [49] found different droplet hydrodynamics for impact on a liquid surface. Different parameters such as Weber number, Ohsenorge number, Viscosity ratio, and film thickness have been explored experimentally. Chen et al. [51] performed an experimental study

of impact onto a thin liquid film of miscible and immiscible liquids. They observed that the miscibility can affect the impact dynamics such as the crown formation and splashing, while the effect of film thickness is more complex. Impact on immiscible liquid film can provide information on the effect of the liquid film and its physics for impact on slippery lubricant impregnated surfaces.

1.3.3 Droplet impact on superhydrophobic surfaces

Superhydrophobic properties are associated with the Cassie-Baxter state of wetting [52]. The combination of surface roughness and low surface energy material (such as hydrophobic material) can minimize the adhesion of water on the surface. Superhydrophobic surfaces have been prepared with different approaches such as lithography, plasma treatment, etching, micro-machining, chemical vapor deposition, sol-gel processing, etc [53]. Droplet impact dynamics and its deformation on superhydrophobic surfaces are mostly governed by the droplet kinetic and surface energies. In an ideal well-structured superhydrophobic surface, droplet rebounds from the surface and the amount of time that droplet is in contact with the substrates is the contact time. In several applications, it has been attempted to reduce the contact time for instance in icing conditions. For $We \ll 1$, droplet behaves as a solid bulk impinging on a surface. For $We \geq 1$, it has been found that the contact time is independent of the impact velocity and is approximated by $\tau_o = \sqrt{\rho R_o^3/\sigma}$, where the droplet behaves as a spring-mass system. The contact time is also affected by the internal dissipation and surface-liquid adhesion which is the combination of two different contact time correlations of spreading and recoiling stage [54].

There have been several experimental, numerical, and theoretical analysis on droplet impact on superhydrophobic surfaces [55–62], where the effect of surface roughness and its topology, spreading of a droplet and its dynamics, the contact time of droplet especially in the freezing conditions, have been mostly evaluated. A review on history and recent advances in superhydrophobic can be found in [53]. For micro-scale droplets, the impact dynamics would be different compared to macro-scale droplets as the surface tension effect (capillary force) would be the dominant effect compared to inertial force in micro–droplets. Furthermore, the effect of micro–structured surface on the outcome of droplet dynamics become more noticeable for micro–droplets. Though many experimental and numerical studies have been presented for macro–scale droplet impact on SHSs, few experimental studies have been dedicated to the impact of micro–scale droplets on SHSs [63–65].

One of the most important issues in superhydrophobic surfaces is the Cassie-Wenzel transition that can

breakdown and hinders the bouncing feature in superhydrophobic surfaces [66, 67]. Several parameters can affect this transition such as evaporating the sessile droplet, increasing the volume of a droplet, and the topology of micro-structures (height, shape, or pitch of pillars). Additionally, superhydrophobic surfaces are only limited to repelling water droplets while they can be wet by low surface tension liquids such as oils. One of the parameters that affect this transition is the topology of micro-structures in SHS. Generally, once a droplet impacts a surface, the capillary pressure (P_C, due to the surface tension effect) and dynamic pressure (P_D, due to the inertia effect) play an important role in droplet dynamics. At high impact velocity such as in the pipe flow, the water hammer pressure (P_{WH}) is also generated [68] (due to the compression of the droplet by shock wave at larger impact velocity) at the contact area. The interplay between these pressure results in complete bouncing, partial bouncing, and complete wetting situations. Once the dynamics pressure exceeds the capillary pressure, the transition of a droplet to non-bouncing behavior is susceptible. Considering the water hammer pressure, the criteria for complete bouncing, partial-bouncing and non-bouncing are $P_C > P_{WH} > P_D$, $P_{WH} > P_C > P_D$ and $P_{WH} > P_D > P_C$, respectively [55]. There have been several studies on analyzing and improving the morphology of superhydrophobic surfaces [69, 70].

Despite various advantages of using superhydrophobic surfaces, they are mostly limited to repelling water and are likely wet by low surface tension liquids such as oils or other complex fluids low surface tension liquids. Additionally, their non-wetting features might collapse during the frost formation or exposing to high-pressure conditions [71–73]. Superomniphobic surfaces have been also introduced that can be applied to a broad range of liquids which has been first introduced by Tsujii et al. [74] which were defined as surfaces that have both superhydrophobicity and superoleophobicity features. Designing superomniphobic surfaces is based on the hierarchically structured surface or using the re-entrant surface texture (i.e., convex topography) in conjunction with surface chemistry. However, developing durable superomniphobic surfaces is challenging and needs further improvements [75, 76]. Developing mechanical durable re-entrant texture in superomniphobic surfaces has far been challenging. This is because their structures are comprised in nano-scale and very delicate to get damage. Additionally, the repellency of wide ranges of liquids on these surfaces has not been investigated thoroughly.

1.3.4 Droplet impact on slippery lubricant impregnated surfaces

Slippery lubricant impregnated surfaces (SLIPS/LIS) are another alternative for superomniphobic surfaces, where the micro/nano-textured or porous surfaces are filled with an immiscible liquid. Quere et al.

[77] was the first who introduced the idea of replacing the air plastron with a fluid. Based on this idea, immiscible liquids have been used in 2011 by Wong et al. [19] to lower the contact angle hysteresis which can be used for repelling a broad range of liquids. The inherent feature of these surfaces exhibits a low contact angle compared to SHSs, while the hysteresis angle is quite low. Wong et al. [19] introduced criteria that are needed to create SLIPS, 1. The lubricating liquid and working liquid must be immiscible. 2. The lubricating liquid must completely be absorbed by the surface and asperities 3. The working liquid must not preferentially wet the substrate over the lubricating liquid. These criteria result in a droplet with a contact angle hysteresis of 5° or lower.

The perfluorinated oils have been mostly used as they are capable of repelling different ranges of liquids. The lubricants are able to adhere completely within the micro/nano-structured surface due to capillarity. In this regard, silicone oils and Krytox oils have been used for infusing the structured surface. For instance, the Dupont Krytox oils are mostly thermally stable and nonflammable. It is nonvolatile and useful over a broad temperature range of $-75^\circ C$ to $350^\circ C$ or higher. Its high resistance to ionizing radiation makes it useful for the aerospace industry. However, depending on the applications, the toxicity of lubricant must be taken into consideration. One of the challenges in SLIPS is the depletion of the oil layer when the substrate is exhausted under conditions such as high temperature or abrasion which results in losing its repellency ability. Several solutions have been introduced to obtain a more stable substrate [19, 78, 79]. For instance, Shang et al. [80] have used a coating by mixing silicon oil-contained UV responsive micro-capsules. It has been observed that once the coating is exposed to UV/sunlight, the silicone oil can be released for the formation of a lubricant layer on the coating surface, which then results in a long-term self-repairing liquid-repellent coating.

Despite the vast research on the mobility of droplets, few studies are dedicated to the dynamics behavior of droplets [45, 81–83]. Kim and Rothstein [81] present the spreading and retraction dynamics of a droplet impacting a series of LIS surfaces. They investigated the effect of viscosity ratio on droplet dynamics when the droplet impacts LIS. They also compared their experimental results with their theoretical model that can predict the maximum diameter of the droplet. Unlike their expectation, they observed that for low We number, droplet spreading factor (the ratio of the maximum diameter of the droplet to its initial diameter) is greater for LIS for the low viscosity lubricant compared to air-infused SHS. They deduced that the receding contact angle is more susceptible to the oil viscosity than the advancing contact angle. Hao et al. [84] created a superhydrophobic-like bouncing regime on a thin immiscible liquid film with tunable thickness. This new

regime depends on the Weber number, film thickness, and viscosity. They found the critical We number for a droplet that exhibits bouncing behavior. Lee et al. [82] experimentally investigated the impact of millimeter-sized droplets on nanostructured surfaces infused with an oil layer (Krytox and other silicone oils). They evaluated how the physical properties of the oil and the impact velocity can lead to different impact behavior. They showed that oil viscosity has a limited influence on the maximal spreading radius, while the recoiling dynamics and also the stability of the oil layer were affected significantly by this parameter. Other research found that the maximum spreading radius was influenced by oil viscosity [81] which might be due to the different Weber numbers in the experiments. A variety of complex phenomena may occur during the droplet impact on oil-infused surfaces.

1.4 Droplet shedding dynamics

In addition to droplet impact, the mobility of droplets occurs frequently in nature and industrial applications. One of the driven forces for droplet mobility is the air shear flow, which is defined as droplet shedding. A droplet can be shed or moved on the surface once the adhesion force of the droplet overcomes the adhesion force. The incipient motion happens once the minimum air velocity leads to droplet movement. For instance, the movement of water droplets on airfoils is vital in order to prevent ice formation [42]. Several other applications involved air shear flow, such as for enhancing oil recovery where the oil droplet motion determines the oil recovery, for water managing in proton exchange membrane to remove excess water droplets inside a channel [85]. In biological applications where it is shown that how the viscous force can affect the cells spread and roll over the adhesion force [86].

As shown in Figure 1.8, at the incipient motion of droplet, the droplet deforms to a shape where the upstream and downstream contact angles called the $\theta_{\min}$ and $\theta_{\max}$, respectively. The adhesion force is the surface tension force of a droplet on a surface with a wetting length of L_w. Once the drag force which is the summation of both pressure integration component and shear stress component, overcomes the adhesion force, droplet shedding occurs. It should be noted that numerous parameters can affect droplet sheddings such as droplet size, droplet physical properties (surface tension, density, viscosity), surface topology, air speed, and boundary layer thickness. Surface wettability is a significant factor amongst all the parameters that affect droplet shedding. Surfaces with low adhesion properties have been used to enhance droplet repellency and mobility.

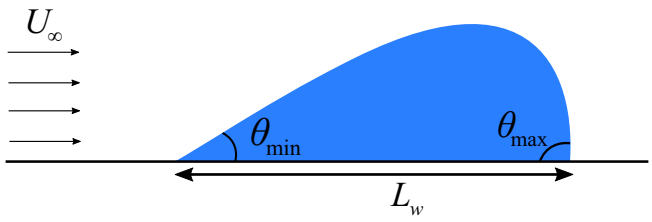

Figure 1.8: Schematic of droplet shedding under the effect of air shear flow

Several studies have been evaluated the performance of droplet shedding on superhydrophobic surfaces because of their surface morphology which results in high contact angle ($> 150^\circ$) and low contact angle hysteresis ($\sim< 10^\circ$) [87, 88]. Milne and Amirfazli [88] studied the performance of droplet shedding on different surface wettabilities. Their results showed that SHSs have the lowest critical air velocity. Some studies were analyzed how the onset of droplet shedding was affected by the presence of the vicinity droplets [89, 90]. They investigated the effect of arrangements of multiple sessile droplets by airflow. Four droplet arrangements including the triangle, square, reversed triangle, and diamond have been analyzed. It was found both the spacing between the droplet and their arrangements required different critical airflow for droplet shedding. In the case of having multiple sessile droplets, several studies studied the effect of droplet arrangements on their shedding [89, 90]. Different arrangements including the triangle, square, reversed triangle, and diamond have been analyzed. It was found both the spacing between the droplet and their arrangements required different critical airflow for droplet shedding. Moghtadernejad et al. [87] also investigated the physics of two droplets coalescence and shedding on superhydrophobic surfaces. Their results showed that droplet coalescence results in better droplet detachment from SHS, especially in low air speed of $5\,m/s$. Moghtadernejad et al. [91] conducted an experimental study of droplet shedding on superhydrophobic surfaces creating by a laser micro–machined approach. It was observed that droplet surface tension and viscosity can significantly affect the shedding behaviors. Their results exhibit droplet pinning within the asperities for ethylene glycol and propylene glycol whose surface tension and viscosity are low and high, respectively. Thus, High mobility features in superhydrophobic surfaces can be collapsed.

Besides the high slipperiness of SLIPS, it has been observed that the slippery surfaces have great potential for drag reduction [84, 92]. They have been considered as surfaces to enhance droplet mobility because of the low contact angle hysteresis feature that can be applied to a wide range of liquids. [93–96]. Stamatopoulos et al. [92] introduced a way to enable a complete transition of a Wenzel to a Cassie–Baxter state. They used the hemi-wicking of low surface tension (LST) liquid as an intervening layer. They identified

a critical tilted substrate and show a pseudo-Cassie–Baxter state. By increasing the tilting angle, a droplet detached from the intervening layer and exhibited a traditional Cassie–Baxter wetting state. This technique would enhance droplet mobility. Hao et al. [84] also used a thin liquid film to create a superhydrophobic-like bouncing effect, showing the advantage of slippery surfaces in fast droplet shedding. Solomon et al. [97] experimentally found that SLIPS can reduce the drag force in laminar flows, and they also presented a model to show this capability in SLIPS. They showed that LIS could reduce the drag force to 16% for a ratio of working fluid to lubricant viscosity of 260. Although superhydrophobic surfaces have better performance in droplet mobility in comparison to SLIPSs, the slippery surfaces have the additional benefit of increasing pressure stability, which is promising in microfluidics and turbulent flows.

1.5 Objectives

The goal of this thesis is to understand how the bio-inspired slippery lubricant impregnated surfaces perform compared to superhydrophobic surfaces for the impingement of droplet dynamics and shedding under the air shear flow conditions. Designing slippery lubricant impregnated surfaces is an essential key in order to obtain surfaces that perform as an omniphobic-like behavior. Thus, analyzing critical parameters including the effect of the immiscible liquid layer, impact velocity, and surface morphology is required. The objectives of this study are summarized as follows,

1. Evaluating the physics of the immiscible lubricant layer underlying the SLIPS for different liquid thicknesses and impact velocities (low Weber numbers) by implementing a three-phase flow model.

2. Analyzing the micro-pillars as the effect of surface morphology in SHS and SLIPS performance (such as pinning effect, droplet spreading, and recoiling) for a micro-droplet impact with different impact velocities using a three-phase flow model in conjunction with a dynamic contact angle method.

3. Investigating the shedding of a water droplet under the effect of air flow on SHS and SLIPS with different air speeds using both the experimental and numerical study to observe and compare physical behavior of droplet mobility.

1.6 Outline of thesis

This thesis is organized in a paper-based format which presents a fundamental study on the physics underlying the bio-inspired slippery lubricant impregnated surface compared to the superhydrophobic surface for droplet impingement and shedding conditions which can occur during the in-flight conditions.

Chapter 1 introduced fundamental parameters that can affect the surface wettability and its relevant parameters. An introduction to droplet impact (solid, liquid, superhydrophobic, and slippery lubricant impregnated surfaces) and shedding and possible attributed physical phenomena have been included in this chapter.

Chapter 2 presents a numerical study on the impact of a water droplet on an immiscible liquid film layer with different impact velocities (low Weber numbers) and different liquid film thicknesses (thin, thick, and pool liquid surface). A three-phase numerical model has been implemented which was validated with the theoretical model. The numerical simulation could capture the micro air layer beneath the droplet. Both the droplet and the immiscible lubricant layer deformation have been analyzed. The effect of liquid film on droplet impact that can induce spontaneous droplet bouncing has been investigated.

Chapter 3 presents more details on the effect of surface morphology on the performance of slippery lubricant impregnated surfaces compared to superhydrophobic surfaces for droplet impingement problems. The droplet is considered on micro-scale where the effect of surface morphology on droplet dynamics is more highlighted. Different Weber numbers have been studied to characterize the performance of SLIPS and SHS. The amount of droplet penetration within the micro-asperities has been evaluated which results in significantly less pinning effect in slippery surfaces.

In chapter 4, the mobility of a droplet under the effect of air flow with different air speeds has been studied experimentally. The performance of SHSs and SLIPSs has been evaluated in room temperature conditions. The behavior of droplet motion in SHS was completely different than SLIPS. Superhydrophobic surfaces resulted in a more spherical droplet shape and a higher drag force that led the droplet to detach from the surface. In SLIPS, the droplet exhibit combination of sliding and rolling behavior, in which the mobility of droplets depends on the viscosity of the coated lubricant on slippery surfaces. A numerical simulation in conjunction with the experimental work is also presented to enhance our observations in experimental results.

Finally, in chapter 5, a summary of our findings and further recommendations for future research are

provided. To better track the whole study, the thesis layout is given in a chart as follows.

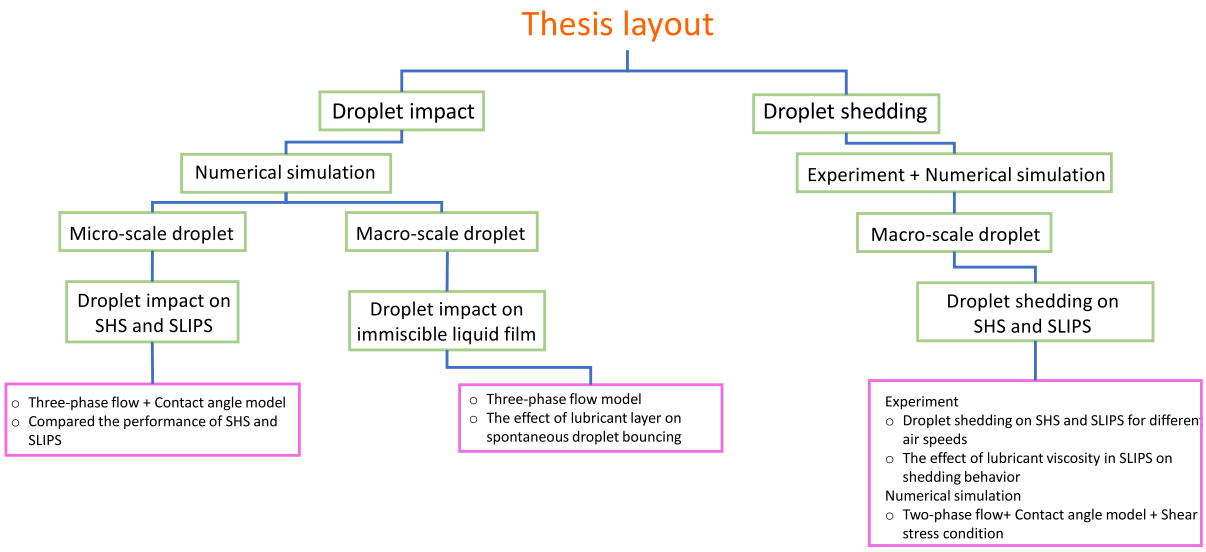

Figure 1.9: Schematics of thesis structure

Chapter 2

A Numerical Analysis of Air Entrapment During Droplet Impact on an Immiscible Liquid Film

[1]

2.1 Abstract

The air entrapment during droplet impingement is responsible for spontaneous droplet bouncing on an arbitrary solid surface at low Weber numbers. However, for the impact on liquid film surfaces, the outcome would significantly change, making it more favorable for the fabrication of non-wetting lubricant impregnated surfaces (LIS/SLIPS). In this paper, we describe a problem associated with the impact on a liquid surface using a three-phase flow model that captures the details of the gas layer thickness and dynamics of fluid motions. The numerical model was based on the finite volume solution coupled with the volume of fluid method to track the phases. The model was validated with the analytical solution. Consequently, the numerical tool was utilized to investigate the thickness of the entrapped air during the impact process while the behavior of droplet and the immiscible liquid film was quantitatively measured. The morphology of the interfacial gas layer was analyzed for key parameters including impact velocity and film thickness. It was observed that the presence of liquid film can reduce the probability of rupturing the

[1] "https://doi.org/10.1016/j.ijmultiphaseflow.2019.103175".

gas layer. The results for the profile of liquid film during droplet impact illustrated that the effect of film thickness can considerably influence the bouncing behavior.

Keywords: Droplet impact, Liquid film, LIS, Spontanous bouncing

2.2 Introduction

The phenomenon of droplets impacting surfaces has been studied due to various interesting physical phenomena and its importance in applications such as thermal spraying, coatings and inkjet printing [36, 98–100]. Depending on the application, the impact of droplet can be classified according to the impacting surface which may be a dry, thin liquid film or a deep liquid pool surface. In all cases, droplet impact consists of several discernible regimes including splashing, bouncing, and coalescing and understanding the physics behind the phenomena are of critical importance [101–103].

The outcome of droplet impact dynamics is mostly the inteplaying between surface tension, inertia and viscous force. Accordingly, these regimes have been characterized with the definition of dimensionless numbers, such as the Reynolds number (Re), the Weber number (We), and the Ohsenorge number (Oh). In the case of a wet surface, there are several key parameters such as liquid film thickness, liquid properties, and impact velocity that modulate the droplet dynamics behavior. The interacting dynamics of both liquids (droplet and liquid film) increases the complexity of the droplet impact process. Numerous experimental, theoretical, and numerical studies [104–106] have been conducted on droplet impacts on dry and wet surfaces (thin, thick and deep pool liquid film) to further define these different phenomena under various conditions..

An important associated phenomenon that can occur during the bouncing of a droplet from a solid surface is the formation of a thin gas layer underneath the center of the droplet upon the impact. This thin gas layer forms at low values of the Weber number and there have been few experimental observation using optical techniques [42, 43, 107]. De Ruiter et al. [107] reported that a droplet can bounce off a hydrophilic surface due to the creation of the thin air cushion, which they observed using reflection interference contrast microscopy (RICM). Some studies have illustrated that a high-pressure air pocket forms between the droplet and the substrate. This air pocket deforms the bottom surface of the droplet into a dimple-like shape and may endure throughout the impact until the droplet bounces. Further experimental studies also measured the thickness of the gas layer for a droplet impacting on a solid surface [41, 42, 107, 108]. Numerical simulation

have also confirmed the presence of the air layer and have provided further details on its dynamics [44, 83, 109].

Although most studies have been dedicated to analyzing the air cushion during the impact process on a solid surface, the mechanism for droplet impact on a liquid surface is still far from being fully understood.

Droplet impact on liquid surfaces is important in several industrial applications and recently in lubricant impregnated surfaces (LIS) due to their promising applications in omniphobic surfaces [19, 82, 110]. Complicated phenomena may occur during impact on a liquid surface such as crown formation and splashing that are influenced including different parameters of Weber and Reynolds numbers, dimensionless film thickness and viscosity ratios. Regarding the splashing phenomena, several studies introduced threshold splashing correlations for different conditions [111–113]. Chen et al. [51] performed experimental study of impact onto thin liquid film of miscible and immiscible liquids. They observed that the miscibility can affect the impact dynamics such as the crown formation and splashing, while the effect of film thickness is more complex. Amongst complicated phenomena during impact on liquid film, the air entrapment has been received less attention. For instance, characterizing the behavior of liquid film in LIS is vital for designing the slippery surface. The impact on finite liquid film thickness results in merging or bouncing, Tang et al. [114] demonstrated that for impact inertia less than the critical value, increasing the film thickness leads to a non-monotonic transition from merging to bouncing to merging and finally to bouncing again. This illustrated the role of the film thickness in the impact dynamics. Tran et al. [115] observed that for drops impacting a liquid bath of the same material, the liquid–air interface of the bath deforms. They deduced that the ruptures of the air film are related to the liquid viscosity and the impact velocity. Recently, few experimental studies have been performed to observe the interfacial gas layer during the impact of droplet on immiscible liquid film [49, 50, 115]. Tang et al. [50] illustrated the temporal dynamics of the gas layer for droplet bouncing on the liquid surface using high-speed imaging and color interferometry. They measured the thickness of the gas layer under several conditions and demonstrated the importance of the liquid film on droplet dynamics. Che and Matar [49] observed that at $We = 3.84$, the droplet impacting on a liquid surface bounces several times due to the gas layer separating the droplet and the immiscible liquid. Experimental studied demonstrated that due to the microscopic nature of the entrapped gas layer, characterizing the dynamics of air entrapment, measuring its thickness and interface morphology is quite challenging [49, 50]. Hence, additional comprehensive investigations are required.

For this process to be understood more fully, the goal of the present study is using numerical analysis

to investigate the profile of liquid film and droplet during impingement, measuring the air thickness and capturing the phenomena during the droplet impact dynamics. Although there are a significant number of studies in the literature on two-phase flows [61, 116–118], much less attention has been devoted to three-phase flows [119–121]. This is mostly due to the complexity of modeling these systems because of their phase interactions and the potential for triple-junctions to be present. To model the interaction between different phases in three-phase flow, Smith et al. [122] also proposed a method to decompose the surface tension coefficient. Another method is using the volume of fluid (VOF). In the current study, a volume of fluid (VOF)-based numerical tool for modeling the three-phase flow system was developed and validated using the analytical solution. Temporal characterization of the gas dynamics and fluid interface for different film thicknesses and impact velocities were investigated. Meanwhile, we characterized the role of the air layer on the behaviors of both the droplet and the liquid film using the two dimensionless parameters: normalized film thickness $h^* = \frac{h}{D_0}$, and Weber number $We = \frac{\rho_w U_w^2 D_0}{\sigma}$, where ρ_w, U_w, D_0, and σ are droplet density, impact velocity, droplet initial diameter, and surface tension, respectively, and h is the thickness of the liquid film.

2.3 Numerical methodology

Among different surface tracking methods that have been reported in the literature for computations of flows with moving interfaces [123–126], the volume of fluid (VOF) method has proven to capture interacial changes accurately due to its ability to conserve mass and handle sharp changes at the interface. In this work, the VOF method combined with the continuum surface force (CSF) model [127] was implemented in the open-source platform OpenFOAM [128]. Because of the symmetrical nature of this problem, a 2 dimensional axyisymmetric coordinate system (r, z) was used to model the flow dynamics, where r and z correspond to the radial and axial coordinates, respectively.

2.3.1 Governing equations

For an incompressible, newtonian, laminar flow, the equations governing the physics are given as follows,

$$\nabla \cdot \overrightarrow{U} = 0 \tag{2.1}$$

$$\frac{\partial \rho \overrightarrow{U}}{\partial t} + \nabla \cdot \left(\rho \overrightarrow{U} \overrightarrow{U} \right) = -\nabla P + \left[\nabla \cdot [\mu (\frac{\nabla \overrightarrow{U} + \nabla \overrightarrow{U}^T}{2}) \right] + \rho \cdot g + F_s \tag{2.2}$$

where ρ, μ, U and P are the density, dynamic viscosity, velocity field, and pressure of the flow, respectively. The surface tension force is denoted by F_s, which is computed at the interface region based on the continuum surface force (CSF) [127]. This force is computed as $F_s = \sigma \kappa \hat{n} \delta$, where σ is the surface tension coefficient and κ is the interface curvature defined as $-\nabla \cdot \hat{n}$, where $\hat{n}$ is a unit surface vector.

In order to capture the dynamics of each phase, the volume of fluid (VOF) method was used for tracking the interface, which is expressed by the volume fraction α_i, in which a value of i was assigned to each phase. The value of the volume fraction indicator α_i ranges between 0 and 1, where "$\alpha_i = 0$ " corresponds to cells filled with gas, "$\alpha_i = 1$ " corresponds to cells filled with liquid, and "$0 < \alpha_i < 1$" represents the liquid/gas interface. A schematic of the volume fraction distribution for a two-phase flow is shown in Figure 2.1a. The evolution of the interface was computed using the following transport equation,

$$\frac{\partial \rho \alpha_i}{\partial t} + \nabla \cdot \left(\overrightarrow{U} \alpha_i \right) + \nabla \cdot \left(\overrightarrow{U}_r \alpha_i \left(1 - \alpha_i \right) \right) = 0 \tag{2.3}$$

where U_r is an artificial compression relative velocity at the free surface that is applied normally into the interface to counteract the numerical diffusion and maintain a sharp interface defined as,

$$\overrightarrow{U}_r = \left(\min \left(C_{\alpha_i} \left| U \right|, \max \left(\left| U \right| \right) \right) \right) \frac{\nabla \alpha_i}{\left| \nabla \alpha_i \right|} \tag{2.4}$$

where C_{α_i} is the compression coefficient, which determines the degree of compression.

2.3.2 Numerical method in three-phase flows

Since a three-phase flow system of a water droplet, an immiscible liquid film, and the surrounding air was the focus of the current work, a multiphase flow solver was required for producing a numerical solution.

For a three-phase immiscible flow system (water–oil–air), the volume fraction distribution is shown in Figure 2.1b. The volume fraction of each phase is distributed according to the transport equation, provided that $\sum_{i=1}^{n} \alpha_i = 1$, where n is the the number of phases. In this study, $n = 3$ as we have three different immiscible flows. In regions where all three phases exist, the volume fraction is distributed as shown in Figure 2.1b. In the case of three-phase flows, all variables of fluid properties such as density and viscosity

are defined by their phase fraction and their values of ρ_i and μ_i, which define the density and viscosity of each phase, respectively. Accordingly, the physical properties of fluids are calculated according to the average weight of the volume fraction of each fluid. The physical properties of fluids are obtained as a volumetric mixture value, $\rho = \sum_{i=1}^{N=3} \alpha_i \rho_i$ and $\mu = \sum_{i=1}^{N=3} \alpha_i \mu_i$ where N is the number of phases.

In regions where all three phases exist (triple points), the complexity of three-phase modeling is much higher than for two-phase modeling. Simultaneous modeling of three-phase interaction is challenging and there are few studies carried out to model the interactions [121, 122]. For instance, Smith et al. [122] proposed a method to decompose the surface tension coefficient based on the binary surface tension between phases.

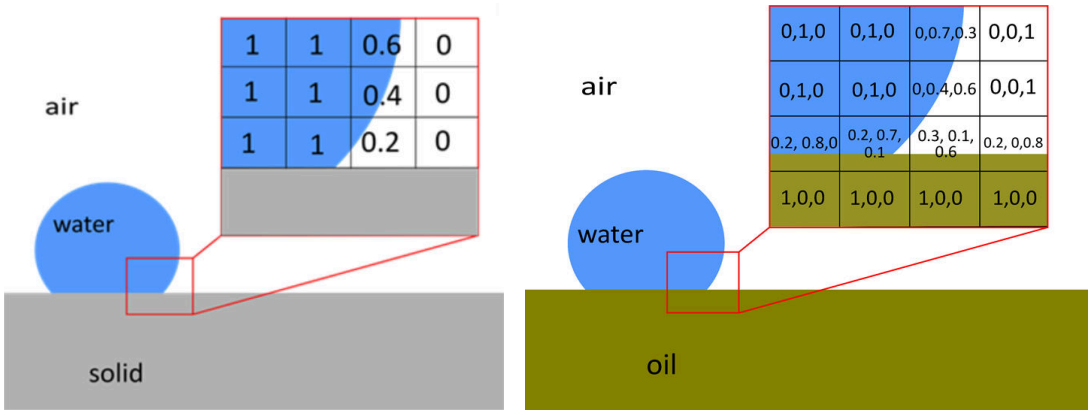

(a) (b)

Figure 2.1: Schematic of volume fraction distribution in VOF method for (a) two-phase: air α_a)/water (α_w) (b) three immiscible phase: air (α_a)/water (α_w)/oil (α_o). Values in each cell corresponds to the volume fraction contained in the cell

In the current work, the surface normal and surface curvature are determined using the Dirac delta function [120]. In the case of three-phase flows, this method calculated the surface tension force with $F_s = \sum_{i=1}^{3} \sum_{j\neq 1}^{3} \sigma_{ij} \kappa_{ij} \delta_{ij}$ where σ_{ij} and κ_{ij} are the physical interfacial tension and the curvature between the two phases of i and j, respectively. In fact, all the domain follows the two-phase flow algorithm except the surface tension at the triple region (where all three phases meet) which is the summation of all binary interfacial tension force. The Dirac delta function as implemented was,

$$F_s = -\sum_{i=1}^{3} \sum_{j\neq 1}^{3} \sigma_{ij} (\nabla \cdot (\frac{\alpha_j \nabla \alpha_i - \alpha_i \nabla \alpha_j}{|\alpha_j \nabla \alpha_i - \alpha_i \nabla \alpha_j|})) (\alpha_j \nabla \alpha_i - \alpha_i \nabla \alpha_j) \tag{2.5}$$

The governing equations were then discretized by using the finite volume method and following the

schemes detailed in Table 2.1. Finally, the simulation of the 2D axisymmetric geometry was performed in parallel using the PIMPLE algorithm, which is a combination of the PISO (Pressure Implicit with Splitting of Operator) and SIMPLE (Semi-Implicit Method for Pressure-Linked Equations) algorithms.

Table 2.1: Discretization schemes

Term	Discretization scheme
$\frac{\partial}{\partial t}(\rho U)$	Euler
$\nabla \cdot (\rho U U)$	Gauss Limited Linear V1 (TVD)
$\nabla \cdot (\alpha U)$	Gauss VanLeer
$\nabla \cdot (U_r \alpha (1-\alpha))$	Gauss interfaceCompression

2.3.3 Adaptive time step

To optimize the computational time, an adaptive time-step control feature was applied. The time-step control feature also ensured the stability of the solution procedure as it was adjusted based on the Courant Friedrichs Lewy number ($Co = \frac{u_i \Delta t}{\Delta x}$) at the beginning of the time iteration loop. Using the values of the velocity of the phase fractions and Δt from previous time step, the maximum local Courant number (Co_0) was calculated and a new time-step was iteratively initiated.

$$\Delta t = min \left\{ \frac{Co_{max}}{Co_0} \Delta t_0; \left(1 + \lambda_1 \frac{Co_{max}}{Co_0}\right) \Delta t_0; \lambda_2 \Delta t_0; \Delta t_{max} \right\} \tag{2.6}$$

where Co_{max} and Δt_{max} were prescribed values for the Courant number and time step, respectively. Moreover, in the beginning of the simulation at a very small initial time-step (Δt_{ini}), an intermediate time-step value was calculated by using the formula

$$\Delta t^*_{ini} = min \left\{ \frac{Co_{max}}{Co_0} \Delta t_{ini}; \Delta t_{max} \right\} \tag{2.7}$$

Then, this intermediate value (Δt^*_{ini}) was used as Δt_0 in the new time-step calculation, providing a Co_0 as close to the maximum Courant number. The size of time steps varied during the calculations because of this Courant value maximization, which allowed the time step to be smoothly adjusted.

2.3.4 Validation of the three-phase model

In this section, following the method of Boyer et al. [121], the model was validated for an equilibrium droplet lens problem, which is a well-suited case for a three-phase flow model verification. The droplet lens problem is the situation of a spherical water droplet spreading at the middle of a straight surface between two immiscible fluids (oil and air). A schematic of the initial conditions are shown in Figure 2.2a. The balance of interfacial forces leads the droplet to reach a final equilibrium condition (Figure 2.2b).

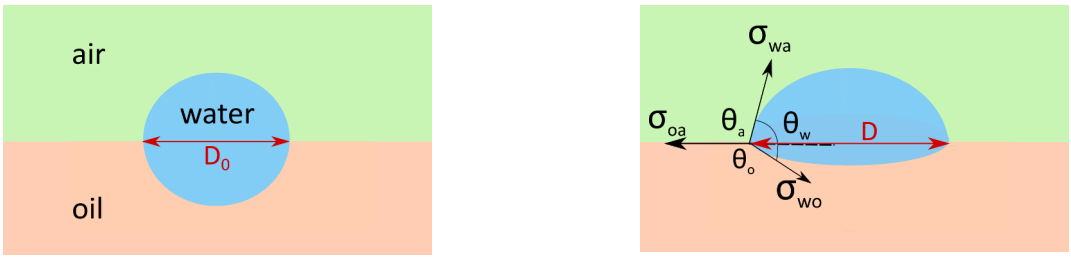

(a) (b)

Figure 2.2: Schematic of droplet spreading between two immiscible phases (a) Initial condition (b) Equilibrium condition

In this model, we used a 1 mm droplet in the initial spherical position, and neglected the effects of gravity. Therefore, the interfacial surface tension force between phases was entirely responsible for the final configuration of the droplet. At the equilibrium state, the final diameter of the droplet D (shown in Figure 2.2b) and the contact angle of each fluid were obtained according to the geometry and mathematical balancing of the interfacial tensions. The details of calculating equilibrium diameter and contact angle are presented in Appendix A.

To assess the accuracy of this model compared to the analytical solution, two cases for different interfacial surface tension were simulated [33]. All details of quantitative and qualitative comparison of validation results are illustrated in Appendix A. The results of the final droplet diameter and contact angles of phases were compared to that obtained in the analytical model and it was observed that they were in good agreements.

2.3.5 Computational set-up

A 2D axisymmetric geometry was performed for all cases. The droplet was located in the center of the computational domain, which was sized about $5D_0 \times 10D_0$ to make sure that the hydrodynamics of the

droplet were not affected by the domain boundaries (Figure 2.3). For high liquid film thickness ($h^* > 1$), since the liquid film deformation is more significant, the computational domain is expanded to $10D_0 \times 10D_0$. As the thickness of the air layer is on the order of a few micrometers, the size of the cells in the computational domain is around 1 micrometer.

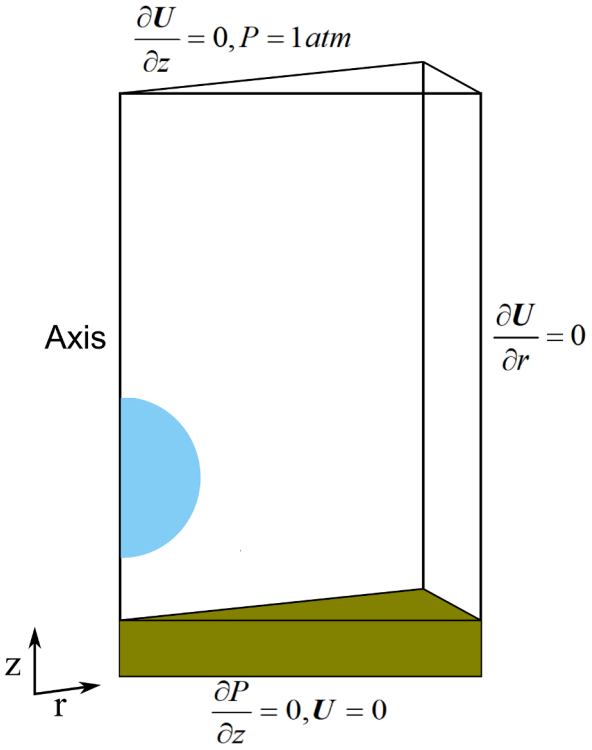

Figure 2.3: Schematic of computational domain of the numerical model

A no-slip boundary condition applied to the bottom surface of the geometry with the gradient effect of the pressure is considered to be zero. Since the top surface is subjected to the atmosphere, the boundary conditions of atmospheric pressure with no gradient effect of velocity has been considered.

Regarding the fluids properties, a water droplet with a diameter of $D_0 = 2mm$ and a perfluorinated liquid (Dupont Krytox 103) were used as the droplet and liquid film materials for this study, since this system is used in various applications. The reason behind using this liquid film is due to its wide range applications specially in the lubricant impregnated surfaces (LIS). This system also has the simplifying advantage of low adhesion of the water droplet to the surface. The physical properties of the droplet and the lubricant are presented in Table 2.2.

For droplet impact on liquid surface, according to what have been observed in experimental study, the

Table 2.2: Physical properties of fluids

Fluids	**Density**($^{kg}/_{m^3}$)	**Viscosity**($Pa.\ s$)	**Surface tension**($^{N}/_{m}$)
Dupont Krytox103	1900	0.15	0.017
Water	1000	0.001	0.07

presence of the liquid film influences the behavior of the droplet dynamics and air layer since the liquid film is able to deform during the impact process [49, 50]. In this study, we carried out a numerical study of water droplet impact on a liquid film for film different thicknesses and impact velocities, to identify this air layer thickness (δ) quantitatively. Additionally, to better understand how the droplet and liquid film behave during the impingement, we used two green and red points on the droplets and liquid film, as shown in Figure 2.4, that better represent the similarities and differences for a visual comparison.

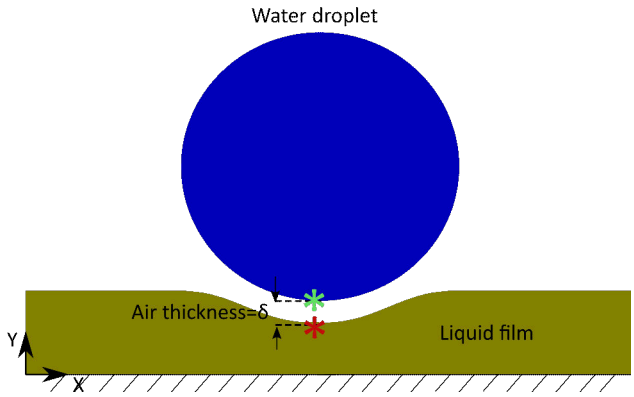

Figure 2.4: Schematic of droplet impact on a liquid film of lubricant

In the next sections, we discuss comprehensively the effects that impact velocity and film thickness had on the mechanism of the impact events.

2.4 Results and discussions

2.4.1 I. Role of the droplet impact velocity on the air layer

To identify the behavior of the droplet and the liquid film, the impact of a water droplet on a liquid film with a thickness of $h^* = 0.025$ was studied at three different Weber numbers ($We = 1.5$, 5, and 10). The liquid film can be treated as the thin film surface ($h^* < 1$) [48, 50] which can be suitable candidate for LIS applications [30, 84]. For a droplet at $We = 1.5$, numerical and experimental studies have shown the presence of an air layer between the droplet and a solid surface [44, 107]. Analogously, we found that an air

layers was entrapped during the impact of a droplet on a liquid surface, which results in the droplet bouncing without touching the liquid film. At low Weber number, the base surface (liquid film) was slightly affected by the droplet inertia, however the droplet follows the same hydrodynamics as was observed on solid surface (i.e. spreading, rebounding, bouncing). Figure 2.5 illustrates this situation and compares the results from the numerical modelling (droplet impact on thin liquid film) performed in this study to experimental results (droplet impact on solid surface) conducted by De ruiter [107].

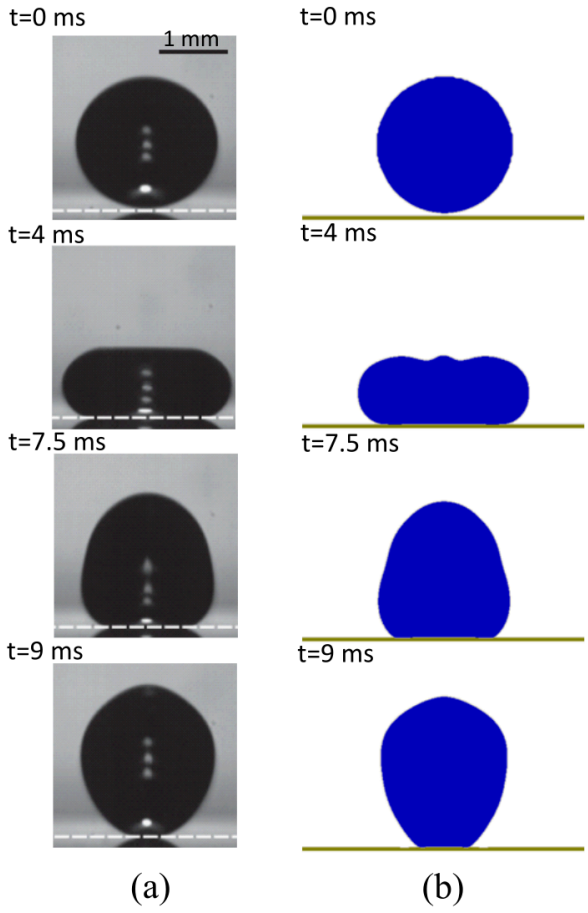

Figure 2.5: Comparison of droplet impact at $We = 1.5$ (a) On a solid surface, experimental results [107] and (b) On a thin liquid film surface ($h^* = 0.025$), numerical results

It can be seen that although both the droplet and liquid film interface was affected, droplet hydrodynamics was similar to the case of droplet impact at low Weber number on a solid surface in the experimental study.

As discussed, the liquid film was deformed during the impingement process. To investigate the deformation in the liquid film and the droplet, the profile of the central points of both the water droplet and the

liquid film were labelled to clearly identify their behavior during the impingement. Figure 2.6 illustrated that the liquid film (lubricant) was deformed as the droplet started moving downward, and the air cushion was generated beneath the droplet. The velocity vector field in fluids at few millisecond of impingement demonstrated that how the thin liquid film would react to droplet impact and the squeezed air can deform the liquid film. It can be seen that the central point of liquid film profile at low Weber number of 1.5 was almost constant after the first deformation of the liquid film occurred.

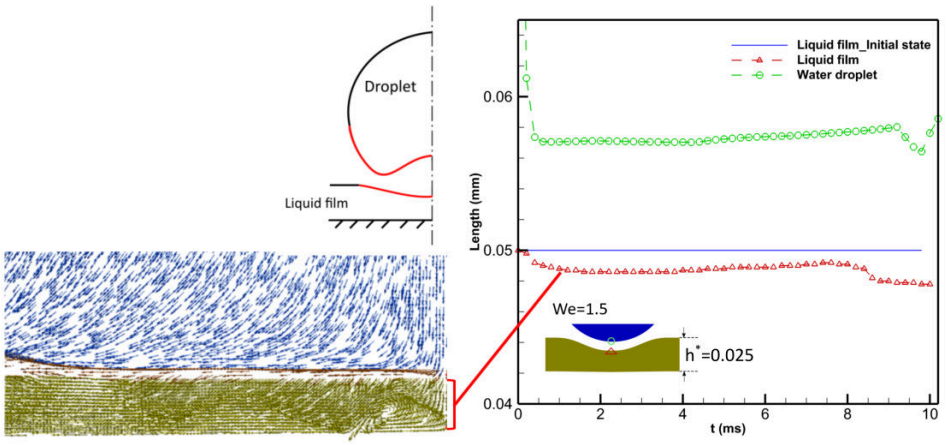

Figure 2.6: Profile of water droplet and liquid film interface at the center of impact over time ($We = 1.5$ and $h^* = 0.025$)

To investigate the effect of Weber number on droplet and the liquid film hydrodynamics, impacts at two Weber numbers of $We = 5$ and 10 were also modeled. Since the droplet detached from the solid surface by $We \simeq 7$ [107], it was expected that the droplet would display spontaneous rebounding from the liquid surface below that threshold. However, the presence of a liquid film affected the impingement hydrodynamics even at a very small liquid film thickness. By increasing the Weber number to $We = 5$, droplet spread over a layer of entrapped air beneath the droplet, as shown in Figure 2.7. The droplet reached its maximum diameter ($t \simeq 3\ ms$) and retracted due to the surface tension until it bounced from the liquid surface ($t \simeq 10\ ms$).

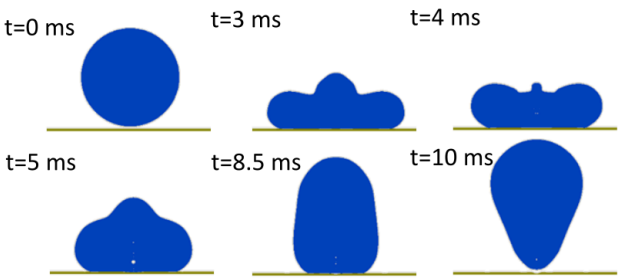

Figure 2.7: Evolution of water droplet impact on a thin liquid film ($We = 5$ and $h^* = 0.025$)

The air cushion can produce a dimple-like shape in the water droplet as reported for the impact of a droplet on a solid surface [42, 115]. The interface profile of both the droplet and liquid film changed significantly during the few milliseconds of droplet impact, as shown in Figure 2.8. In fact, during the spreading stage, the pressure build-up would change both the interface profile of water droplet and liquid film, even for a thin liquid film. This would indicate that the deformation occur in both water droplet and liquid film, especially during the few milliseconds of impingement until it spread to maximum diameter. After that, during the rebounding stage, more phenomena happen which would be illustrated in quantitative details.

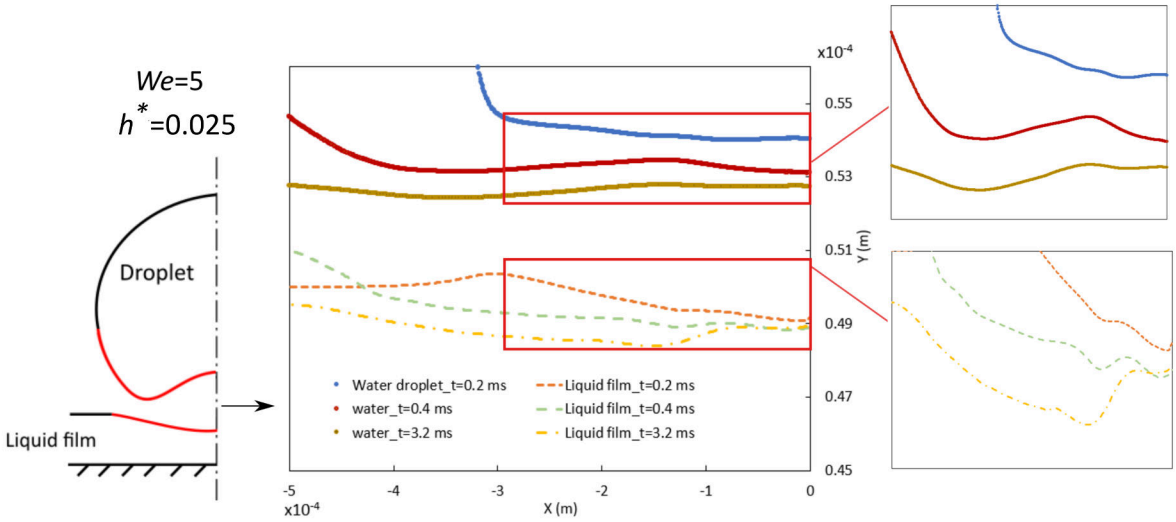

Figure 2.8: Profile of the water droplet and liquid film interface ($We = 5$ and $h^* = 0.025$)

The profile of central points of the droplet and the liquid film was measured over time for the impact at $We = 5$ (Figure 2.9). A significant deformation in the profile of both the droplet and the liquid film was

observed. The deformation during the spreading stage until $t \simeq 4\ ms$ remained constant.

It is found that an air bubble is formed within the droplet (Figure 2.7) during the retraction process ($t \simeq 4\ ms$ to $t \simeq 5\ ms$). Due to the kinetic energy of droplet, droplet deformed into the pyramid shape during the spreading stage due to the capillary waves. Accordingly, the air cavity was formed at the center of the droplet which results in air bubble entrapment within the droplet that has been also observed in experimental studies, such as impact on a superhydrophobic surface, soft and viscoelastic surfaces [129–131]. This air bubble was not formed at $We = 1.5$, since the droplet deformation was not large enough to generate the bubble. Then, the bubble was ejected from the droplet ($t \simeq 7.5\ ms$), and, consequently, the height of droplet profile increased slightly (at $t \simeq 8\ ms$) as the liquid film height decreased. Finally, droplet bounced completely at $t \simeq 10\ ms$.

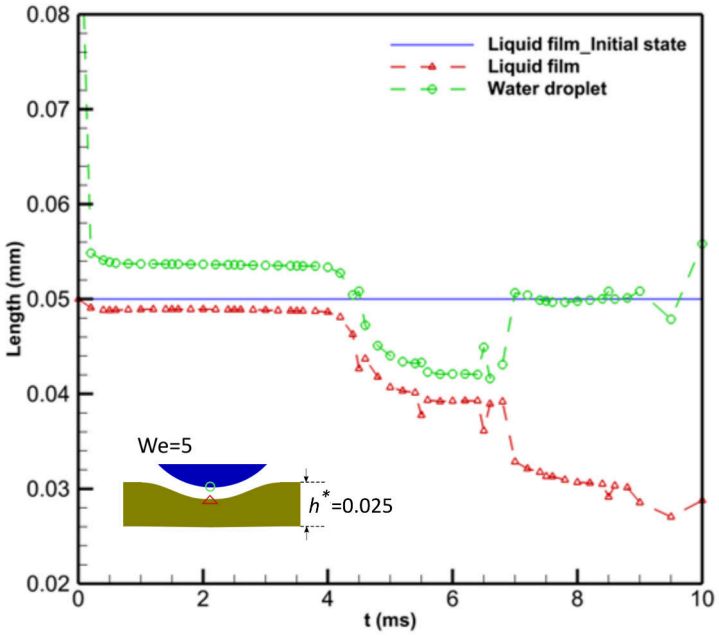

Figure 2.9: Profile of the water droplet and the liquid film interface at the center of impact over time ($We = 5$ and $h^* = 0.025$)

Further increase of the Weber number to $We = 10$ was also investigated. The temporal evolution of the shape of the water droplet and thin liquid film is shown in Figure 2.10. Despite the failure of the droplet to bounce from a solid surface at Weber numbers greater than around 7, we found that the bouncing behavior of a water droplet from a liquid surface to be different. Figure 2.10 illustrates the qualitative comparison of the numerically calculated results of droplet impact on a thin liquid film with the time lapse images from the experimental droplet impacts performed by Hao et al. [84]. There was good agreement in the

hydrodynamics of the droplet between the numerical model and the experimental results.

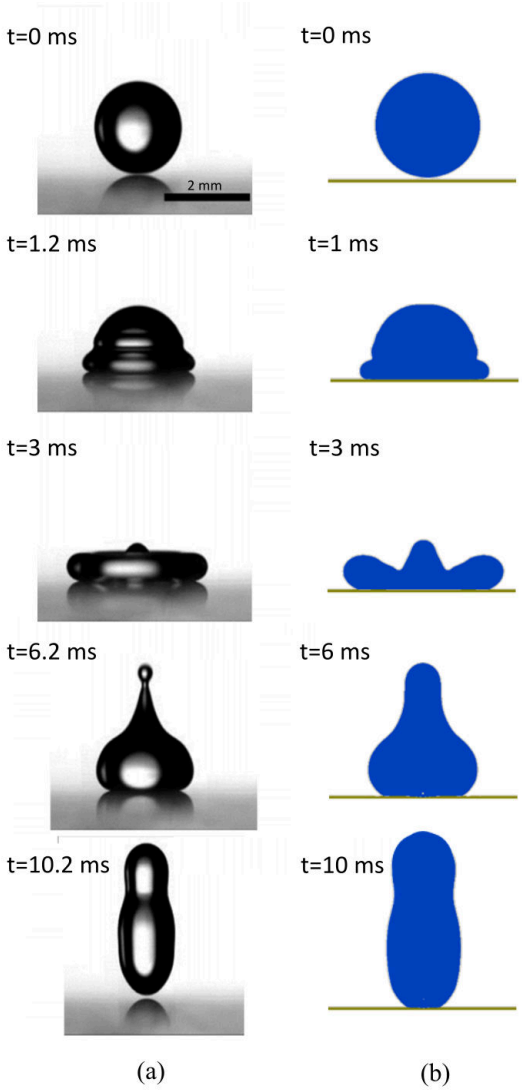

Figure 2.10: Comparison of water droplet impact on a thin liquid film (a) Experimental results [84] and (b) Side-view of numerical results ($We = 10$ and $h^* = 0.025$)

The spreading factor, defined as the ratio of maximum droplet contact length ($D_{\max}$) to the initial droplet diameter (D_0), was quantified and validated against experimental results [84]. Figure 2.11 illustrates the result that the normalized droplet spreading length in the numerical model agreed well with the experimental results.

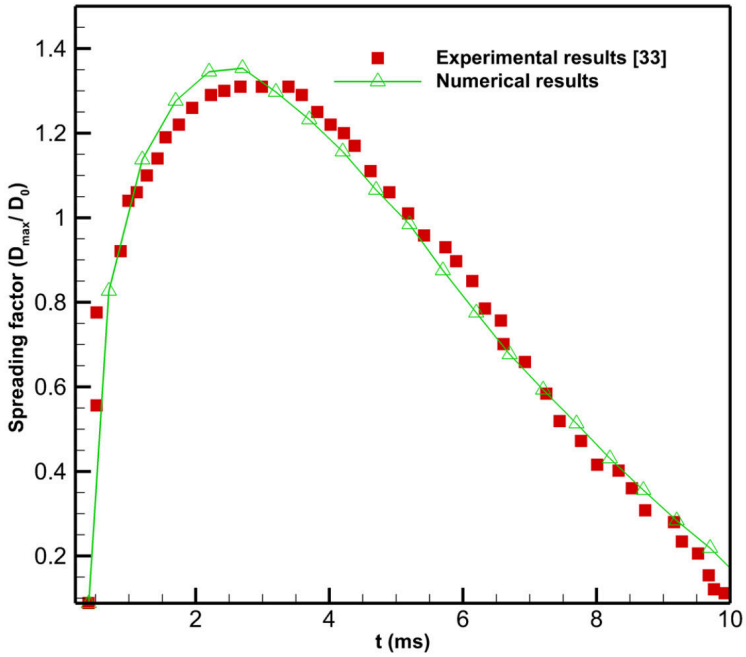

Figure 2.11: Comparison of numerical study of spreading factor ($D_{\max}/D_0$) of droplet impact at $We = 10$ on a thin liquid film of $h^* = 0.025$ with experimental results [84]

The spreading factor alone cannot describe all of the details behind the droplet impact behavior. For this reason, we characterized the deformation of the central point of the droplet and the liquid film over time. For $We = 10$ we could subdivide the droplet bouncing mechanism into four distinct sections to better clarify the process, as displayed in Figure 2.12. In section I, there was a slight increase in the droplet height and a decrease in the liquid film height due to the dimple formation, which was also seen in the lower Weber numbers ($We = 1.5$ and 5). After this region, the droplet started spreading until $t \simeq 4\,ms$ and no significant deformation in the liquids interface was seen during the spreading process. Once the water droplet began to rebound, the liquid film moved downwards (section II). In section III, the droplet height increased during the rebounding process. In fact, at the start of the droplet rebounding, a small bubble was entrapped within the water droplet. It was then ejected from the water droplet, which led to an increment in droplet height and a decrease in the liquid film height. Finally, the effect of the bubble on the fluid height dissipated and the droplet bounced from the liquid surface in section IV.

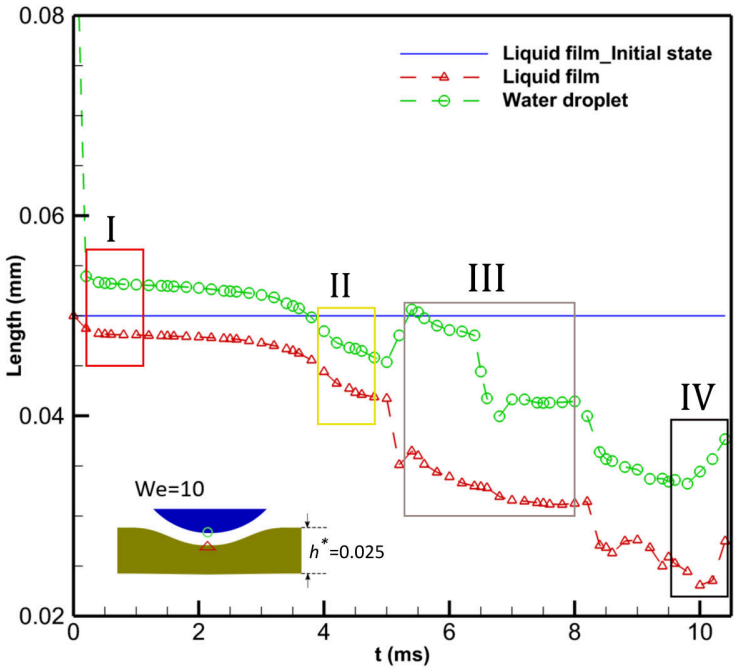

Figure 2.12: Profile of the water droplet and liquid film interface at the center of impact over time ($We = 10$ and $h^* = 0.025$)

The interface profile of droplet and liquid film is plotted for $We = 10$ and $h^* = 0.025$ in Figure 2.13. Similarly, both of the droplet and liquid film interface were changing upon the impact.

We also calculated the thickness of the entrapped air layer (δ as shown in Figure 2.3) between the droplet and the liquid film for models run at different Weber numbers, and plotted them in Figure 2.14a. The air layer was maintained during almost all of the impingement process at the lowest Weber number tested, $We = 1.5$, while considerable deformation of this layer was observed at the higher Weber numbers. Additionally, the effect of the inertia force in the $We = 5$ and $We = 10$ case resulted in a squeezed air layer, especially during the rebounding stage, except the rise in some cases because of the ejecting bubble inside the droplet.

A scaling law for the dimensionless height of dimple formation for impact on a solid surface has been suggested by Bouwhuis et al. [132], $H_d/R \sim \mathrm{St}^{-2/3}$, where St is the Stokes number which is defined by $St = \rho_l RU/\mu_g$. For We= 5 and 10, it is observed that the dimple height on thin liquid film is slightly lower ($\sim 3-5\%$) due to the damping caused by the thin liquid film comparing to the predicted height for impact on a solid surface [132].

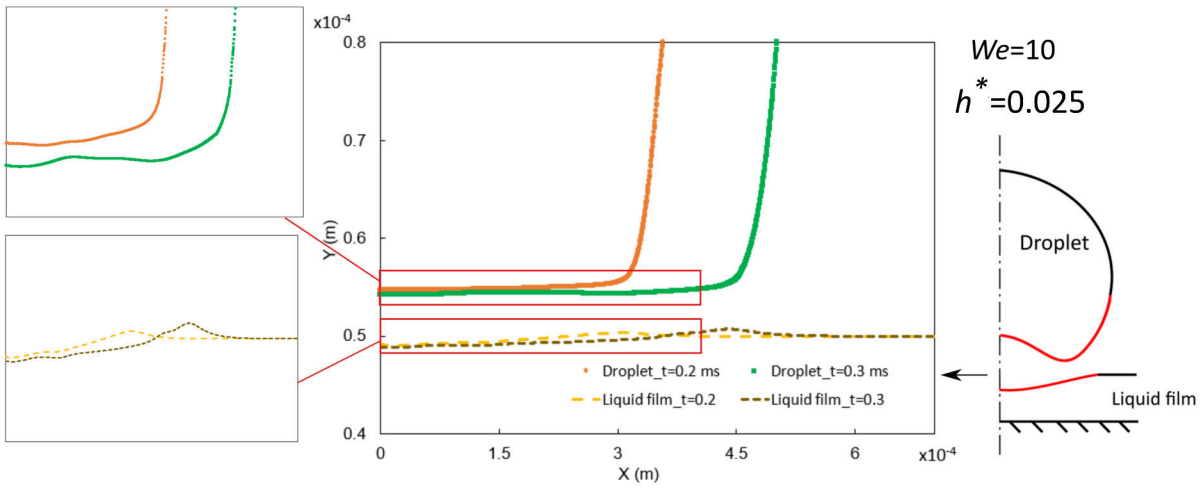

Figure 2.13: Profile of the water droplet and the liquid film interface ($We = 10$ and $h^* = 0.025$)

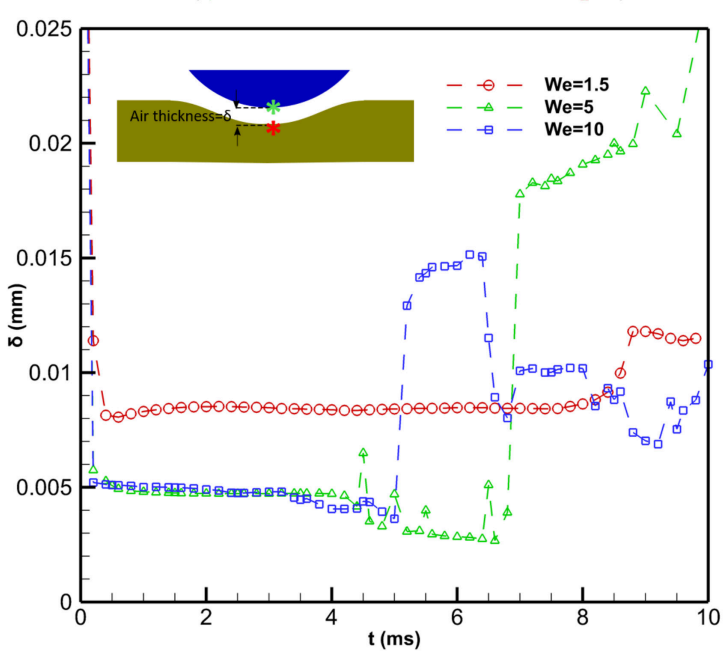

Figure 2.14: Evolution of air layer thickness for different Weber numbers

It can be observed in all cases that although the deformation of the very thin liquid film was largely restricted by the solid surface, the presence of the liquid film and its movement during impingement substantially changed the conventional mechanism of impact on a solid surface and increased the probability of the droplet bouncing.

2.4.2 II. Role of the liquid film thickness on the air layer

In this part, we looked at the effect of the liquid film thickness at the same Weber number ($We = 5$) for a range of three film thicknesses. It should be noted that different classifications of the liquid surface have been used for different thicknesses, as they behave differently [104]. For instance, $h^* < 0.1$ [47] is recommended as a thin liquid film, while several investigations suggest that thin films are associated with $h^* < 1$. In this study, $h^* = 1$ was used as the threshold to distinguish the liquid thin film regime from the liquid pool regime. The results for liquid thin film of $(h^* = 0.025)$ for $We = 5$ were demonstrated in previous section. The effect of the liquid film thickness on a thin film $(h^* = 0.1)$ and liquid pool film $(h^* = 2.5)$ was also studied. Although the case of $h^* = 0.1$ belongs to the group of liquid thin film ($h^* < 1$), this treatment could have a significant impact on the hydrodynamic changes of the liquid and the gas. For the case of $h^* = 0.1$, the time lapses of the impact process are displayed in Figure 2.15. The process of the droplet rebounding from the liquid surface occurred due to the entrapped air beneath the droplet, which was a similar mechanism to what has been explained in the previous section.

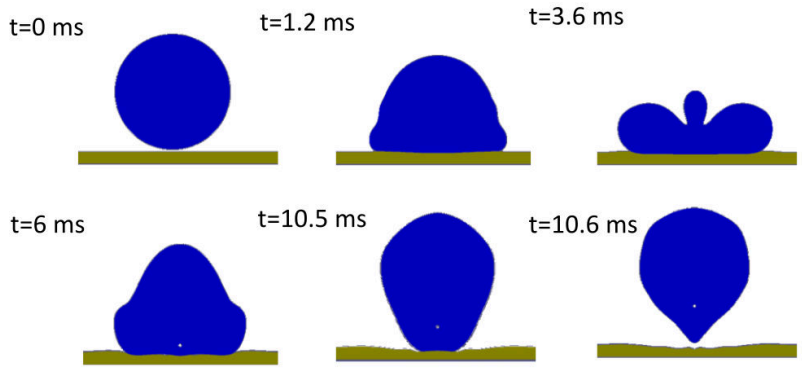

Figure 2.15: Evolution of water droplet impact on a thin liquid film surface ($We = 5$ and $h^* = 0.1$)

The spreading factor (D_{max}/D_0) of the $h^* = 0.1$ case was similar to the case of a thin liquid film of $h^* = 0.025$ (as shown in Figure 2.20). The profile of the droplet and the liquid film at the center point of fluids were calculated and are shown in Figure 2.16. Both the droplet and the liquid film experienced deformation through the impingement process. The plot of interface profile in Figure 2.17 is also provided for the $We = 5$ and $h^* = 0.1$. It was observed that although the thickness of liquid film is in the thin film regime, the profile of the liquid film interface was tending to deform more significantly during the initial impingement process comparing to the $h^* = 0.025$.

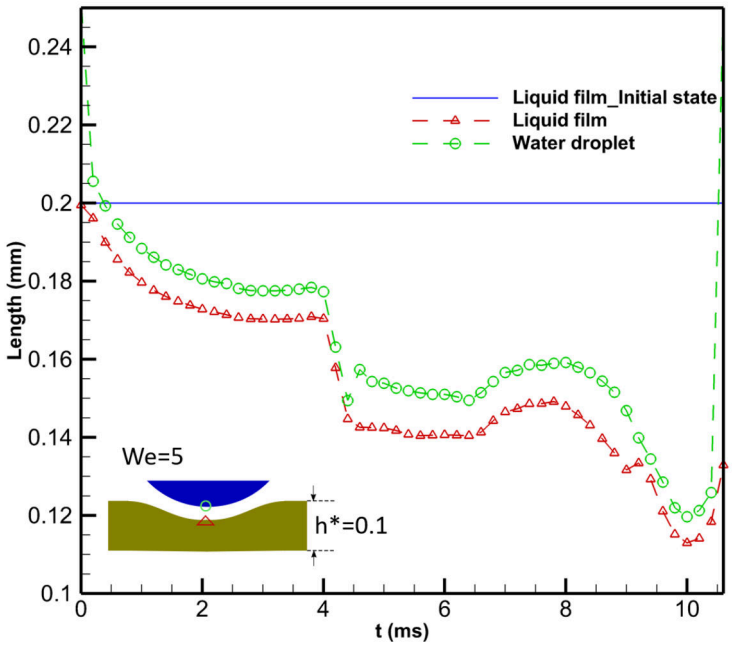

Figure 2.16: Profile of water droplet and liquid film interface at the center of impact over time ($We = 5$ and $h^* = 0.1$)

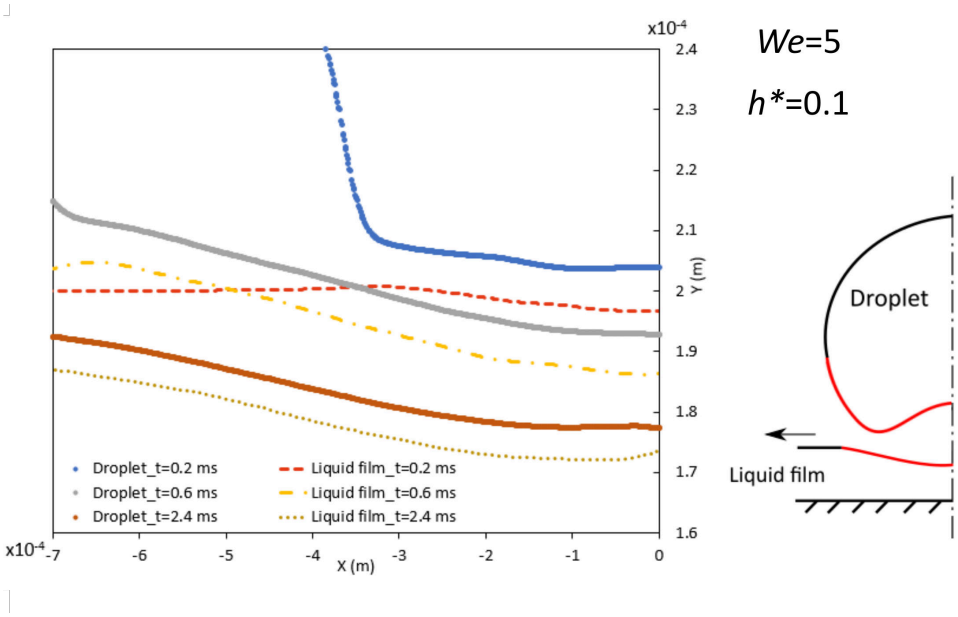

Figure 2.17: Profile of the water droplet and the liquid film interface ($We = 5$ and $h^* = 0.1$)

For the case of a deep liquid pool of liquid film where h^* = 2.5 at $We = 5$, the evolution of the droplet impact is shown in Figure 2.18. A more significant deformation in the deep liquid pool during the impact process has been observed. The air layer was significantly squeezed during the impingement while the large

deformation in the liquid film occurred. In fact, at this Weber number, the large pool thickness was less constrained by the solid surface than was the thin film, and, consequently, the liquid surface adapted in shape to the droplet impact.

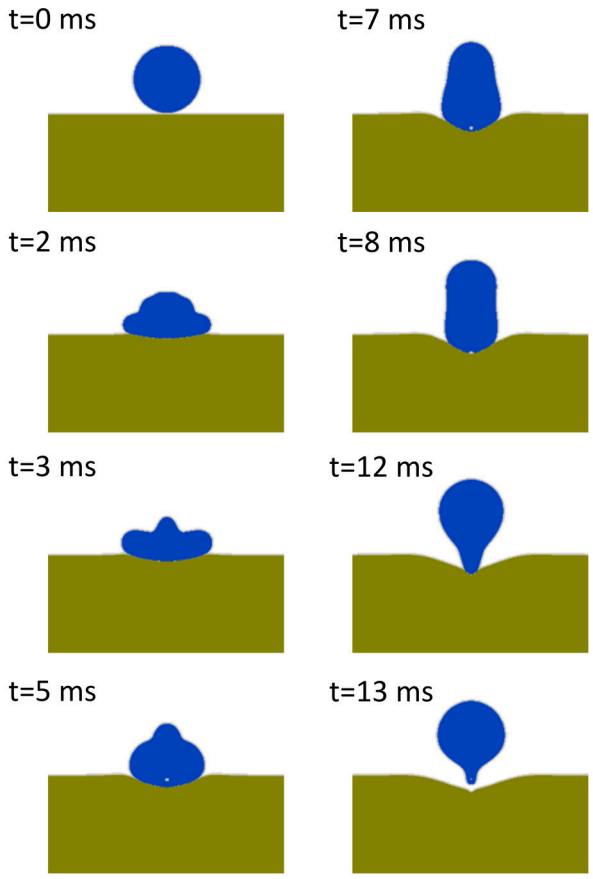

Figure 2.18: Evolution of water droplet impact on a deep liquid film surface ($We = 5$ and $h^* = 2.5$)

In Figure 2.20, the spreading factor of the droplet indicated that the droplet experienced less spreading in the case of the liquid pool compared to impingement at lower values of h^*. This is because the liquid film was less restricted by the solid surface, and, consequently, a large deformation of the liquid resisted the droplet spreading outwards compared to the case of the thin liquid film. The delay in the rebounding of the droplet from a deep liquid surface was also attributed to a higher penetration of both the droplet and the liquid film, which had been also observed experimentally by Tang et al. [50].

In the case of deep pool of liquid film, the profile of fluids interface are presented in Figure 2.19. Since the inertia force is not high and the liquid film is not constraint by the solid surface, it can be seen that the

motion of liquid film is alongside the water droplet while the air film is captivated within the droplet and liquid film. Thus, the dimple-shape is less significant in this case.

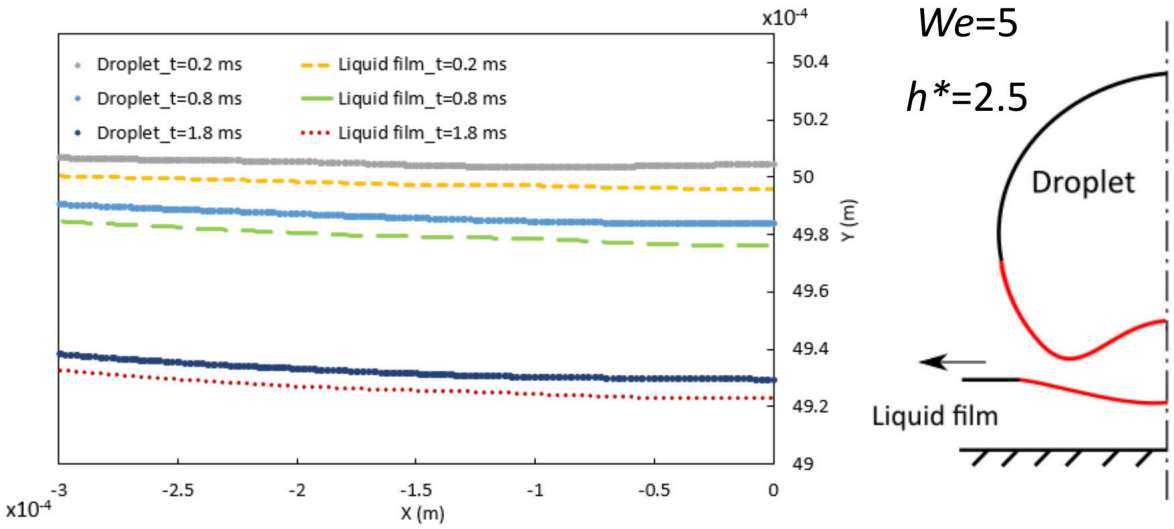

Figure 2.19: Profile of the water droplet and the liquid film interface ($We = 5$ and $h^* = 2.5$)

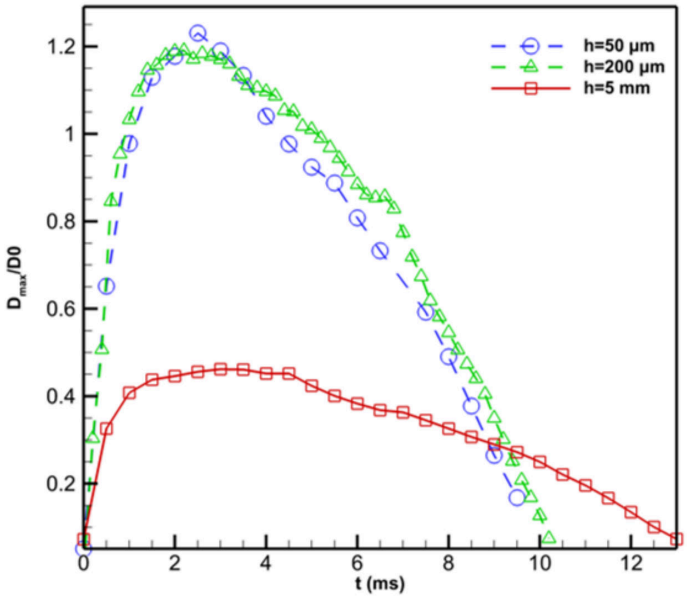

Figure 2.20: Spreading factor over time at $We = 5$ and for different liquid film thicknesses ($h^* = 0.025$, $h^* = 0.1$ and $h^* = 2.5$)

In order to quantify and analyze the dynamics of the deep pool of an immiscible liquid film on droplet impingement, the variation of the droplet and liquid film profile at the center points were evaluated (Figure

2.21). Both of the fluids deformed during the impact process. The droplet deformed substantially and rebounded after reaching its maximum spreading, and a small bubble formed within the inside of the water droplet during the rebounding stage. A slight increase in the height of the droplet and a decrease in the height of the liquid film were demonstrated this incident according to eject of bubble inside the water droplet. Finally, when the droplet detached from the liquid surface, the height of both fluids increased.

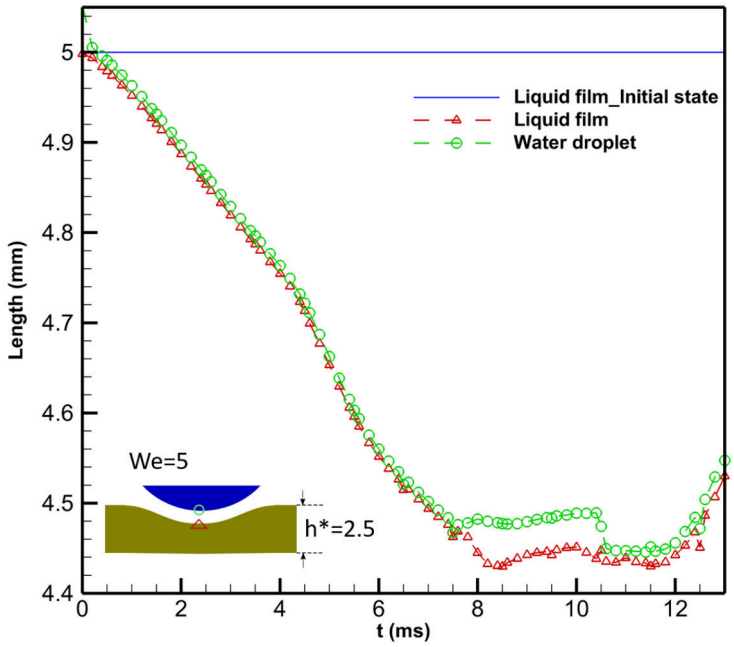

Figure 2.21: Profile of the water droplet and the liquid film at the center of impact over time ($We = 5$ and $h^* = 2.5$)

To better understand the effects of the entrapped air layer and its behavior, the air thickness (δ) was measured for the mentioned three liquid film thicknesses of $h^* = 0.025$, $h^* = 0.1$ and $h^* = 2.5$ at $We = 5$, which is shown in Figure 2.22. It is interesting to note that there is a decrease in the air layer thickness during the process of droplet approaching the surface (initial impingement), and the trend of this thickness change between runs is that $\delta_{h=50\mu m} < \delta_{h=200\mu m} < \delta_{h=5\,mm}$. It is also observed that the dimple height in higher liquid film thicknesses would be larger comparing to the introduced numerical correlation for the case of impact on solid surface [132]. This is likely because the thin liquid film was constrained by the solid surface, and the air layer was squeezed to a greater extent compared to the deep liquid pool case during the spreading stage. Afterward this approach, the thickness of the interfacial gas layer in the deep liquid pool decreased during the retracting stage. This is due to the easily deformed liquid surface that was adaptive to

the impact during the droplet impingement.

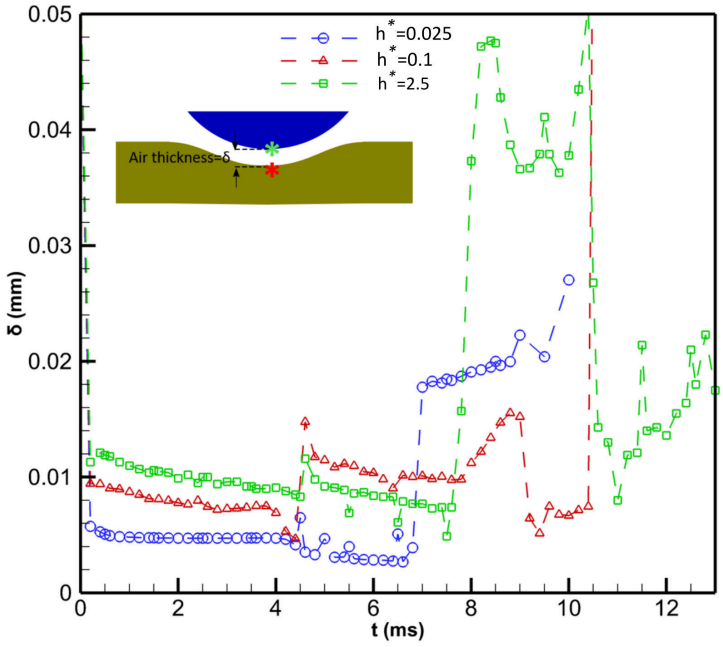

Figure 2.22: Air layer thickness over time for different liquid film thicknesses ($h^* = 0.025$, $h^* = 0.1$ and $h^* = 2.5$)

Additionally, Tang et al.[50] observed a similar trend in their recent experimental study using high-speed imaging and color interferometry. They showed that the air layer thickness decreased almost linearly with time for both thin and thick liquid layers. We found that the rebounding stage was dramatically different from the approaching stage. It is observed a substantial rapid increment in the air layer thickness for a deep pool of liquid film, which started slowing down after rebounding until the droplet detached from the liquid surface.

2.5 Conclusion

A three-phase flow solver has been developed to investigate the hydrodynamics change of a liquid film (lubricant) and the entrapped air layer during droplet impact and bouncing. The numerical model was validated against the analytical model based on the balance of the interfacial forces. In order to understand and characterize the nature of the air layer underneath the droplet, droplet impact on an immiscible liquid film at different film thicknesses and Weber numbers have been studied.

It was observed that at low Weber number ($We = 1.5$ and $h^* = 0.025$), despite the liquid film deformation, the hydrodynamics change of the droplet on a thin liquid film was similar to that on a solid surface which is caused by the presence of the air layer. For higher Weber number ($We = 10$), droplet sticks to the solid surface whereas on the liquid film, droplet detaches due to the local deformation of the liquid film interface caused by the entrapment of the air. For the liquid film in the deep pool regime, liquid deformation was more significant due to the diminished constraints of the solid surface on this thicker liquid film. Furthermore, in some cases, an air bubble was formed within the droplet during the retracting process, which also facilitated the droplet rebounding process. The numerical results can provide valuable guidelines for exploring the behavior of three-phase flow, especially in LIS.

Chapter 3

A comparison of bioinspired slippery and superhydrophobic surfaces: micro-droplet impact

[1]

3.1 Abstract

Slippery lubricant impregnated surfaces (SLIPS/LIS) exhibit remarkable features of repellency and droplet mobility to a broad range of complex fluids. Their performance in micro–droplet repellency has received less attention. In this study, the anti-wetting performance of SLIPS in comparison to superhydrophobic surface (SHS) are investigated for micro–droplet impact on different textured surfaces. Different series of square-pillar arrays are modeled to consider the effect of surface morphology on droplet hydrodynamics. A multiphase numerical model in conjunction with an accurate contact angle method has been implemented to analyze details of three immiscible phases during droplet impact on SLIPS. Our findings revealed that in SLIPS with low–density micro–textured surface where the effect of lubricant is more significant, droplet repellency and mobility is improved compared to SHSs. It was illustrated that in SLIPS, droplet pinning decreased significantly and in low Weber number cases where the effect of lubricant is more

[1] "Reproduced from Yeganehdoust, F., Attarzadeh, R., Dolatabadi, A., Karimfazli, I. (2021). A comparison of bioinspired slippery and superhydrophobic surfaces: Micro-droplet impact. Physics of Fluids, 33(2), 022105, with the permission of AIP Publishing".

noticeable, partial-bouncing occurred. It was also observed that slippery surfaces with a low–density of micro–pillars exhibit bouncing behavior which indicated the repellency effect of lubricant in droplet hydrodynamics. Although micro–droplet failed to recoil in higher Weber number ($We \simeq 160$) in both SHS and SLIPS, droplet penetration within the micro–structured surface was considerably smaller in SLIPS.

Keywords: Droplet impact, Slippery lubricant impregnated surfaces, Superhydrophobic surfaces, Micro-droplet

3.2 Introduction

Engineered surfaces with non–wetting behavior have broad applications in anti–icing and anti–frosting [133–135], anti– biofouling [136, 137] and condensation [31, 138, 139]. For instance, strikes of cloud-sized droplets which are mainly in micro–scale could result in frost formation that can ultimately change the airfoil aerodynamics and lead to serious performance degradation. Another significant application of micro–droplet impact is associated to respiratory droplets that are exhaled during talking, coughing, or sneezing. The average human exhales droplets are in the range of 1 μm–2000 μm. Small droplets ($< 5\ \mu m$) evaporate in a very short timescale (fraction of seconds). However, bigger micro–droplets can settle due to a slightly longer evaporation lifetime [140]. Therefore, pinning of the respiratory micro–droplets within the micro–structured surface are a critical factor in transmitting viral infections [140]. Thus, reducing the adhesion of micro–droplets could reduce the transmission of respiratory disease.

Liquid repellent surfaces could be a passive way for designing non–wetting surfaces. Superhydrophobic surfaces (SHSs) possess anti–wetting property as they are composed of hydrophobic surfaces with micro/nanometer–sized structures. The air is trapped within the textured surface due to surface tension and decreases contact angle hysteresis which can prevent the pinning of water droplet into the gaps of the surface.

Several experimental and theoretical analyses have been conducted regarding droplet impact on SHSs [55–59]. Numerical simulations have been also performed to elucidate the physics of droplet impact in SHSs [60] such as induced–jumping of droplets on SHS [116] or analyzing the effect of micro-textured surface in conditions where the ice formation occurred [61, 62]. For micro–scale droplets, the impact dynamics would be different compared to macro-scale droplets as the surface tension effect (capillary force) would be the dominant effect compared to inertial force in micro–droplets. Furthermore, the effect of

micro–structured surface on the outcome of droplet dynamics become more noticeable for micro–droplets. Though many experimental and numerical studies have been presented for macro–scale droplet impact on SHSs, few experimental studies have been dedicated to the impact of micro–scale droplet on SHSs ([63–65]). Despite various advantages of using superhydrophobic surfaces, they cannot be fully functional in many applications such as repellency of complex liquids with low surface tension, frost formation, and the presence of mechanical defects on the surface [71–73].

To improve issues associated with SHS, slippery lubricant impregnated surfaces (SLIPS/LIS) have been proposed [19]. These bio-inspired engineered surfaces have been developed such that the air pockets are replaced by impregnating a low surface tension liquid film within the micro-structured surface. The liquid oil can completely spread and wet the textured surface via capillary force which results in a smooth and homogeneous surface with high slippery features due to very small contact angle hysteresis [30, 141]. The SLIPS exhibits self-cleaning, anti-icing, anti–biofouling properties and are also able to repel various liquids with lower surface tension than water [133, 142, 143]. They have also shown promising performance in droplet manipulation in microfluidics systems [144] or reducing the frictional drag because of their enhanced stability against high-pressure environments [20, 145].

To achieve slippery surfaces, the liquid oil should also act as an immiscible liquid against liquid droplet [19]. Smith et al. [30] reported three different states of droplet and lubricant based on the interfacial tension between water/oil/air. The oil can be in an encapsulated state at which a thin liquid film of lubricant exists on oil-infused micro-pillars surface. Otherwise, the oil can become impregnated into the micro-structured surface [30] (as shown in Figure 3.1b). Although the encapsulated status would be more thermodynamically favorable [30], this might result in excessive lubricant depletion. It has been shown that the lubricant layer would resist large static pressure and repels various kinds of liquid including those with low surface tensions. Previous studies have also demonstrated that slippery surfaces can limit ice formation [133, 142]. Unlike air-infused superhydrophobic surfaces, it was found that the lubricant layer can restore after abrasion and impact of liquids [19]. Thus, lubricant can self-heal once defects occur on the surface due to the presence of oil within the porous structure and capillarity [146, 147]. This would increase mechanical stability in SLIPS comparing to the SHS. However, few studies have been dedicated to the performance of SLIPS for millimeter/micrometer-sized droplet impact.

Kim and Rothstein [81] investigated the spreading and retraction dynamics of droplet impact on SLIPS

with randomly rough micro–structures which were infused with different silicone oils of different viscosities. They found an increase in maximum spreading diameter and the retraction velocity by reducing the viscosity of the infused silicone oil layer. For the lowest viscosity of oil, small changes in either the dynamic advancing or the receding contact angle were observed. Muschi et al. [148] evaluated the effect of oil thickness on the wetting properties and drop impact dynamics on SLIPS. They used a spin-coating technique for tuning the oil thickness to reach a homogeneous distribution of liquid oil. They observed that droplet spreading, or the bouncing dynamics were not strongly affected by the oil thickness if the infused oil layer at the surface is mostly homogeneous. Lee et al. [82] studied droplet impact dynamics on the oil-infused nano-structured surface. They observed that the oil viscosity can determine the stability of the infused lubricant oil during the drop impact and the low viscous oil layer can be displaced by the impacting droplet. They have also reported different instabilities during droplet impact for high Weber numbers. Designing robust and sustainable slippery surfaces is essential to use the maximum of their features. Recent studies have been more devoted to the study of more robust and stable slippery surfaces [1, 96, 149, 150]. Different parameters such as the surface morphology, lubricant, and surface properties can significantly affect SLIPS performance. There have been few computational and experimental studies on the effect of surface morphology in Slippery lubricant impregnated surfaces.

In the present work, we aim to elucidate the non–wetting performance of the slippery surfaces compared to superhydrophobic surfaces for micro–droplet impact (typical droplet size in in–flight icing or respiratory system) using numerical analysis. Different surface morphologies and impact velocities were studied. For SLIPS, a layer of lubricant was infused within the micro-structured surface while there is air within the micro–structured surface in superhydrophobic surfaces. The qualitative and quantitative comparison of droplet impact hydrodynamics and the effect of surface morphologies were studied using the numerical approach. Furthermore, a map that indicates different states of the droplet is presented based on different surface morphology and impact conditions.

3.3 Problem set–up

In the current study, a three-dimensional numerical model of the droplet impact on slippery lubricant impregnated surfaces in comparison with superhydrophobic surfaces have been studied. A micro-droplet with a size of $D_0 = 30\ \mu m$ was used in the present study to resemble the size of respiratory droplets or the

supercooled droplet which mostly initiates ice formation over critical surfaces [62].

In superhydrophobic cases, surfaces were composed of micro–structured arrays with square cross-sectional pillars. Figure 3.1a illustrates a schematic image of the micro–structure used in the current study in which the size of micro-pillars is $2\ \mu m \times 2\ \mu m \times 2\ \mu m$. For SLIPS, the air within the pillars of SHS was replaced by an immiscible lubricant to make a slippery surface (Figure 3.1b).

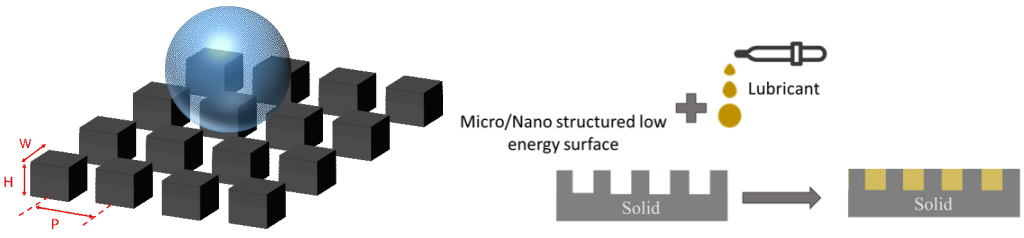

(a) (b)

Figure 3.1: A schematic of (a) superhydrophobic surface (with the surface pattern of "$nwmp$" where "w" and "p" denote the width and pitch size (in μm) of pillars) and (b) slippery lubricant impregnated surface

The impregnated/emerged state was considered in all SLIPS impact conditions to reduce the probability of lubricant depletion [30]. The Krytox GPL 101 was used in the present work [151]. The physical and chemical property of oil can completely wick the low surface energy surface and increase the mobility of working liquid on the surface [19, 30]. The physical properties of lubricant (Krytox GPL101), water droplet and surrounding air are listed in Table 3.1. The interfacial tension between water–oil is considered as $\gamma_{\text{wo}} = 0.053\ (mN/m)$.

Table 3.1: Physical properties of fluids

Fluids	**Density**($^{kg}/_{m^3}$)	**Kinematic viscosity**(cSt)	**Surface tension**($^{N}/_{m}$)
Dupont KrytoxGPL 101	1850	17.7	0.017
Water	1000	1	0.072
Air	1.2	15	-

In all cases, the surface properties are chosen to represent a surface which is coated with a thin layer of stearic acid relevant to experimental studies [62, 152, 153]. The equilibrium, advancing, and receding contact angles of a droplet on a smooth flat surface that is coated with stearic acid have been measured as $\theta_E = 111°$, $\theta_A = 120°$ and $\theta_R = 86°$, respectively. The effect of surface topology was assessed by considering different patterns of the micro–pillar arrangements. To distinguish the pattern of micro–pillars,

each pattern was identified in a template of "$nwmp$" as shown in Figure 3.1a, where "n" and "m" denotes the width and pitch size of the micro–pillar. In all cases, the width and height of the pillars were consistent while the pitch of pillars changed, $m = 3$, 5, and 7 μm. The combination of a hydrophobic coated layer of stearic acid and a textured surface provided non–wetting surface depending on the pattern of the textured surface and initial impact conditions.

Since both the textured surface and droplet are in micro–scale, a dimensionless number of ξ was introduced as $\xi = {}^{p}/_{D0}$ to describe the surface morphologies on droplet dynamics. Thus, considering $30\mu m$ droplet, three patterns of $2w3p$ ($\xi = 0.1$), $2w5p$ ($\xi = 0.17$) and $2w7p$ ($\xi = 0.23$) have been investigated. The initial geometry, the boundary condition of the domain, and mesh distribution are illustrated in Figure 3.2. The geometry domain is considered for a quarter of droplet and substrate and the symmetry boundary condition is applied on two faces. All the cases were simulated in an isothermal condition. The micro–droplet was located in the center of the computational domain with a size of $4R_0 \times 4R_0$ and 100 cells per droplet diameter. The top surface is subjected to the atmosphere. A boundary condition of atmospheric pressure with no gradient effect of velocity is considered. A no-slip boundary condition is applied to the bottom and side surfaces of the geometry while the gradient effect of the pressure is considered as zero. The cell size in the refined region (as shown in Figure 3.2) is approximately 300 nm and around $2M$ cells were considered in the model. The computational simulations were done in parallel with the 24 processor. The run time was approximately 30 hours for each simulation.

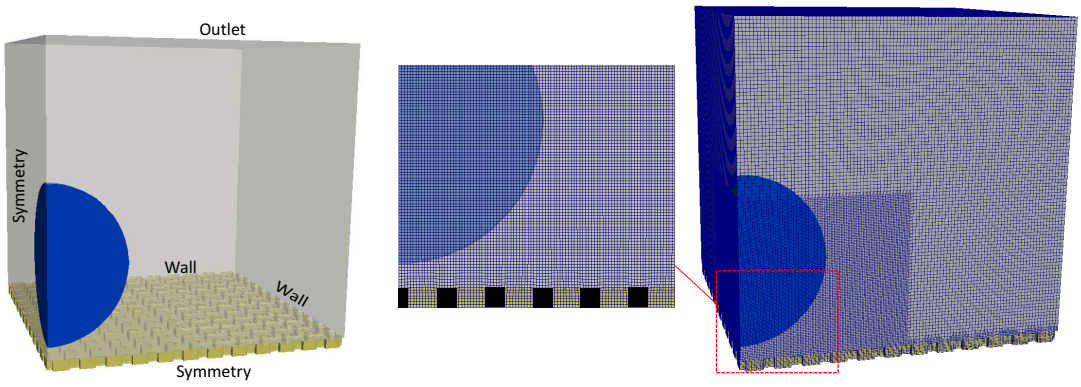

(a) (b)

Figure 3.2: (a) The initial geometry and (b) mesh distribution of the computational domain for droplet impact on SLIPS (for instance, $2w5p$)

3.4 Computational approach

Slippery surfaces involve three phases of air, water droplet, and infused lubricant within the micro–pillar surfaces. A three-phase flow solver based on the volume of fluid (VOF) method in OpenFOAM [45, 128] was used in conjunction with a modified contact angle model. Amidst different interface tracking methods [125, 126, 154, 155], the VOF scheme was used in this study due to its accuracy, ability in capturing the interfaces between multiple phases, and its inherent capability in the calculation of the surface tension [45].

3.4.1 Governing equations

For an incompressible, newtonian, laminar flow, the governing equations are given as follows,

$$\nabla \cdot \overrightarrow{U} = 0 \tag{3.1}$$

$$\frac{\partial \rho \vec{U}}{\partial t} + \nabla \cdot \left(\rho \vec{U} \vec{U}\right) = -\nabla P + \left[\nabla \cdot [\mu(\frac{\nabla \vec{U} + \nabla \vec{U}^T}{2})\right] + \rho \cdot \vec{g} + \overrightarrow{F_s}, \tag{3.2}$$

where ρ, μ, U and P are the density, dynamic viscosity, velocity field, and pressure of the flow, respectively. $F_s = \sigma \kappa \hat{n} \delta$ is the surface tension force based on the continuum surface force (CSF) [127].

Regarding the VOF method for tracking each phase interface, a volume fraction α_i is introduced in which the value of $i = 1, 2, 3$ that represents air, water and oil, respectively. The value of α_i is in the range between 0 and 1 and the physical properties of phases are defined based on the volume fraction average of all fluids in the cell. Thus, density and viscosity would be $\rho = \sum_{i=1}^{3} \alpha_i \rho_i$ and $\mu = \sum_{i=1}^{3} \alpha_i \mu_i$.

The volume fraction is advected by transport equation and the evolution of the interface was computed as follows,

$$\frac{\partial \rho \alpha_i}{\partial t} + \nabla \cdot \left(\overrightarrow{U} \alpha_i\right) + \nabla \cdot \left(\overrightarrow{U}_r \alpha_i \left(1 - \alpha_i\right)\right) = 0. \tag{3.3}$$

Generally in the VOF solvers, the interface between phases is smeared over several cells. U_r is an artificial compression velocity at the free surface that acts normal to the interface to compress the free surface and counteract the numerical diffusion and maintain a sharp interface [156]. U_r is defined in Equation 3.4,

$$\overrightarrow{U}_r = \left(\min\left(C_{\alpha_i} \left|U\right|, \max\left(\left|U\right|\right)\right)\right) \frac{\nabla \alpha_i}{\left|\nabla \alpha_i\right|}, \tag{3.4}$$

where C_{α_i} is the compression coefficient that determines the degree of compression. The surface tension force for the case of three-phase flows is calculated as $F_s = \sum_{i=1}^{3}\sum_{j\neq i}^{3}\sigma_{ij}\kappa_{ij}\delta_{ij}$, where σ_{ij} and κ_{ij} are the physical interfacial tension and the curvature between the two phases of i and j, respectively. Since the surface curvature is calculated using the Dirac delta function [45, 120], the general form of interfacial tension force is as follows,

$$F_s = -\sum_{i=1}^{3}\sum_{j\neq 1}^{3}\sigma_{ij}(\nabla\cdot(\frac{\alpha_j\nabla\alpha_i - \alpha_i\nabla\alpha_j}{|\alpha_j\nabla\alpha_i - \alpha_i\nabla\alpha_j|}))(\alpha_j\nabla\alpha_i - \alpha_i\nabla\alpha_j). \tag{3.5}$$

The multiphase model was verified previously for three–phase flow systems [45, 83]. In conjunction with the three-phase flow model, a dynamic contact angle method (Kistler method) [157] was extended for three immiscible liquid phases. This method is one of the accurate methods in modeling dynamic contact angle [158]. In the Kistler method, the dynamic contact angle (θ_D) is described as a function of contact line velocity through Capillary number,

$$\cos\theta_D = 1 - 2\tanh\left(5.16\left[\frac{\mathrm{Ca}+\mathrm{fHl}}{1+1.31(\mathrm{Ca}+\mathrm{fHl})^{0.99}}\right]^{0.706}\right) \tag{3.6}$$

$$\mathrm{fHl}^{0.706} = \frac{1}{5.16}\left[1+1.31\mathrm{fHl}^{0.99}\right]^{0.706}\tanh^{-1}\left[\frac{1-\cos\theta_E}{2}\right], \tag{3.7}$$

where θ_E is the equilibrium contact angle. Ca is the capillary number, $Ca = \frac{\mu U_{cl}}{\sigma}$ where U_{cl}, μ and σ are the spreading velocity of the contact line, the dynamic viscosity and the surface tension of the liquid. fHl is the empirical Hoffman's function. The equilibrium angle (θ_E) is then replaced by either an advancing or receding contact (θ_A or θ_R) respectively, depending on the sign of the velocity vector at the contact line. In the present study which involved three–phase flow systems in SLIPS, the dynamic contact angle was implemented based on the initial contact angle conditions (θ_A or θ_R) and physical properties of phases. The accuracy of the numerical model for three–phase flow system was assessed and illustrated in Appendix B. The results indicated that the numerical model is capable of predicting droplet dynamics for three immiscible liquids which can be applied to SLIPS.

3.5 Results and discussion

The performance of slippery surfaces in comparison to superhydrophobic surfaces is evaluated for micro–droplet impact with three different Weber numbers ($We = \frac{\rho {U_0}^2 D_0}{\sigma}$) of $We = 10.4, 41.7$ and 166.7 on surface patterns of $\xi = 0.1, 0.17$ and 0.23. Then, the effect of surface morphology is quantitatively demonstrated.

For high-density micro–textured surface of $2w3p$ ($\xi = 0.1$), the effect of Weber number on droplet hydrodynamics in both cases of SHS and SLIPS is shown in Figure 3.3. Three different Weber number ($We = 10.4, 41.7$ and 166.7) were investigated to observe the performance of $\xi = 0.1$ for different impact conditions. All snapshots of droplet impact at different Weber numbers are illustrated in dimensionless time number ($t^* = \frac{tU_0}{D_0}$) which is defined as $t^* = \frac{tU_0}{D_0}$. The interface of water droplet and lubricant as well as the velocity magnitude distribution of phases are shown. At $We = 10.4$ (Figure 3.3(a)) droplet exhibits complete bouncing for SHS while droplet remains on the surface for SLIPS case.

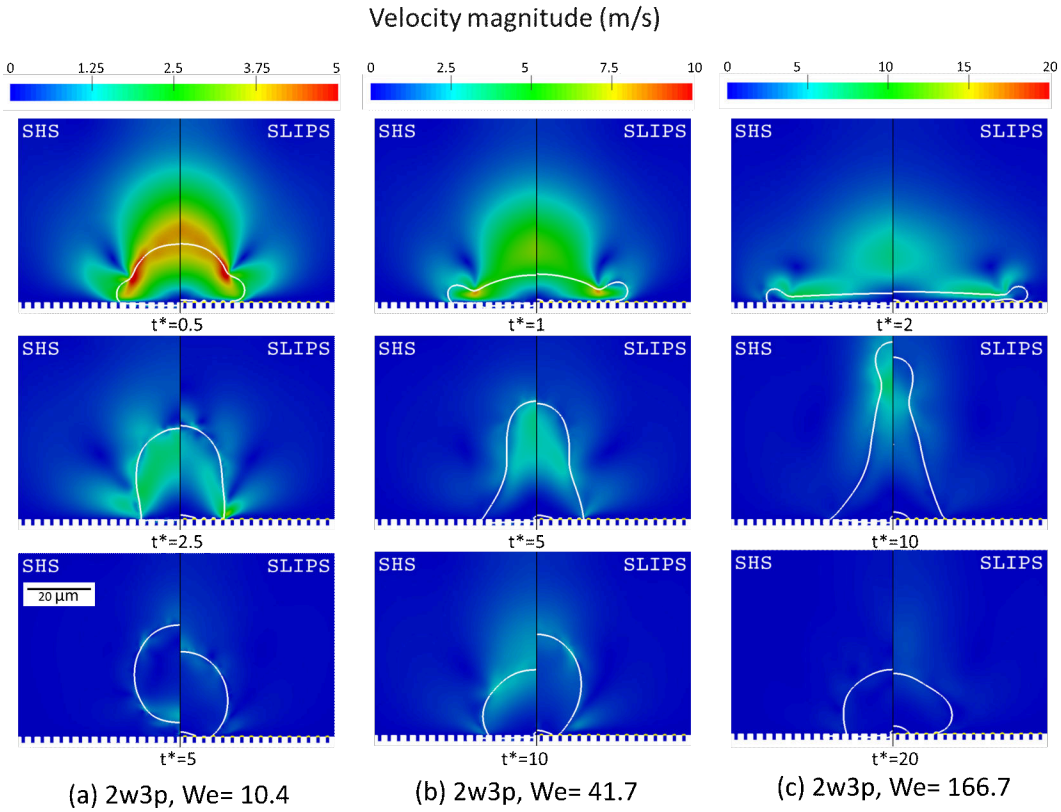

Figure 3.3: Comparison of of micro–droplet impact on SHS and SLIPS for $2w3p$ ($\xi = 0.1$) textured pattern with different Weber numbers of: column (a) $We = 10.4$, column (b) $We = 41.7$ and column (c) $We = 166.7$- Solid white line: Water droplet interface, Solid yellow line: Lubricant interface

Generally, droplet bouncing/non-bouncing can be theoretically predicted in SHS by comparing the dynamic pressure against capillary pressure [55, 59]. The emergence i.e. different regimes of complete bouncing, partial bouncing and wetting depends on the balance of capillary pressure (P_C) and dynamic pressure (P_D) which are estimated as $P_C = 4\gamma \cos\theta_a \left(\frac{\phi}{w(1-\phi)}\right)$ where $\phi = \frac{w^2}{p^2}$, and $P_D = 0.5\rho V^2$ for a square-pillar micro–structured surface [55]. Accordingly, in the current case of SHS ($\xi = 0.1$), it is also expected that droplet results in complete–bouncing as capillary pressure is approximately 5 times the dynamic pressure. For higher impact velocity ($We = 41.7$ and $We = 166.7$), as shown in the Figure 3.3 b and c, droplet started penetrating within the micro–pillars in SHS as the kinetic energy increased. In SLIPS with a high density of square pillars, it can be seen in Figure 3.3 that droplet remained on slippery surfaces at all Weber numbers. SLIPS cases in high–density textured surface ($\xi = 0.1$) behaved similarly to the flat smooth solid surface and the effect of lubricant was not significant. Although both SHS and SLIPS revealed non–bouncing behavior in higher Weber numbers ($We = 41.7$ and $We = 166.7$), droplet remained on top of the textured surface in the SLIPS, unlike SHS which shows complete pinning within the micro–pillars (Figure 3.3). To better understand the droplet dynamics in different Weber numbers for the $2w3p$ surface structure, zoom-in views of the region near micro–pillars (stretched in vertical direction by a factor of 3) are illustrated in Figure 3.4.

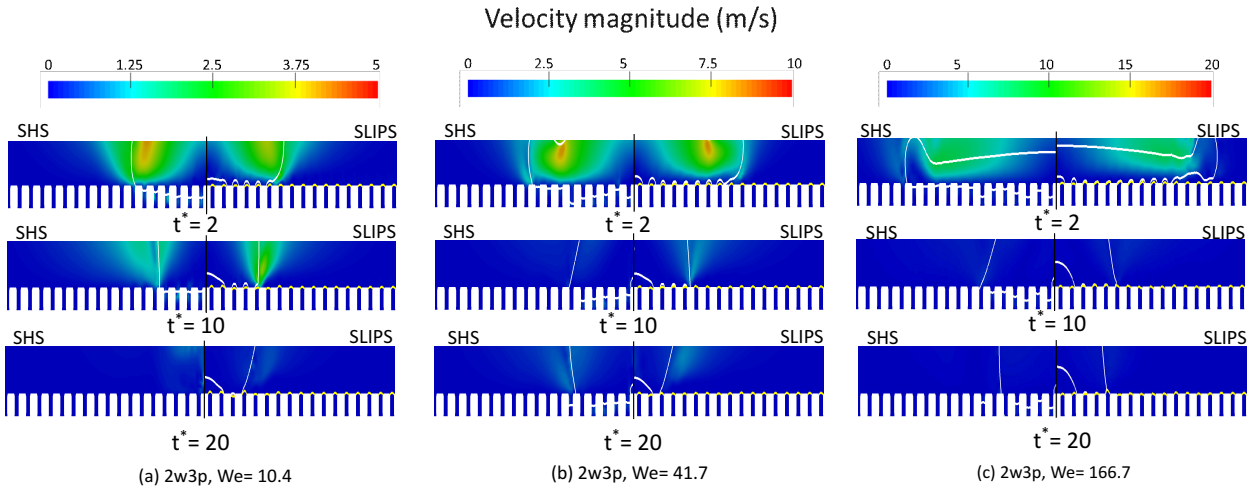

Figure 3.4: The magnified images near the substrate region for micro–droplet impact on SHS and SLIPS for $2w3p$ ($\xi = 0.1$) textured pattern with different Weber numbers of: column (a) $We = 10.4$, column (b) $We = 41.7$ and column (c) $We = 166.7$- Solid white line: Water droplet interface, Solid yellow line: Lubricant interface- The images are stretched in vertical direction by a factor of 3

Next, the pattern of textured surface was changed by increasing the pitch length to $5\mu m$ ($\xi = 0.17$).

A comparison of droplet impact on SHS and SLIPS for three Weber number ($We = 10.4, 41.7$ and 166.7) is illustrated (Figure 3.5). More details on droplet and lubricant near the micro–pillars regions are shown in Figure 3.6. It can be seen in Figure 3.5 that droplet fails to bounce off the surface for all cases in SHS. Thus, the non–wetting property of superhydrophobic surfaces is considerably restricted and sensitive to the arrangement of micro–pillars. As the space between micro–pillars increased, the effect of lubricant in SLIPS cases was more pronounced than the previous case. At $We = 10.4$, droplet remained on the surface for the SLIPS case while the liquid oil layer prevented droplet from penetrating the gaps within micro–pillars (as illustrated in Figure 3.6). It can be observed that once the kinetic energy increased and Weber number raised to $We = 41.7$ (Figure 3.5 (b)), partial bouncing occurred and most parts of the droplet recoiled from the surface and only a small droplet remained on the surface. In higher Weber number ($We = 166.7$), droplet broke up during the receding stage and finally remained on the surface as shown in Figure 3.5 (c). In all SLIPS cases, the lubricant is maintained within the micro–pillars while the droplet stayed on top of the asperities even at a higher Weber number.

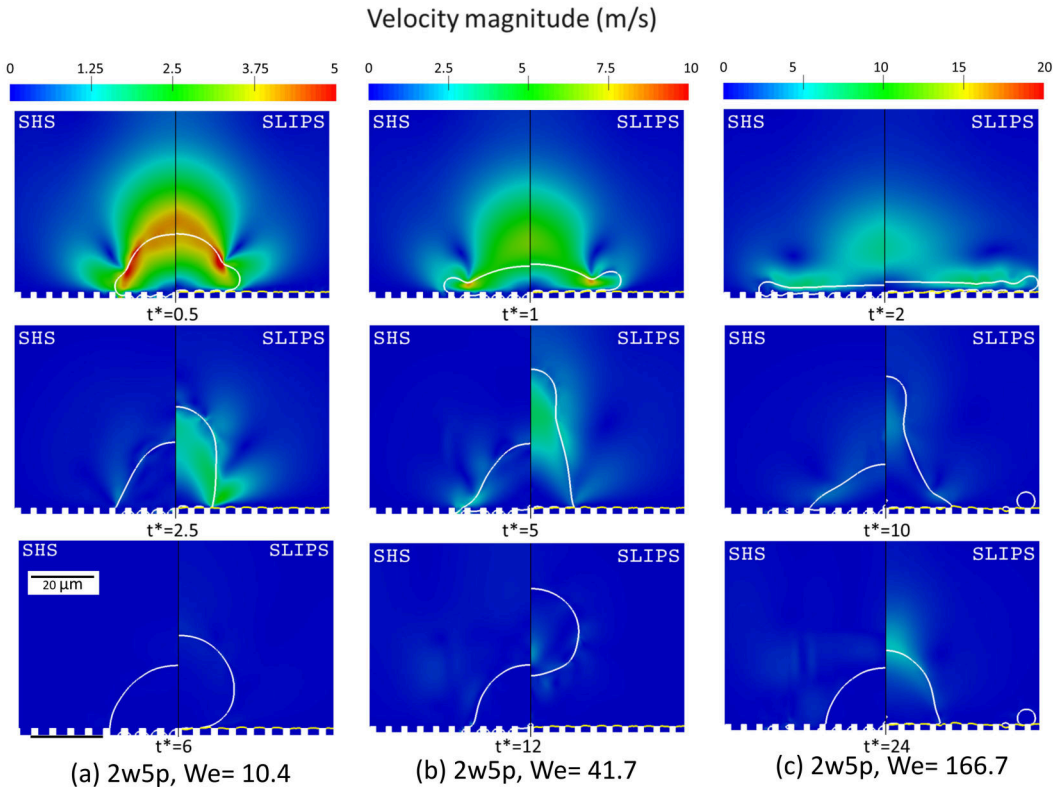

Figure 3.5: Comparison of of micro–droplet impact on SHS and SLIPS for $2w5p$ ($\xi = 0.17$) textured pattern with different Weber numbers of: column (a) $We = 10.4$, column (b) $We = 41.7$ and column (c) $We = 166.7$- Solid white line: Water droplet interface, Solid yellow line: Lubricant interface

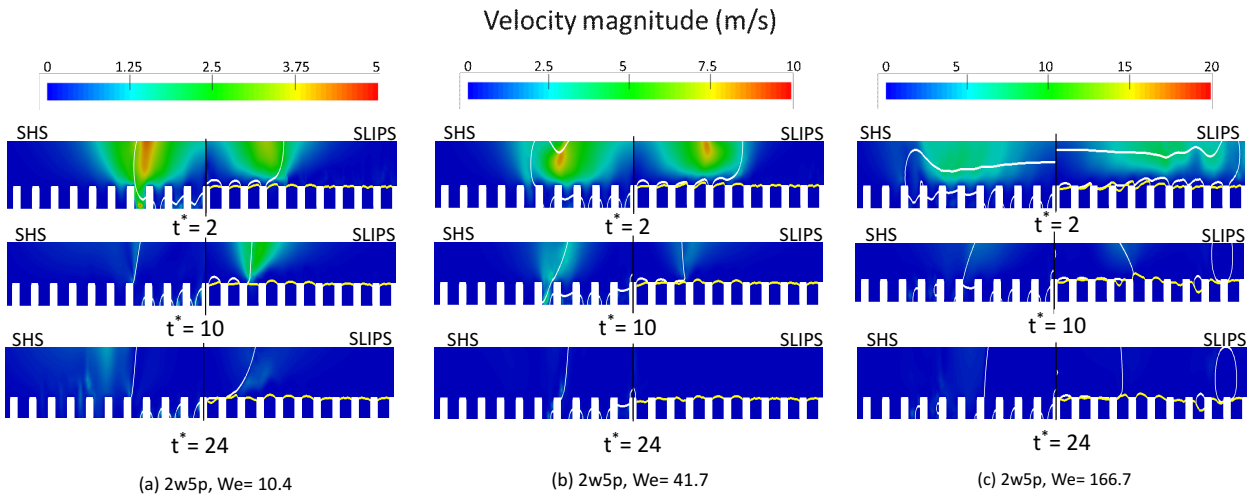

Figure 3.6: The magnified images near the substrate region for micro–droplet impact on SHS and SLIPS for $2w5p$ ($\xi = 0.17$) textured pattern with different Weber numbers of: column (a) $We = 10.4$, column (b) $We = 41.7$ and column (c) $We = 166.7$- Solid white line: Water droplet interface, Solid yellow line: Lubricant interface- The images are stretched in vertical direction by a factor of 3

Finally, the hydrodynamics of droplet impact on SHS and SLIPS with low-density micro–textured surface ($2w7p$ or $\xi = 0.23$) for three different Weber numbers ($We = 10.4, 41.7$ and 166.7) have been evaluated (Figure 3.7). It can be seen in Figure 3.7 that SHS still failed in droplet recoiling in all three cases. In $\xi = 0.23$ cases, slippery surfaces are composed of low–density of micro–textured surface which specifies that more oil is presented in the system compared to other cases ($\xi = 0.17$ and $\xi = 0.1$). This leads to the air entrapment formation between droplet and lubricant (Figure 3.8 and 3.9) and results in preventing the droplet from pinning to the surface and droplet bouncing in SLIPS with the morphology of $2w7p$ ($We = 10.4$ and $We = 41.7$).

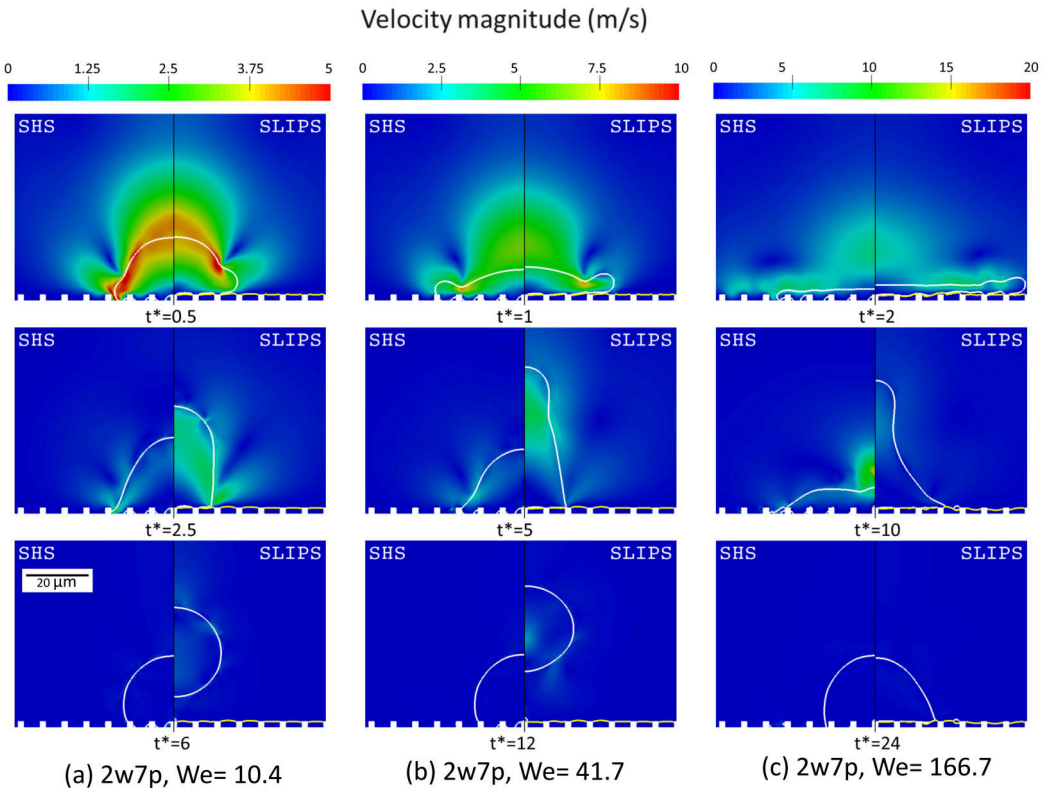

Figure 3.7: Comparison of of micro–droplet impact on SHS and SLIPS for $2w7p$ ($\xi = 0.23$) textured pattern with different Weber numbers of: column (a) $We = 10.4$, column (b) $We = 41.7$ and column (c) $We = 166.7$- Solid white line: Water droplet interface, Solid yellow line: Lubricant interface

For higher impact velocity ($We = 166.7$), it can be seen in Figure 3.7(c) that droplet splashed into small droplets and remained on the surface while the droplet completely penetrated within the pillars for SHS case. In addition, it is clearly shown in column (c) that despite the large space between micro–pillars, the lubricant did not fail its effectiveness in SLIPS cases and it was not displaced by water droplet noticeably.

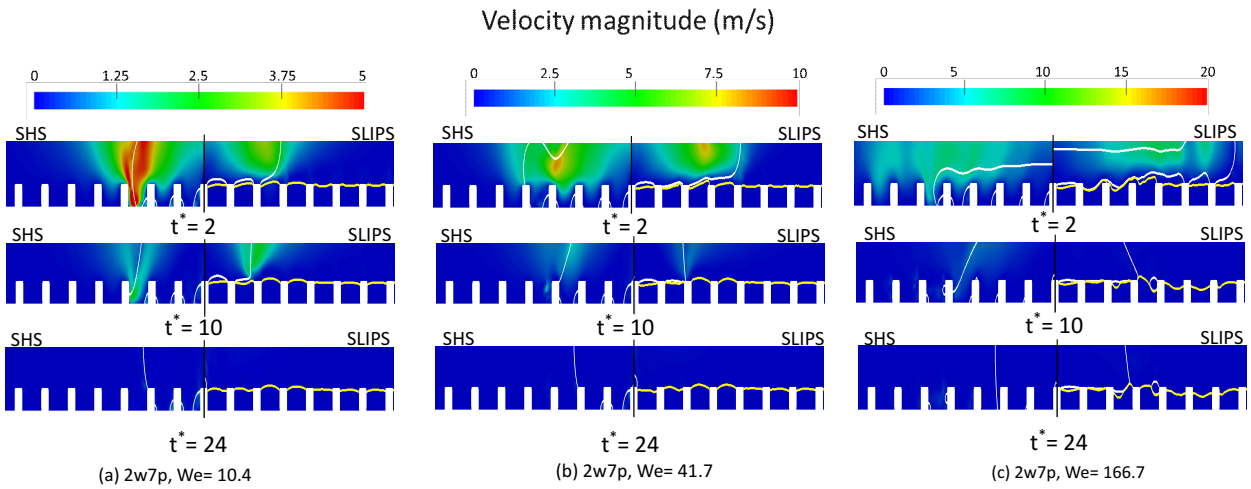

Figure 3.8: The magnified images near the substrate region for micro–droplet impact on SHS and SLIPS for $2w7p$ ($\xi = 0.23$) textured pattern with different Weber numbers of: column (a) $We = 10.4$, column (b) $We = 41.7$ and column (c) $We = 166.7$- Solid white line: Water droplet interface, Solid yellow line: Lubricant interface- The images are stretched in vertical direction by a factor of 3

It is worth noting that during the spreading stage of droplet impingement in all SLIPS cases, droplet deformed into a dimple shape in the regions near the impregnated lubricant. Figure 3.9 demonstrates the magnified image of droplet impact at $We = 10.4$ on SHS and SLIPS ($\xi = 0.1$ and $\xi = 0.23$) at $t^* = 0.5$. It can be seen that within the few milliseconds of droplet impingement, both droplet and lubricant are deformed.

In SHS, the air is entrapped at $We = 10.4$, $2w3p$ while it gradually collapsed for higher Weber number cases ($We = 41.7$ and $We = 166.7$). For SLIPS, the immiscible liquid film prevents the droplet from penetrating within the micro–asperities while due to the lubricant deformation, the air entrapment occurs in the regions between droplet and lubricant. This was also observed for the millimeter size droplet impact on immiscible liquid film [45, 50]. It can be seen that for the small size of pitch ($\xi = 0.1$), the lubricant deformation is small compared to the large ξ (low–density textured surface).

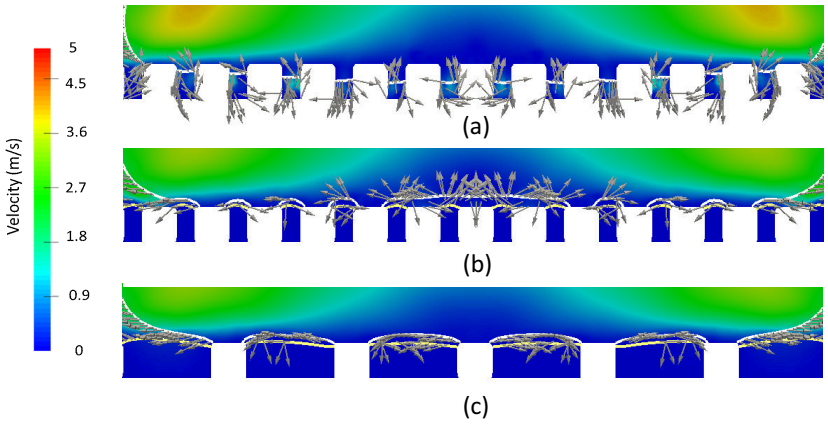

Figure 3.9: The magnified image of water droplet deformation and air entrapment during droplet impingement at $We = 10.4$ on (a) SHS, (b) SLIP-$2w3p$ and (c) SLIP-$2w7p$

To further elucidate the underlying mechanisms, few snapshots of the three–dimensional view of droplet interface impact on SLIPS and SHS at $We = 10.4$ are illustrated in Figure 3.10. It can be seen that for SHS, droplet penetrates within the micro–pillars during the spreading stage ($t^* = 1$), as the magnified image is also shown. For SLIPS, no significant droplet penetration occurs which results in less contact time of droplet in the SLIPS ($2w7p$) compared to SHS. The air entrapment during impact especially in the spreading stage of SLIPS can be observed in Figure 3.10 (the magnified image of the droplet interface at $t^* = 1$). Consequently, this would inhibit droplet from pinning into micro–structured surface.

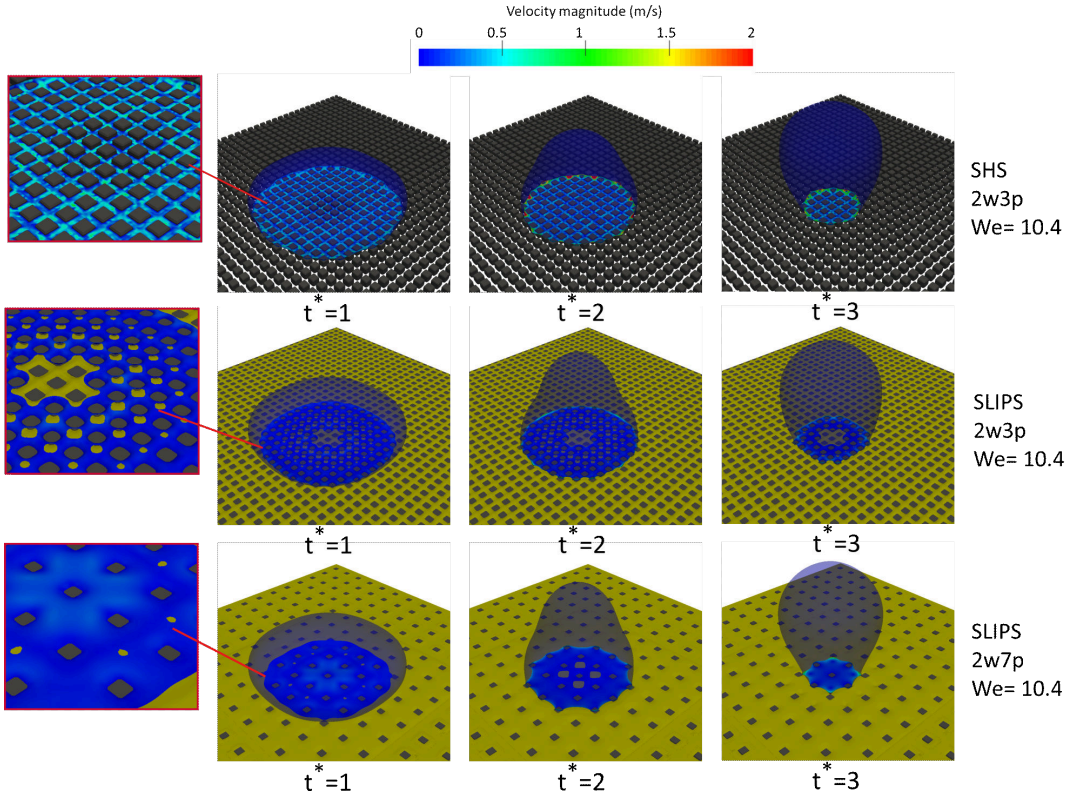

Figure 3.10: Droplet interface velocity at $We = 10.4$ during droplet impact on : First row: SHS, Second row: SLIPS ($2w3p$) and Third row: SLIPS ($2w7p$)–The yellow color in the droplet interface indicates the air entrapment between droplet and lubricant in SLIPS

3.5.1 Quantitative characterization of micro–droplet impact

As the surface structure can be a significant parameter in designing a robust slippery surface, quantitative characterizations are required to study the effect of surface morphology on SLIPS performance. In this regard, some key dimensionless parameters including the β, δ^* and U^* that are denoted as spreading factor, dimensionless droplet penetration depth, and average normal velocity (coefficient of restitution), respectively, are investigated. These parameters would provide more information on droplet wetting length, the rate of droplet pinning within the textured surface, and droplet kinetic energy during impingement on slippery surfaces.

Spreading factor

Spreading factor is the ratio of droplet diameter to the initial diameter ($\beta = \frac{D}{D_0}$) which is an important quantitative parameter that could represent surface wettability during droplet impact. Figure 3.11 illustrates

how the spreading factor (β) is affected by different patterns of micro–pillars ($\xi = 0.1, 0.17$ and 0.23) in both SHS and SLIPS. The spreading factor is illustrated for superhydrophobic surface at $We = 10.4$ in Figure 3.11a. It can be observed that in surface morphology of $\xi = 0.1$, β reduced significantly during the receding stage which denotes the bouncing behavior of droplet. It can be seen in Figure 3.11a that $\beta_{\xi=0.23} < \beta_{\xi=0.17}$.

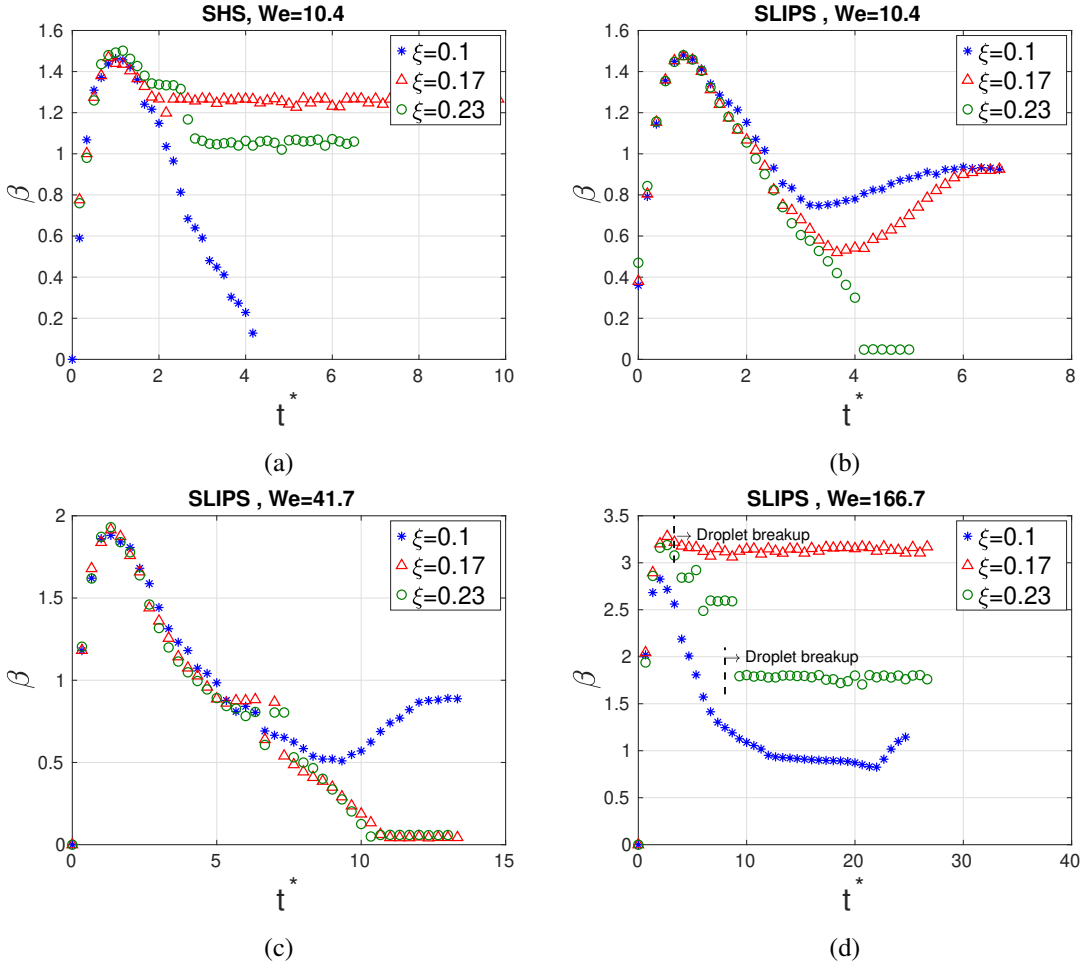

Figure 3.11: Comparison of spreading factor (β) during droplet impact for different surface patterns ($\xi = 0.1$, 0.17 and 0.23) on (a) SHS, $We = 10.4$ (b) SLIPS, $We = 10.4$ (c) SLIPS, $We = 41.7$ and (d) SLIPS, $We = 166.7$

The higher amount of β during the receding stage in $\xi = 0.17$ compared to the $\xi = 0.23$ is due to the higher number of micro–pillars in $\xi = 0.17$ which made obstacles and impede the droplet movement. In SLIPS at $We = 10.4$ (Figure 3.11b), it can be seen that the all three ξ shows same behavior during the spreading stage. However, for low-density of micro–pillars ($\xi = 0.23$), β decreased significantly as partial bouncing occurred, while β in $\xi = 0.1$ is the highest during the receding stage (after $t^* = 4$). Figure 3.11c

demonstrates the effect of surface morphologies (ξ) on β for SLIPS at $We = 41.7$.

It can be seen that the spreading factor for both $\xi = 0.17$ and $\xi = 0.23$ decreases significantly comparing to the case of $\xi = 0.1$ which indicates that both surfaces result in partial bouncing. For higher Weber number ($We = 166.7$) in slippery surface as shown in Figure 3.11d, droplet disintegrates into small droplets in $\xi = 0.17$ and $\xi = 0.23$ once the droplet starts receding. For $\xi = 0.1$, no break-up occurred as the textured surface is more analogous to a smooth solid surface. From the spreading results, it can be deduced that due to the presence of lubricant and inertial force effect, β is not affected significantly by the surface morphology during the spreading stage. The spreading factor is approximately similar for different surface structures in SLIPS (except $We = 166.7$ where the droplet broke up). The energy dissipation gradually changes the speed of β and the outcome of droplet dynamics. Thus, slippery surfaces with low density textured resulted in partial bouncing. It can be also observed that even in cases where no bouncing/partial bouncing occurred (Figure 3.11b, $\xi = 0.17$ and $\xi = 0.23$), the reduction in β is still discernible.

Droplet penetration depth

In many applications such as anti–biofouling, anti-icing or condensation, it is critical to have droplets on top of the surface to slide more easily on the surface without pinning to the textured surface. In superhydrophobic surfaces, micro–scale sized droplets tend to penetrate within the micro–textured surfaces which would result in breaking down the non–wetting property. In this regard, the dimensionless maximum depth of droplet penetration within the textured surface (δ^*) has been evaluated quantitatively which is defined as $\delta^* = {}^{\delta_{\max}}/_{h}$. $\delta_{\max}$ is measured based on the maximum value of droplet penetration depth through the whole micro–pillars and h is the height of micro–pillars. A schematic of parameter $\delta_{\max}$ is shown in Figure 3.12.

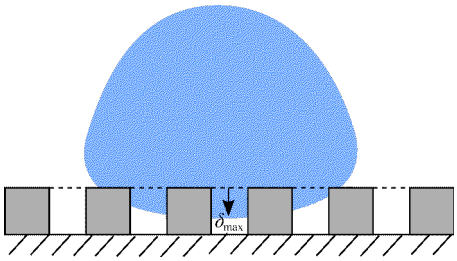

Figure 3.12: A schematic of droplet penetration depth ($\delta_{\max}$) within the micro-pillar surface

Figure 3.13 demonstrates the effect of surface morphology on the pinning of droplet within the micro–pillars in SHS and SLIPS. For this purpose, δ^* was measured in SHS and SLIPS for three $\xi = 0.1, 0.17$

and 0.23. Since the height of pillars is $2\mu m$ in all cases, the dimensionless number of $\delta^* = 1$ indicated that droplet completely penetrated within micro–pillars. Figure 3.13a demonstrates droplet penetration depth within the pillars on SHS for low Weber number ($We = 10.4$). The results indicated that the droplet was completely infused through the micro–pillars for $\xi = 0.17$ and 0.23 which implied that SHS cannot be functional. It can be seen that although complete bouncing occurred in SHS ($\xi = 0.1$), δ^* reached to 0.6 during impingement which is more than the case on slippery surfaces. For SLIPS at $We = 10.4$ (Figure 3.13b), δ^* is slightly higher in $\xi = 0.23$ and $\xi = 0.17$ comparing to $\xi = 0.1$ until $t^* = 4$. Since partial– bouncing occurred in $\xi = 0.23$, δ^* reduced to almost zero. For higher impact velocity of SLIPS ($We = 41.7$), it can be seen that δ^* during impact would be as ${\delta^*}_{\xi=0.23} > {\delta^*}_{\xi=0.17} > {\delta^*}_{\xi=0.1}$ until partial–bouncing occurred in $\xi = 0.23$ and $\xi = 0.17$. For $We = 166.7$ of SLIPS cases as illustrated in Figure 3.13d, δ^* in $\xi = 0.23$ is higher during the spreading stage ($t^* = 3$). Since the kinetic energy of droplet was increased, the lubricant within the micro–textured surfaces with larger ξ are more susceptible to impact. Thus, the oscillation of droplet deformation is more noticeable during the impingement process. This resulted in breaking up the droplet into small droplets during the receding stage and δ^* increased to approximately 0.6 while droplet completely infused within the micro–pillars of SHS as it can be seen in Figure 3.5 and Figure 3.7. It can be deduced that δ^* in SLIPS is considerably small (less than 20% for $We = 10.4$ and 41.7 and less than 60% for $We = 166.7$) compared to SHS. Thus, SLIPS can be a promising method to prevent droplet pinning within the asperities.

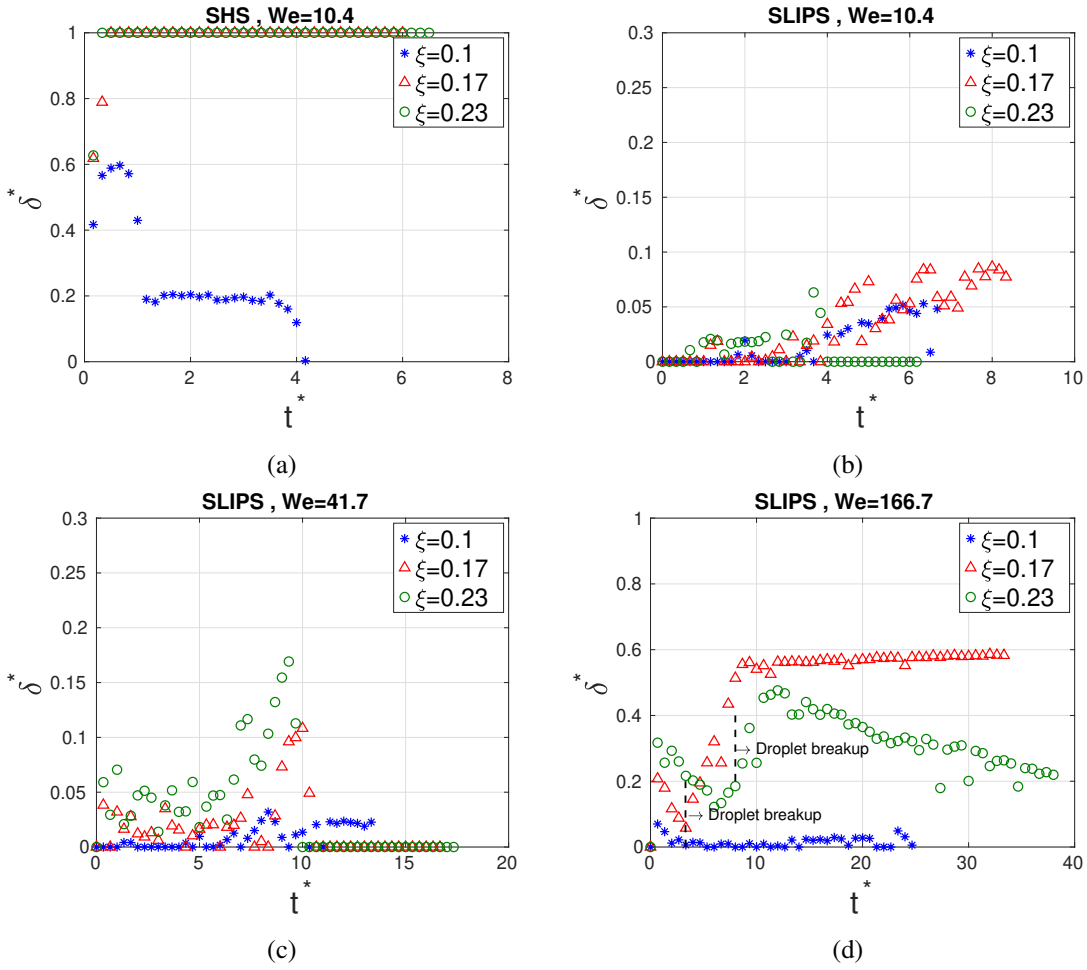

Figure 3.13: Comparison of δ^* during droplet impact for different surface patterns ($\xi = 0.1$, 0.17 and 0.23) on (a) SHS, $We = 10.4$ (b) SLIPS, $We = 10.4$ (c) SLIPS, $We = 41.7$ and (d) SLIPS, $We = 166.7$

Average normal velocity

Another parameter that can provide further information on droplet hydrodynamics in both superhydrophobic and slippery impregnated surfaces is the U^*. It is defined as $U^* = \overline{U}_z/U_0$ where $\overline{U}_z$ and U_0 are the average normal velocity of the droplet (positive in the upward direction) and initial impact velocity, respectively. This parameter explains droplet average upward velocity during the receding stage and jumping velocity of the droplet. Figure3.14 demonstrates the effect of surface morphology (ξ) on U^* in SHS and SLIPS. Figure3.14(a) shows that there is a significant difference in U^* amongst surface topology of the superhydrophobic surface. During the receding stage of droplet (after $t^* = 2$), the kinetic energy of droplet is higher in $\xi = 0.1$ compared to $\xi = 0.17$ and $\xi = 0.23$ which resulted in droplet bouncing in SHS. For SLIPS cases at the same condition as shown in Figure3.14(b), U^* is similar for all surface patterns while in

the receding stage of $\xi = 0.23$, kinetic energy is less reduced that lead to droplet bouncing. At $We = 41.7$ of SLIPS (Figure3.14(c)), both surfaces of $\xi = 0.17$ and $\xi = 0.23$ have approximately similar behavior and exhibit bouncing behavior despite the high–density micro–textured surface ($\xi = 0.1$).

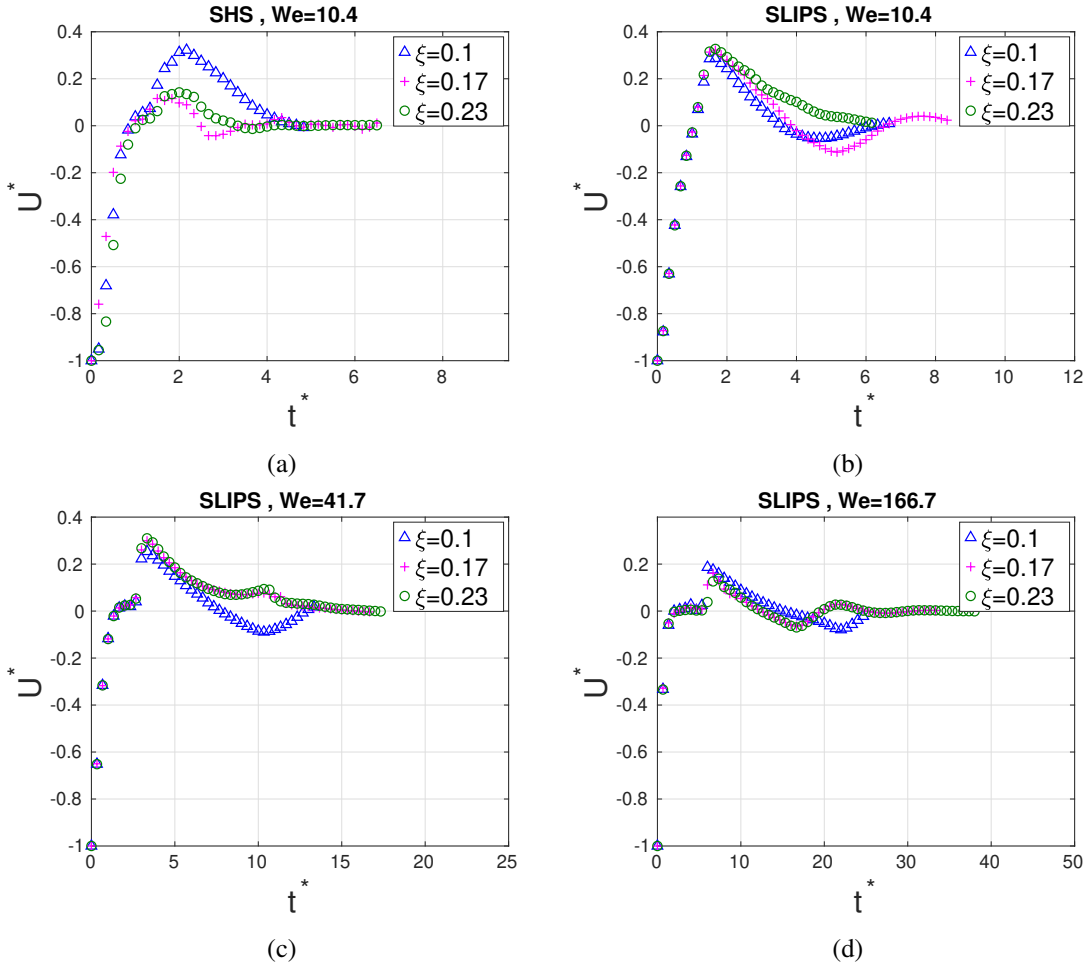

Figure 3.14: Comparison of U^* during droplet impact for different surface patterns ($\xi = 0.1$, 0.17 and 0.23) on (a) SHS, $We = 10.4$ (b) SLIPS, $We = 10.4$ (c) SLIPS, $We = 41.7$ and (d) SLIPS, $We = 166.7$

For higher Weber number ($We = 166.7$) in SLIPS as can be seen in Figure3.14(d), U^* behaves approximately similar in both $\xi = 0.17$ and $\xi = 0.23$. The quantitative data can reveal how the presence of liquid oil is noticeable in droplet hydrodynamics, especially during the receding stage. Analysis of U^* or the coefficient of restitution indicates how the energy is dissipated during the impingement process especially in micro–droplets less than $\sim 100\ \mu m$ for which the energy loss is more significant [65]. In Figure 3.14a, the maximum U^* in both the $\xi = 0.17$ and $\xi = 0.23$ decreased as the droplet lost most of the energy. However, in all SLIPS cases, the maximum of U^* is approximately the same for different surface structure. Most

dissipation occurred in the receding stage in SLIPS. The slope of U^* in Figure 3.14b and c indicates that the energy loss is smaller for the surfaces with low density textured surfaces.

To better describe the effect of surface morphology and impact velocity on the outcome of droplet impact, a table based on critical parameters of ξ and We is presented (Figure 3.15). Three states of Complete–Bouncing, Partial–Bouncing and No–Bouncing are considered to illustrate the outcome of droplet impact in SHS and SLIPS. As also described earlier, the probability of droplet pinning within the micro–pillars is significantly low in SLIPS which makes this surface a promising method for having a mobile and non-wetting surface.

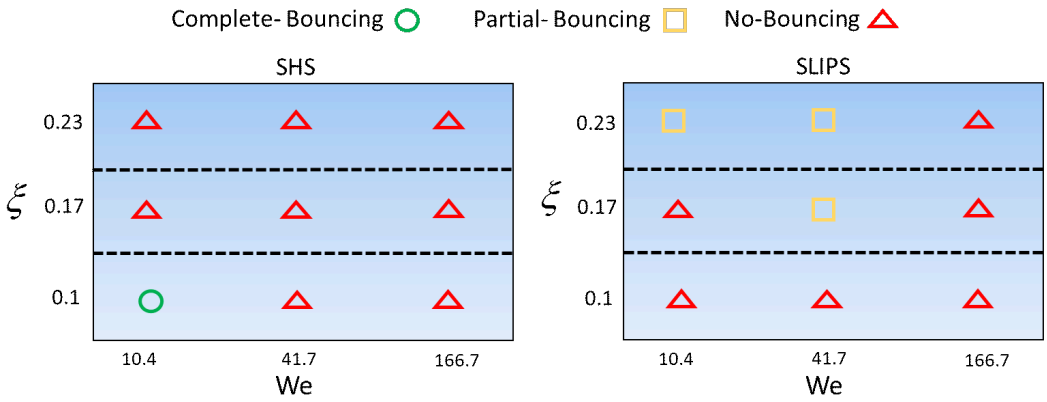

Figure 3.15: A map of micro–droplet impact outcome based on We and ξ on SHS and SLIPS

3.6 Conclusion

In this study, we numerically studied the performance of both superhydrophobic and slippery impregnated liquid surfaces during micro–droplet impact on surfaces with square micro–pillar arrays. In this regard, an in–house multiphase solver in conjunction with the Kistler dynamic contact angle method was employed. For this purpose, a 3D micro-structured surface was infused with a lubricant (Dupont Krytox GPL101) to make slippery surfaces. Three different Weber numbers and surface patterns were studied to understand the dynamics of droplet impact. It was found that the structure of surfaces can significantly change the dynamics of droplet impact since both the droplet and surface pillars were on micro–scale. The results demonstrated that SHSs exhibit anti-wetting behavior only at specific surface properties and droplet impact conditions. However, our findings from SLIPS cases revealed that they were capable of enhancing droplet mobility and anti-wetting properties especially in conditions where SHS failed in droplet repellency. It was observed that slippery surfaces with a high-density of micro–pillars ($\xi = 0.1$) behaved similarly to the solid surface

while for low-density of micro–pillars ($\xi = 0.23$), dynamics of the droplet was similar to that of a surface with a thin liquid film. The quantitative parameter (δ^*) illustrated that the presence of lubricant within the micro–pillars (especially SLIPS with low–density micro–textured surface) prevents droplet from pinning to the textured surface and leads droplet to bounce in most low and moderate Weber number ($We = 10.4$ and $We = 41.7$).

The effect of surface morphology in SLIPS and SHS on droplet dynamics was demonstrated quantitatively via different dimensionless parameters such as spreading factor, droplet penetration depth within the asperities and average of droplet velocity during impingement (β, δ^* and U^*). It was observed that for micro-droplet impact, SHSs are more sensitive to surface morphologies as droplet completely pinned to all SHS substrate (except for $2w3p$ at $We = 10.4$). However, the probability of droplet pinning in SLIPS is less affected by different surface morphologies. Additionally, in high Weber number cases ($We = 166.7$), the presence of infused oil in slippery impregnated surfaces prevented droplet from pinning to the micro-pillars, although no droplet recoiling occurred on both surfaces. The results of this study demonstrated that the slippery lubricant impregnated surfaces can be employed in various applications such as anti–biofouling to prevent the respiratory micro–droplets on surfaces or in anti–icing applications which are required to avoid droplet pinning to the textured surface.

Chapter 4

Droplet mobility on slippery lubricant impregnated and superhydrophobic surfaces under the effect of air shear flow

[1]

4.1 Abstract

The focus of this study is to investigate and compare the behavior of a droplet on superhydrophobic (SHS) and slippery lubricant impregnated (SLIPS) surfaces under the effect of air shear flow. In this regard, both experimental and numerical analyses have been conducted to compare their performance on droplet mobility under different air speeds. Two different lubricants have been utilized to scrutinize their effect on droplet movement. The numerical simulations have been performed based on the volume of fluid method coupled with the large eddy simulation turbulent model in conjunction with the dynamic contact angle method in addition to a model that can represent the effect of lubricants on slippery surfaces. The numerical simulations are compared with the experimental study in order to shed light on the underlying mechanisms. The results showed that under the same conditions, the critical velocity for droplet movement on the superhydrophobic surfaces is lower than that on the slippery lubricant impregnated surfaces due to

[1] "Reproduced (or 'Reproduced in part') with permission from (Yeganehdoust F., Amer A., Sharifi N., Karimfazli I., Dolatabadi A., Droplet Mobility on Slippery Lubricant Impregnated and Superhydrophobic Surfaces under the Effect of Air Shear Flow, Langmuir, https://doi.org/10.1021/acs.langmuir.1c00726) Copyright 2021 American Chemical Society."

the smaller droplet base diameter and the larger contact angle. The hydrodynamics of droplet mobility on superhydrophobic surfaces exhibits a rolling behavior while for the slippery lubricant impregnated surfaces a combination of rolling and sliding is observed. Beyond the critical airflow speed, a complete droplet shedding on all surfaces occurs. The wetting length and position of the droplet on superhydrophobic and slippery surfaces have been measured. On slippery surfaces, the speed of droplets is greatly affected by the lubricant properties while similar behavior in the wetting lengths is observed.

Droplet shedding, Slippery lubricant impregnated surfaces, Superhydrophobic surfaces

4.2 Introduction

Droplet mobility plays an important role in a wide range of engineering applications such as in self-cleaning surfaces [159–161], microfluidics [11, 162], drug delivery, water harvesting, spray coatings, and anti-icing coating technologies. Mobility of sessile droplets occurs when there is an imbalance in droplet contact line forces. This might attribute to the conditions where there is thermal gradient [163], air shear flow [88, 91], mechanical vibration [164] and electro–wetting [165]. Amongst mobility-driven forces, the air shear flow scenario has attracted significant attention in various natural and industrial applications. Droplet incipient movement occurs when the drag force (due to air shear flow) overcomes the adhesion force between the droplet and substrate. The drag force and adhesion force are illustrated as $F_{drag} \propto \frac{1}{2}\rho_l V_{air}^2 S C_D$ and $F_{adh} \propto L_w \sigma \left(\cos\theta_{\min} - \cos\theta_{\max}\right)$ [88, 91] where ρ_l, V_{air}, S and C_D are droplet density, airspeed, the front area of the droplet facing the air flow, and the drag coefficient, respectively. L_w and σ are droplet wetting length and surface tension coefficient. $\theta_{\min}$ and $\theta_{\max}$ denotes the upstream and downstream contact angles once the droplet starts its movement on the surface due to the air shear flow.

Amongst different parameters (such as droplet properties and air speed) that affect droplet shedding, the surface property is a critical one. In conventional methods, low energy surfaces with micro/nano–structured surfaces such as superhydrophobic surfaces (SHS) have been used to enhance droplet repellency due to the air pockets in the textured surface. It has been proved that surfaces with low adhesion and contact angle hysteresis can promote droplet mobility. Superhydrophobic and slippery lubricant impregnated surfaces (SLIPS) are amongst these surfaces that induce droplet mobility. [87, 88, 93–96].

Several studies have reported the major influence of surface wetting properties on droplet shedding by the airflow. Milne and Amirfazli [88] investigated the critical air velocity for the shedding of a droplet

on surfaces with different wettabilities. It has been shown that superhydrophobic surfaces have the lowest critical air velocities in all cases. Additionally, in situations where multiple droplets were present, a unique critical velocity was required, which indicates that the shedding behavior can be assumed to be similar in the presence of multiple droplets. Moghtadernejad et al. [87] performed an experimental and numerical investigation on the effect of air flow on the shedding and coalescing of two droplets on a superhydrophobic. It was reported that the coalescence phenomenon could facilitate droplet detachment from the superhydrophobic surface especially at low air speeds. For the low air speed of 5 m/s, the coalescence of droplets resulted in successive rebounds of the merged droplet on the substrate. In another study by Moghtadernejad et al. [91], they also evaluated the effect of air shear flow on different liquid properties depositing on a laser micro–machined surface with superhydrophobic properties substrates. They observed that droplet dynamics are affected by both surface tension and viscosity properties. It was demonstrated that in liquids such as ethylene glycol and propylene glycol with low surface tension and high viscosity, droplet detachment did not occur. This was attributed to the droplet penetration within the surface asperities due to low surface tension and high viscosity of liquids that lead to droplet pinning.

Further studies have been analyzed how the onset of droplet shedding was affected by the presence of the neighboring droplets [89, 90]. They investigated the effect of the arrangement of multiple sessile droplets by airflow. Four arrangements including the triangle, square, reversed triangle and diamond have been analyzed. It was found that both the spacing between the droplet and their arrangements required different critical airflow for droplet shedding. Despite several experimental and numerical studies on droplet mobility on superhydrophobic substrates which exhibit their remarkable shedding behaviors, the robustness of their functions depends on the stability of air pockets. Several reasons such as humidity and the collapse of the trapped air through external wetting pressures can easily lead to liquid pinning and may induce ice nucleation [23, 26, 27]. A recent approach suggests a combination of micro-structured surfaces and slippery lubricants known as slippery lubricant impregnated surfaces (SLIPS) [19, 29, 166]. These surfaces result in reducing contact angle hysteresis and have a significant influence on droplet mobility. Additionally, they can repel various types of liquids with different surface tensions and are considered omniphobic.

Only a few studies have considered the effect of slippery surfaces on droplet mobility [30] and their performance. Smith et al. [30] investigated the fundamental hydrodynamics of droplet mobility on tilted slippery surfaces. Different parameters such as droplet and lubricant properties, texture size, and substrate

tilt angle were involved in their model. The model also included the effect of energy loss of viscous dissipation due to the presence of wetting ridge from the lubricant. They indicated that the proper performance of slippery surfaces depends on the design of surfaces. Orme et al. [95] have introduced the effect of step in a few microns to control droplet retention and shedding on slippery surfaces. Their results showed that a simple structure could provide a capillary force due to the interaction between the lubricant menisci created by the step and droplet which resulted in droplet repelling or attracting from the step based on the Cheerios effect. Pham et al. [150] impregnated lubricant within a porous surface to achieve a more durable slippery surface and maintaining the lubricant over a longer period. They found that ultra-small droplets varied substantially by changing the level of lubricant thickness. By reducing the level of lubricant thickness (exposing the underlying solid surface), the microliter droplet started pinning into the surface while in nano-liter droplets, no significant pinning has been observed.

The performances of SLIPS for droplet mobility under the effect of air shear flow compared to superhydrophobic surfaces are still a question and have not yet been investigated. In this study, a thorough experimental study was conducted to compare the function of SHS and SLIPS under the effect of air shear flow. Two different slippery surfaces have been used to evaluate the effect of lubricant properties on the hydrodynamics of droplet shedding at various air speeds. A multiphase numerical simulation is also performed to enhance our understanding and observations in the experimental study.

4.3 Experimental method

4.3.1 Samples preparation

Generating micro/nano–textured surfaces is a critical factor for creating both superhydrophobic and slippery surfaces. In all of the current experimental work, the hierarchical textured surfaces are prepared using the suspension plasma spray method (SPS) [153]. In this technique, small ranges of particles (from nm to μm) are deposited on the surface [152, 167]. The material of all samples was flat stainless steel with a dimension of $5\ cm\ \times\ 5\ cm\ \times\ 0.3\ cm$. A grit blasting process was first performed using fine alumina particles to produce a surface roughness between $1.5 - 2\ \mu m$ which resulted in a hierarchical texture surface combined with the SPS coating process. After grit blasting, the coating was deposited using the SPS. In this study, TiO_2 is used as the coating material and the main advantages of using TiO_2 is its thermal/chemical stability, non–toxicity, and low cost. Additionally, another characteristic of TiO_2 coating is its mechanical

durability and functional properties compared to polymer-based coatings [152].

The suspension in TiO_2 coating is prepared such that the $1000\ g$ of suspension contains $720\ g$ of Ethanol, $180\ g$ of Ethylene glycol, $95\ g$ (95 wt $\%$ of the solid content of TiO_2) and $5\ g$ (5 wt $\%$ of the solid content) of polyvinylpyrrolidone (PVP). The PVP acts as a dispersant which is gradually added to the Ethanol to prevent particle agglomeration and improve the stability of the suspension during the spraying process. Ethylene glycol can also increase the stability of the suspension by increasing its viscosity. The mixing process was done using a magnetic stirrer and sonication (ultra-sound probe). Then, titania suspension was prepared by slowly adding TiO_2 powder to prevent agglomeration. The suspension was then added to the injection system which consists of two sealed pressurized tanks, suspension, and water. Finally, the suspension is injected into the plasma plume and deposited onto the substrates.

A critical parameter in developing samples with this technique is the number of passes, i.e. the number of times the plasma gun scans the substrate which results in various heights of micro–pillars. In the current study, two batches of coatings with 30 and 50 passes were produced and it was concluded to consider the 50 passes of spray coating as it could provide higher micro–pillars height ($\sim\ 250\ \mu m$). This would be also more functional in SLIPS as there would be more reservoirs for oil impregnation [168]. The morphology of micro–structured surface after spray coating with titania suspension for 50 passes conditions is illustrated by the SEM images in Figure 4.1. It can be seen that the surface morphology resembles micro-pillar pattern (from fine to cauliflower-like micro–structure). All samples were cleaned in two steps. First, the samples were cleaned by placing them in distilled water using sonication (ultra-sound probe) for $5 - 10$ minutes. Then, samples were placed in boiling distilled water for about 20 minutes and rinsed with isopropyl alcohol. To achieve SHSs, substrates were coated with a thin stearic acid layer by dipping within the solution and then leaving the samples to dry out. The stearic acid solution comprised $99\ g$ of propanol and $1\ g$ of stearic acid powder. The thin layer of stearic acid layer transformed the hydrophilic coating into a superhydrophobic surface due to its low surface energy combined with the micro/nano-textured surface [152, 153].

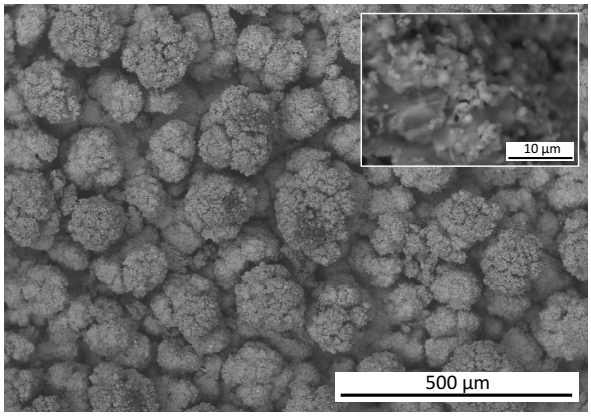

Figure 4.1: SEM images of spray coatings produced by SPS technique for 50 passes

4.3.2 Slippery lubricant impregnated surfaces preparation

To obtain slippery impregnated surfaces, the based surfaces should have low surface energy (oleophilic or hydrophobic surface) combined with the surface roughness. In the current study, the coated samples have micro/nano-textured which is coated with a hydrophobic layer of stearic acid resulting in a low surface energy coating. Additionally, the hierarchical textured surface provides a well–reservoir for developing slippery oil-impregnated surfaces. To create slippery impregnated surfaces, the oil was impregnated through the hydrophobic micro–textured surface. The oil impregnation was performed by placing samples in the vacuum chamber and adding oil and then vacuuming for approximately 10 minutes. This resulted in a homogeneous oil–infused slippery surface by removing any air bubbles from the oil and coating interface.

Two lubricants (Krytox GPL101 and Krytox 143AB) with different viscosities have been chosen to better evaluate the effect of lubricant properties on SLIPS performance for the mobility of droplet under the effect of air shear flow. Table 4.1 illustrates the physical properties of the liquids.

Table 4.1: Physical properties of fluids

Fluids	**Density**(Kg/m^3)	**Kinematic viscosity**(cSt)	**Surface tension**(N/m)
KrytoxGPL 101	1850	17.7	0.017
Krytox143 AB	1890	240	0.017
Water	1000	1	0.072

The confocal laser scanning microscopy of superhydrophobic samples before and after impregnation with low (Krytox GPL101) and high (Krytox 143AB) viscous oils are illustrated in Figure 4.2. It can be seen that the oils are wicked within the textured surface. Confocal microscopy is also able to provide information

on the height of micro-structures and lubricants. To achieve a similar level height of lubricant in all SLIPS samples, once the lubricants are infused within the substrates, both surfaces with low and high viscous oils were tilted for about 10 minutes and 2 hours, respectively. This lead to a similar level height of lubricant in SLIPS to better evaluate and compare the two slippery surfaces. Confocal microscopy was used to provide information on surface roughness parameters. Accordingly, the S_z is defined as the average of the largest peak to valley of asperities measured at different spots on each surface. For the superhydrophobic surface, S_z is approximately $260\ \mu m$. The S_z measurements for both slippery surfaces are around $210\ \mu m$ which indicates an approximate lubricant thickness of $50\ \mu m$ in both slippery surfaces. The lubricant cloaking phenomenon on the sessile droplets is also examined using the spreading coefficient of the oil on the droplet through $S_{\mathrm{ow}} = \sigma_{\mathrm{wa}} - \sigma_{\mathrm{oa}} - \sigma_{\mathrm{ow}}$ (where σ_{wa}, σ_{oa} and σ_{ow} are the surface tension coefficient of water-air, oil-air and water-oil, respectively). If $S_{\mathrm{ow}} > 0$, the lubricant will cloak the droplet. Otherwise ($S_{\mathrm{ow}} < 0$), the lubricant will fail to cloak the droplet. Using the surface tension of DI water ($\sigma_{\mathrm{wa}} = 72.4 \pm 0.1\ mN/m$), both low and high viscous oils ($\sigma_{\mathrm{oa}} = 17 \pm 1\ mN/m$), and the interfacial tension between the two liquids ($\sigma_{\mathrm{ow}} = 54\ mN/m$), the spreading coefficient is determined as $S_{\mathrm{ow}} = 1\ mN/m$.

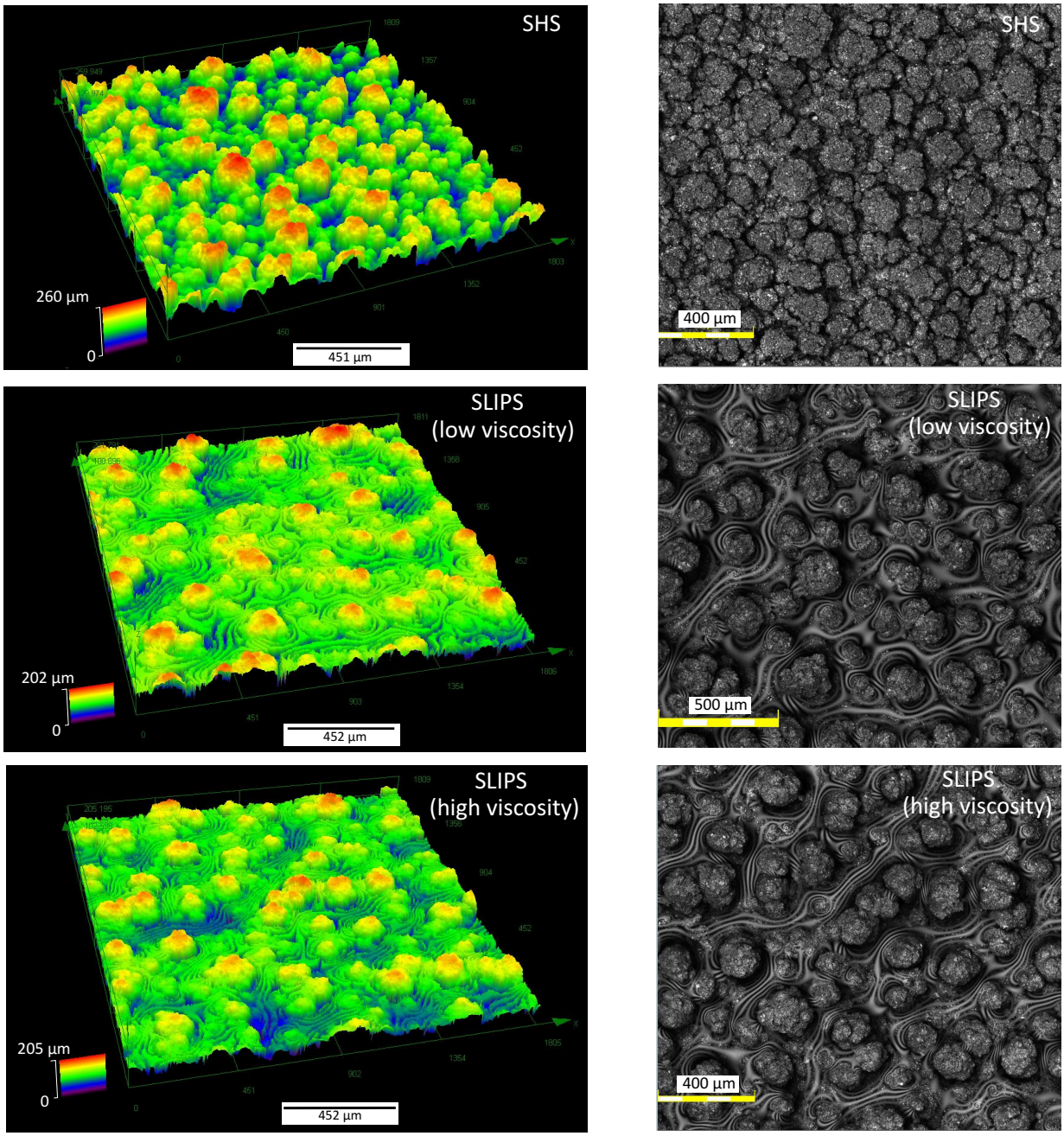

Figure 4.2: Confocal laser scanning microscopy of SHS, SLIPS–low viscosity and SLIPS–high viscosity

This suggests that the droplets are presumed to be encapsulated by the lubricant. However, the extensiveness of the cloaking significantly varies depending on both the lubricant layer thickness and droplet size. The cloaking for both impregnated surfaces did not significantly affect the droplet dynamics during the shedding experiments. The sufficient lubricant cloaking can even improve droplet sliding, especially for smaller droplets [150].

4.3.3 Experimental set–up

Figure 4.3 shows the schematic of the experimental set-up to characterize the droplet mobility under the effect of air shear flow. A high-speed camera (Photron, CA, USA) with an Ultra-Zoom lens was used to capture the in details at the rate of $5000\ fps$. A light-emitting diode (LED) along with a diffuser was used for the illumination. All experimental studies were performed at room temperature ($23^{\circ} \pm 1^{\circ}$). The airflow in the experimental set–up is supplied by the air supply passing through a pipe with the inlet diameter of approximately $10\ mm$ and length of $100\ cm$ which resulted in a fully–developed flow. The pipe is close to the substrate while the sessile droplet is located approximately $10\ mm$ away from the air shear flow on the substrate. This would counteract the effect of developing the boundary layer on droplet dynamics and ensure uniform air flow. A $15 \pm 2\ \mu$L single water droplet (or the initial diameter of $D_0 \sim 3\ mm$) was deposited on a substrate from a droplet dispenser. The physical properties of fluids are illustrated in Table 4.1. Using a pressure regulator calibrated with a pitot tube, different air speeds in the range of 5 to $20\ m/s$ were achieved. To capture the effect of airflow on droplet mobility more accurately, a solenoid valve was connected to a switch between the airflow and a high-speed camera. This give us precise results as the camera can detect the effect of airflow once the valve is open.

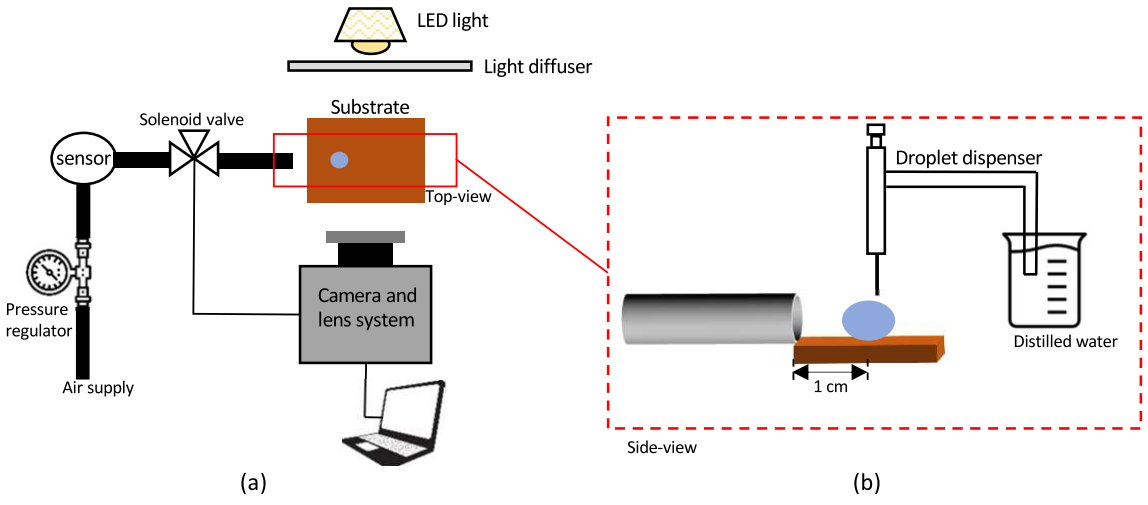

Figure 4.3: (a) A schematic of the experimental set–up and (top–view) (b) the droplet for shedding under the effect of air flow (side–view)

4.3.4 Contact angle measurements

The advancing (θ_A) and receding (θ_R) contact angles of superhydrophobic and the two slippery samples were evaluated by expanding and retracting of a droplet using a dispenser which results in θ_A and θ_R, respectively. A droplet with a 30 μl droplet was deposited on the surface, then by expanding and contracting of 50 μl droplet, θ_A and θ_R were measured. Using the needle method, several measurements were taken to achieve the average value for all the contact angles. Figure 4.4 demonstrates the average of the advancing and receding contact angles as well as the contact angle hysteresis for the three samples. Because of the wetting ridge formation near the droplet in SLIPSs, a method by Guan et al. [34] is used for contact angles measurement by fitting a circle to the droplet where it fits the surface intersect. It was observed that despite high advancing contact angle in superhydrophobic surface ($153.5° \pm 0.4°$) compared to slippery surfaces ($\theta_A = 113° \pm 1°$), the hysteresis contact angle, which is defined as the difference between advancing and receding contact angles is higher in superhydrophobic surface ($9.0° \pm 0.3°$) compared to SLIPS-low viscosity oil ($3° \pm 1°$) or SLIPS-high viscosity oil ($3.5° \pm 0.5°$). It should be noted that for the shedding experiments, the drag force by the air shear flow deforms the droplet to $\theta_{\min}$ and $\theta_{\max}$ (as also seen in Figure 4.12) which are denoted as the upstream and downstream contact angle once the droplet starts its movement on the surface. It has been observed that the $\theta_{\min}$ and $\theta_{\max}$ of the droplet are increased during the shedding phenomenon, especially for the SLIPS which is discussed in the results section.

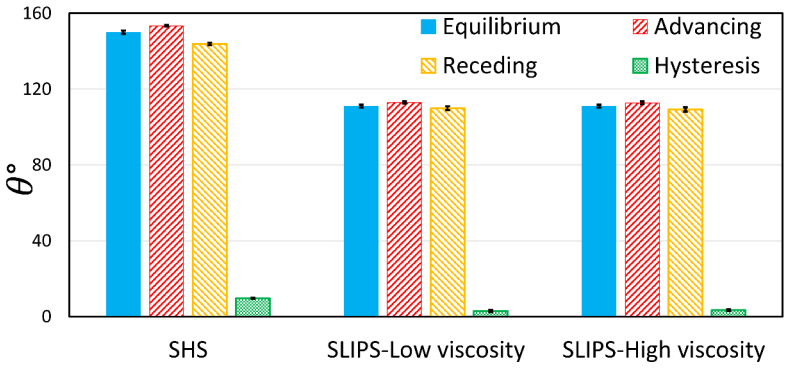

Figure 4.4: Contact angle measurements in SHS, SLIPS-low viscosity and SLIPS-high viscosity

4.4 Numerical method

The air flow exiting the pipe is in the turbulent regime and has a fairly uniform shape. Assuming a uniform inlet air velocity for the external flow on the flat plates [87], the air flow velocities are between 5 and $20\ m/s$, which result in the Reynolds number in the range of $10^3 < \mathrm{Re_D} < 3 \times 10^5$. In order to model the shedding of the droplet, Large Eddy Simulation (LES) is used since a broad turbulent wake region and a continuous vortex shedding occur downstream. In LES, the large-scale motions with filtered Navier-Stokes equation are resolved while the small scales are modeled with the sub-grid stress method. The sub-grid scale (SGS) model represents the effects of small turbulence scales on the flow. The velocity field is separated into a grid and sub-grid part. The grid-scale of the field represents the large eddies, while the sub-grid part of the velocity represents the small scales. The grid scale component is obtained by $\bar{f}(\mathbf{x}) = \int_D f(\mathbf{x}') G(\mathbf{x}, \mathbf{x}')\, d\mathbf{x}'$ where D denotes the computational domain and G is the grid filter function. The governing equations by applying the filter operation are,

$$\frac{\partial \bar{u}_i}{\partial x_i} = 0 \tag{4.1}$$

$$\frac{\partial \bar{u}_i}{\partial t} + \frac{\partial}{\partial x_j}\left(\bar{u}_i \bar{u}_j\right) = -\frac{1}{\rho}\frac{\partial \bar{p}}{\partial x_i} + \frac{\partial}{\partial x_j}\left(\nu \frac{\partial \bar{u}_i}{\partial x_j}\right) - \frac{\partial \tau_{ij}}{\partial x_j}, \tag{4.2}$$

where τ_{ij} is the residual stress tensor (the unresolved scales of the filtered velocity field), $\overline{u_i u_j} - \bar{u}_i \bar{u}_j$. Subgrid-scale turbulence models usually employ the Boussinesq hypothesis and seek to calculate the deviatoric part of the SGS stress tensor using $\tau_{ij} - \frac{\delta_{ij}}{3}\tau_{kk} = -2 v_{sgs} \bar{S}_{ij}$, where $\bar{S}_{ij}$ is the resolved rate-of-strain tensor which is defined by,

$$\bar{S}_{ij} = \frac{1}{2}\left(\frac{\partial \bar{u}_i}{\partial x_j} + \frac{\partial \bar{u}_j}{\partial x_i}\right). \tag{4.3}$$

The SGS models used in this study are the Smagorinsky [169, 170] and v_{sgs} is the subgrid-scale turbulent viscosity which is computed as, $v_{sgs} = (C_s \Delta)^2 |\bar{S}|$ where $|\bar{S}| = \sqrt{2 \bar{S}_{ij} \bar{S}_{ij}}$, Δ is the grid size and C_s is the Smagorinsky constant. Substituting into the Equation 4.2 results the following,

$$\frac{\partial \bar{u}_i}{\partial t} + \frac{\partial}{\partial x_i}\left(\bar{u}_i \bar{u}_j\right) = -\frac{1}{\rho}\frac{\partial \bar{p}}{\partial x_i} + \frac{\partial}{\partial x_j}\left(\left[2v + 2v_{sgs}\right] \bar{S}_{ij}\right). \tag{4.4}$$

To account for the effect of surface tension force, the force F_s is included in the right side of the momentum equation which is defined as $F_s = \sigma\kappa\hat{n}\delta$ based on the continuum surface force (CSF) [127]. Here, σ is the surface tension coefficient, κ is the interface curvature defined as $-\nabla \cdot \hat{n}$ (where $\hat{n}$ is a unit surface vector). A multi–phase flow solver based on the Volume of Fluid (VOF) method in OpenFOAM [45, 83, 128] was used in conjunction with a modified contact angle model [166].

Regarding the VOF method for tracking each phase interface, a volume fraction α_i is introduced in which the value of $i = 1, 2$ that represents air and water, respectively. The value of α_i is in the range between 0 and 1 and the physical properties of phases are defined based on the volume fraction average of all fluids in the cell. Thus, density and viscosity would be $\rho = \sum_{i=1}^{2} \alpha_i \rho_i$ and $\mu = \sum_{i=1}^{2} \alpha_i \mu_i$. The volume fraction is advected by the transport equation and the evolution of the interface was computed as follows,

$$\frac{\partial \rho \alpha_i}{\partial t} + \nabla \cdot \left(\overrightarrow{U} \alpha_i \right) + \nabla \cdot \left(\overrightarrow{U}_r \alpha_i \left(1 - \alpha_i\right) \right) = 0, \tag{4.5}$$

where U_r is an artificial compression velocity at the free surface that acts normal to the interface to compress the free surface and counteract the numerical diffusion and maintain a sharp interface [156]. U_r is defined in Equation 4.6,

$$\overrightarrow{U}_r = \left(\min\left(C_{\alpha_i} \left|U\right|, \max\left(\left|U\right|\right)\right)\right) \frac{\nabla \alpha_i}{\left|\nabla \alpha_i\right|}, \tag{4.6}$$

where C_{α_i} is the compression coefficient that determines the degree of compression. A dynamic contact angle method (Kistler method) [157] is used in conjunction with the flow model which has been found as one of the accurate methods in modeling dynamic contact angle [158]. In the Kistler method, the dynamic contact angle (θ_D) is described as a function of contact line velocity,

$$\cos\theta_D = 1 - 2\tanh\left(5.16 \left[\frac{\mathrm{Ca} + \mathrm{fHl}}{1 + 1.31(\mathrm{Ca} + \mathrm{fHl})^{0.99}} \right]^{0.706} \right) \tag{4.7}$$

$$\mathrm{fHl}^{0.706} = \frac{1}{5.16} \left[1 + 1.31\mathrm{fHl}^{0.99}\right]^{0.706} \tanh^{-1}\left[\frac{1 - \cos\theta_E}{2} \right]. \tag{4.8}$$

In Equation 4.7, the capillary number is defined as, $Ca = \frac{\mu U_{cl}}{\sigma}$ where U_{cl}, μ and σ are the spreading velocity of the contact line, the dynamic viscosity and the surface tension of the liquid. fHl is the empirical Hoffman's function. The equilibrium angle (θ_E) is then replaced by either an advancing or receding contact

(θ_A or θ_R) respectively, depending on the sign of the velocity vector at the contact line.

Although non–uniform micro–structured coated surfaces have been used for all experimental studies, the numerical model has been simplified to a flat smooth surface. The micro-pillar surfaces can add extra computational cost to the LES model and contact angle method. Regarding the numerical model of droplet shedding, a droplet is located in the computational domain of the size $8 \times 24 \times 8\ mm^3$ where the droplet is $10\ mm$ away from the air flow as shown in Figure 4.5. Since the LES model has been used in all simulations, the cells in half of the geometry are refined (as shown in Figure 4.5) in which there are approximately 40 cells within the droplet diameter.

Furthermore, the boundary layer for the laminar flow based on the Blasius solution, is $\delta = \frac{5x}{\sqrt{\mathrm{Re}_x}}$. For the current study where the droplet is placed $10\ mm$ away from the air flow and the air velocities are 5, 10, 15 and $20\ m/s$, the boundary layer thickness is $0.87\ mm$, $0.61\ mm$, $0.50\ mm$ and $0.43\ mm$. Thus, comparing the size of the droplet to boundary layer thickness, a uniform flow on the droplet is expected. The grid study has been also evaluated for one of the simulations with the cell sizes of $80\ \mu m$ and $60\ \mu m$ in which both the simulations resulted in similar behavior. To better capture all the shedding phenomena while decreasing the computational time, the cell size is considered as $80\ \mu m$ in the refined region.

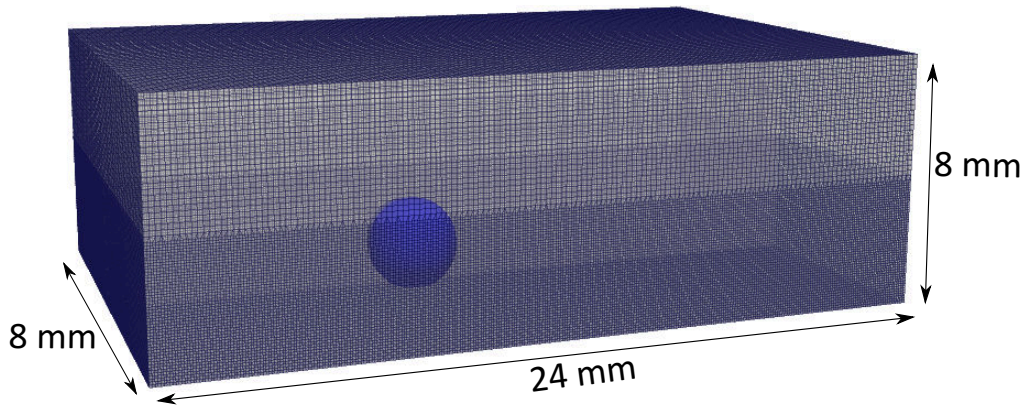

Figure 4.5: Computational domain for droplet shedding

As described above, in the experimental study of slippery surfaces, a thin layer of lubricant ($\simeq 50\ \mu m$) exists at the surface. To consider the effect of this layer, a partial–slip boundary condition is implemented on the surface. The partial–slip condition has been derived based on the balance of the shear stress of oil and water/air fluids ($\tau_{oil} = \tau_{\text{fluid}}$) as shown in Figure 4.6. The balance of shear stress is substituted as $\mu_{oil}({}^{U_{\text{int}}}/_{\delta_{oil}}) = \mu_{fluid}({}^{\partial u}/_{\partial n})$, where U_{int} is the interface velocity and μ_{fluid} can be water or air. Thus, the

velocity of the flat substrate in the numerical simulation is implemented as, $U_{\mathrm{I}} = ({}^{\mu_{fluid}}/_{\mu_{oil}})\delta_{oil}({}^{\partial u}/_{\partial n})$. To evaluate the implemented boundary condition, a Couette flow problem has been considered and compared the numerical results with the theoretical values. Further information is illustrated in the Supporting information.

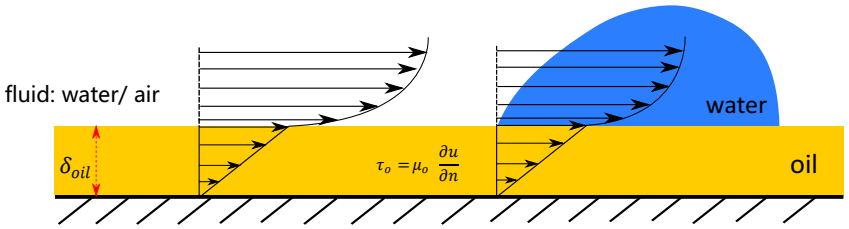

Figure 4.6: A schematic of shear stress balance for droplet shedding

As a $\simeq 15\ \mu l$ of droplet is used in the experimental study, the initial equilibrium radius of droplet in the numerical model (as shown in Figure 4.7) is approximated based on the $\mathrm{R}_{eq} = [\frac{\forall_0}{(4/3)\pi} \times \frac{4}{(1-\cos\theta)^2(2+\cos\theta)}]^{1/3}$, where $\forall_0$ and θ are the droplet initial volume and static contact angle of droplet on the surface [87]. Accordingly, the equilibrium droplet diameter on SHS and SLIPS in the numerical simulation is $3.074\ mm$ and $3.36\ mm$, respectively in which their center is $1.33\ mm$ and $0.602\ mm$ from the surface, respectively.

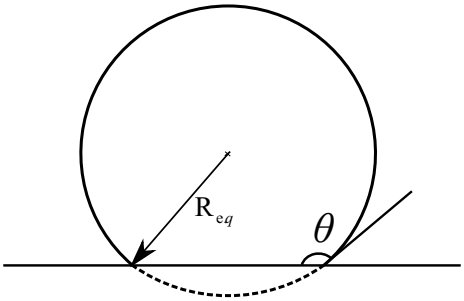

Figure 4.7: A schematic of initial equilibrium droplet (R_{eq}) for numerical simulation

4.5 Results and Discussion

4.5.1 Experimental results: Droplet shedding

As mentioned earlier, superhydrophobic and slippery surfaces are well-known for their anti–wetting and super–slippery features. However, a comparison of their performance under the effect of air shear flow

has not been investigated yet. Here, a thorough experimental study of droplet shedding under the effect of airflow with different air speeds (5, 10, 15, and 20 m/s) have been performed on three different coated surfaces of SHS, SLIPS-low viscous oil (GPL101), and SLIPS-high viscous oil (143AB).

The side–view images of droplet shedding for the airflow of 5 m/s on three different surfaces is shown in Figure 4.8. It should be noted that the critical air velocity for droplet mobility on SHS and SLIPS was obtained as $\sim 3-4\ m/s$ and $\sim 8\ m/s$, respectively. It can be seen that the droplet started rolling on the superhydrophobic surface while the droplet slightly moved on both of the slippery surfaces (as shown in Figure 4.8) and began oscillating on the surface. Additionally, the spherical shape of the droplet is mostly maintained through the shedding process on the superhydrophobic surface.

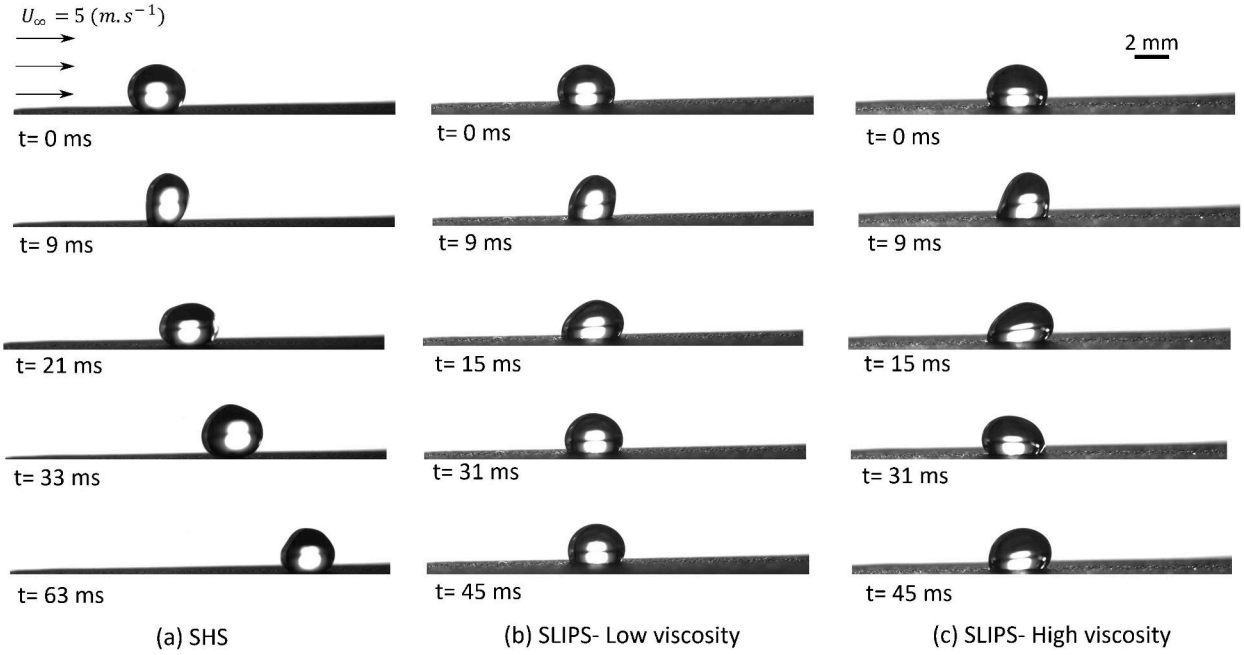

Figure 4.8: Sequences of droplet shedding for the air speed of 5 m/s on (a) SHS, (b) SLIPS-low viscosity lubricant and (c) SLIPS-high viscosity lubricant

For the air shear flow of $U_\infty = 10\ m/s$ (Figure 4.9) on SHS, the droplet initially started rolling on the substrate and detached from the surface, and then it met the superhydrophobic surface once the lift force becomes less than gravity and adhesion forces. As the initial droplet shape is nearly spherical in SHS, the air flow is exposed to a larger surface area and larger drag expected. The drag and lift forces play a dominant effect and resulted in detaching from the surface (Figure 4.9). For both slippery surfaces at $U_\infty = 10\ m/s$ (as shown in Figure 4.9), droplet motion is a combination of rolling and sliding on both slippery surfaces. It can be seen that the droplet slides on both surfaces, however, the time that the droplet reaches the end of the

substrate in high viscosity case is approximately 1.7 times the low viscosity case. This is mostly because of the droplet energy loss due to the viscous dissipation on the slippery surface. Similar to the work by Smith et al. [30], the energy balance for droplet shedding due to the air shear flow would be the balance of viscous dissipation, drag, and adhesion energy (pinning effect of the droplet) as shown in Equation 4.9,

$$V(F_{Drag} - F_{Adhesion}) \sim \ I_{within\ droplet} + \ II_{oil\ film\ beneath\ droplet} + III_{wetting\ ridge}. \tag{4.9}$$

The first, second and third terms on the right hand side of Equation 4.9 are $\mu_{\mathrm{w}} V^2 R_{\mathrm{b}} g(\theta)$, $\frac{\mu_{\mathrm{w}}^2}{\mu_{\mathrm{o}}} V^2 [g(\theta)]^2 t$ and $\mu_{\mathrm{o}} V^2 R_{\mathrm{b}}$ that indicate the viscous dissipation within the droplet (mostly the volume beneath the center of mass), the rate of dissipation within the liquid film, and the energy dissipation within the wetting ridge [30]. R_{b} is the based radius of the droplet (droplet radius on the substrate), $g(\theta)$ is the geometrical relations [30], t is the thickness of the oil, μ_w and μ_o is the water and oil viscosity. Substituting the right hand side terms leads to Equation 4.10. Dividing Equation 4.10 by $R_{\mathrm{b}} \times \mu_{\mathrm{o}}$, results in 4.11, where the two first terms of right hand side can be negligible [30]. Finally, droplet shedding velocity resulted from air shear flow can be expressed as Equation 4.12.

$$V(F_{Drag} - F_{Adhesion}) \sim \mu_{\mathrm{w}} V^2 R_{\mathrm{b}} g(\theta) + \frac{\mu_{\mathrm{w}}^2}{\mu_{\mathrm{o}}} V^2 [g(\theta)]^2 t + \mu_{\mathrm{o}} V^2 R_{\mathrm{b}}, \tag{4.10}$$

$$(\frac{1}{R_{\mathrm{b}} \times \mu_{\mathrm{o}}})(F_{Drag} - F_{Adhesion}) \sim (\frac{\mu_{\mathrm{w}}}{\mu_{\mathrm{o}}} g(\theta) + \frac{\mu_{\mathrm{w}}^2}{\mu_{\mathrm{o}}^2} [g(\theta)]^2 (\frac{t}{R_{\mathrm{b}}}) + 1) V, \tag{4.11}$$

$$V_{Droplet} \sim (\frac{1}{R_{\mathrm{b}} \times \mu_{\mathrm{o}}})(F_{Drag} - F_{Adhesion}). \tag{4.12}$$

Once the drag force overcomes the adhesion force, the droplet starts moving and the droplet velocity is related to the inverse of the base radius of the droplet (R_{b}) and the viscosity of the lubricant layer (μ_{o}). Therefore, as the viscosity of the lubricants is around 17.7 cSt and 240 cST, a lower droplet velocity is expected for the high viscosity case. Additionally, the smaller droplet base on the superhydrophobic surfaces compared with the SLIPSs is another reason for higher droplet speed on superhydrophobic surfaces.

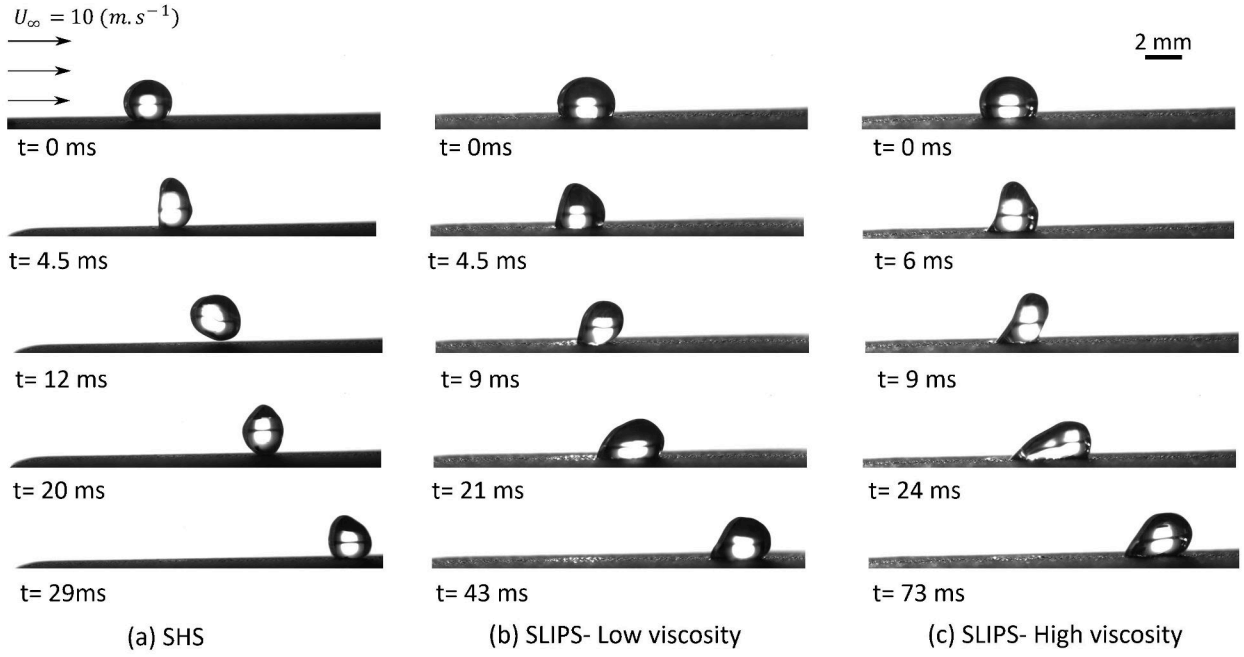

Figure 4.9: Sequences of droplet shedding for the air speed of $10\ m/s$ on (a) SHS, (b) SLIPS-low viscosity lubricant and (c) SLIPS-high viscosity lubricant

Figure 4.10 and 4.11 illustrate the droplet shedding for the air shear flow of $U_\infty = 15$ and $U_\infty = 20\ m/s$, respectively. By increasing the air velocity, the effect of drag force on droplet deformation is more significant. In SHS, as the droplet had an initial small base radius (nearly spherical-shape), it was detached after few milliseconds from the surface. On the other hand, the dynamics of droplet shedding on slippery surfaces were completely different. It can be seen that in higher airflow speeds (Figure 4.10 and 4.11), the droplet elongated on the surface especially on the high-viscous lubricant slippery surface, and finally resulted in droplet breaking. It has been observed that despite droplet break–up, all small droplets completely shed from the slippery surfaces. Moreover, for higher airflow velocities, as the drag force is more significant than the adhesion force, the performance of droplet shedding on both slippery surfaces in terms of the time of droplet shedding, are approximately comparable.

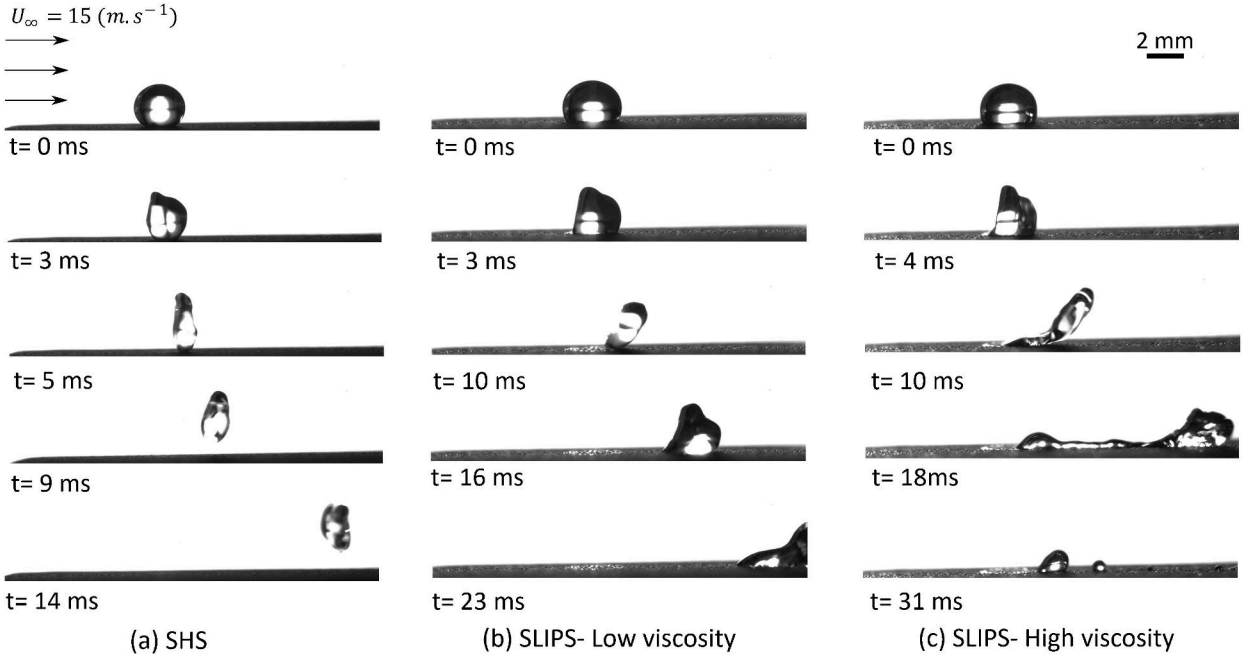

Figure 4.10: Sequences of droplet shedding for the air speed of 15 m/s on (a) SHS, (b) SLIPS-low viscosity lubricant and (c) SLIPS-high viscosity lubricant

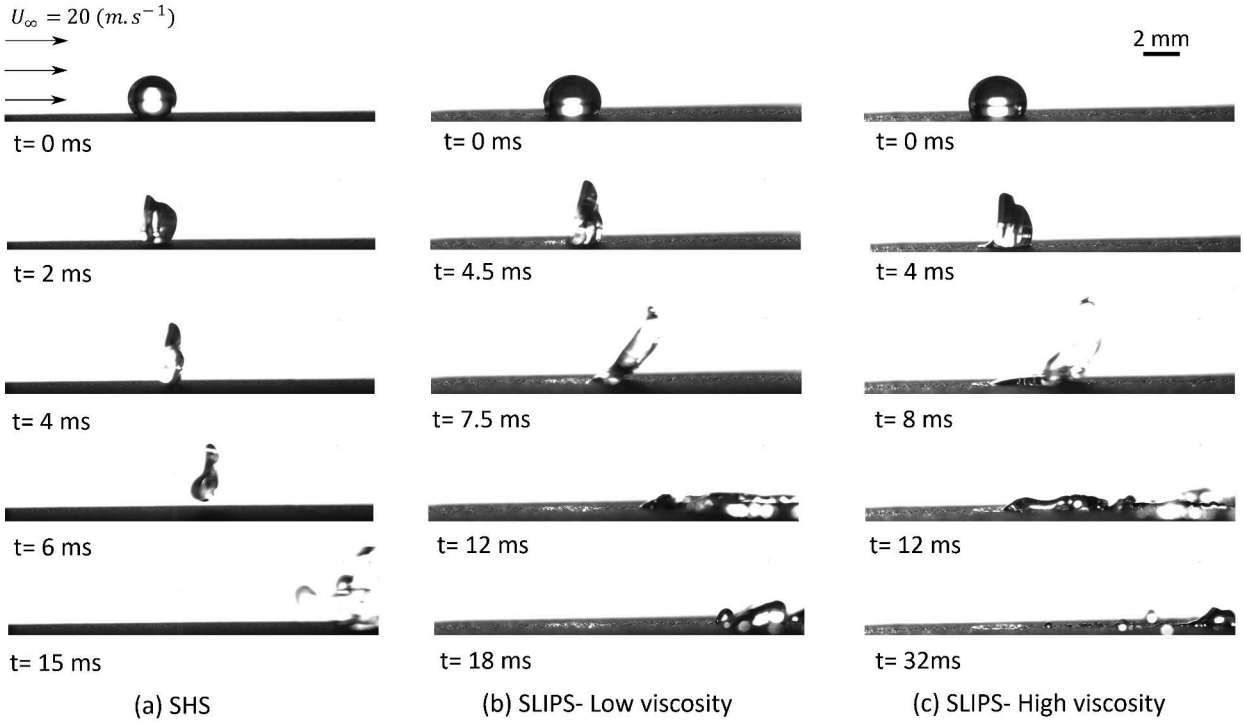

Figure 4.11: Sequences of droplet shedding for the air speed of 20 m/s on (a) SHS, (b) SLIPS-low viscosity lubricant and (c) SLIPS-high viscosity lubricant

The qualitative data exhibit different droplet hydrodynamics on superhydrophobic surfaces compared to

that on slippery surfaces. It should be noted that although ideal superhydrophobic surfaces exhibit excellent performance in terms of droplet shedding velocity, their functions can be deteriorated and become worse than flat surfaces, once the surfaces are damaged and the effect of air trapped within the asperities is collapsed. Additionally, the probability of the droplet pinning in SHS is more significant, especially for smaller droplets [150].

4.5.2 Quantitative characterization of droplet shedding

In this section, two parameters including the wetting length and position of the droplet have been investigated. Surface wettabilities and the performance of surfaces during the droplet shedding process can be described by the evaluation of these parameters. The dimensionless wetting length of the droplet is measured through the shedding process which is defined as $L^* = {}^{L_w}/_{D_{eq}}$, where L_w and D_{eq} are the wetting length of the droplet during the shedding and initial equilibrium diameter, respectively (as shown in Figure 4.12). The position of the droplet (X_{Droplet}) is assumed as the minimum location of the droplet wetting length (Figure 4.12) on the surface which indicates how fast the droplet slides or rolls on the surface. It should be noted that since in some cases the dimensionless wetting length varies due to droplet elongation, considering the mean location of the droplet could be misrepresentative.

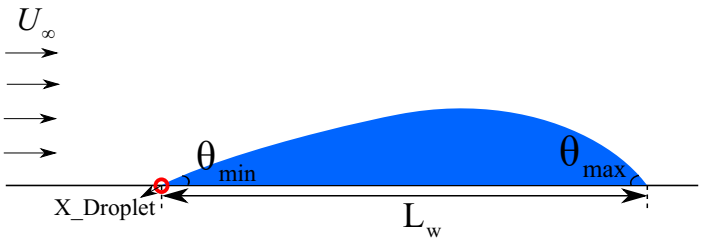

Figure 4.12: A schematic of droplet shedding

Figure 4.13 compares L^* and X_{Droplet} in SHS, SLIPS-low viscosity and SLIPS–high viscosity lubricant for different airflow velocities. At $U_\infty = 5\ m/s$, there are some oscillations in droplet wetting length on SHS however the droplet shape mostly remains spherical on both slippery surfaces and the droplet slightly moves with some oscillations as the drag force is not strong enough compared to the adhesion force. Despite the superhydrophobic surface that exhibited a complete shedding behavior, the slippery surfaces failed to shed the droplet, indeed both slippery surfaces revealed approximately similar behavior. At $U_\infty = 10\ m/s$, droplet deforms at the beginning of shedding on SHS which exhibits a sudden reduction in L^* as shown

in Figure 4.13c. Consequently, the droplet started rolling on the superhydrophobic surface while there are some oscillations due to its detachment from the surface. At higher air flow speeds ($U_\infty = 15$ and $20\ m/s$) droplet is completely detached from the SHS after few milliseconds of movement. On slippery surfaces, as the air flow speed increased, the difference in the performance of the two slippery surfaces in terms of the speed of droplet mobility is more noticeable. Despite complete droplet shedding on both slippery surfaces at $U_\infty = 10\ m/s$ and further cases (Figure4.9), it can be observed that the droplet speed is lower on SLIPS-high viscosity case ($slope_{\text{SLIPS-High viscosity}} < slope_{\text{SLIPS-Low viscosity}} < slope_{\text{SHS}}$).

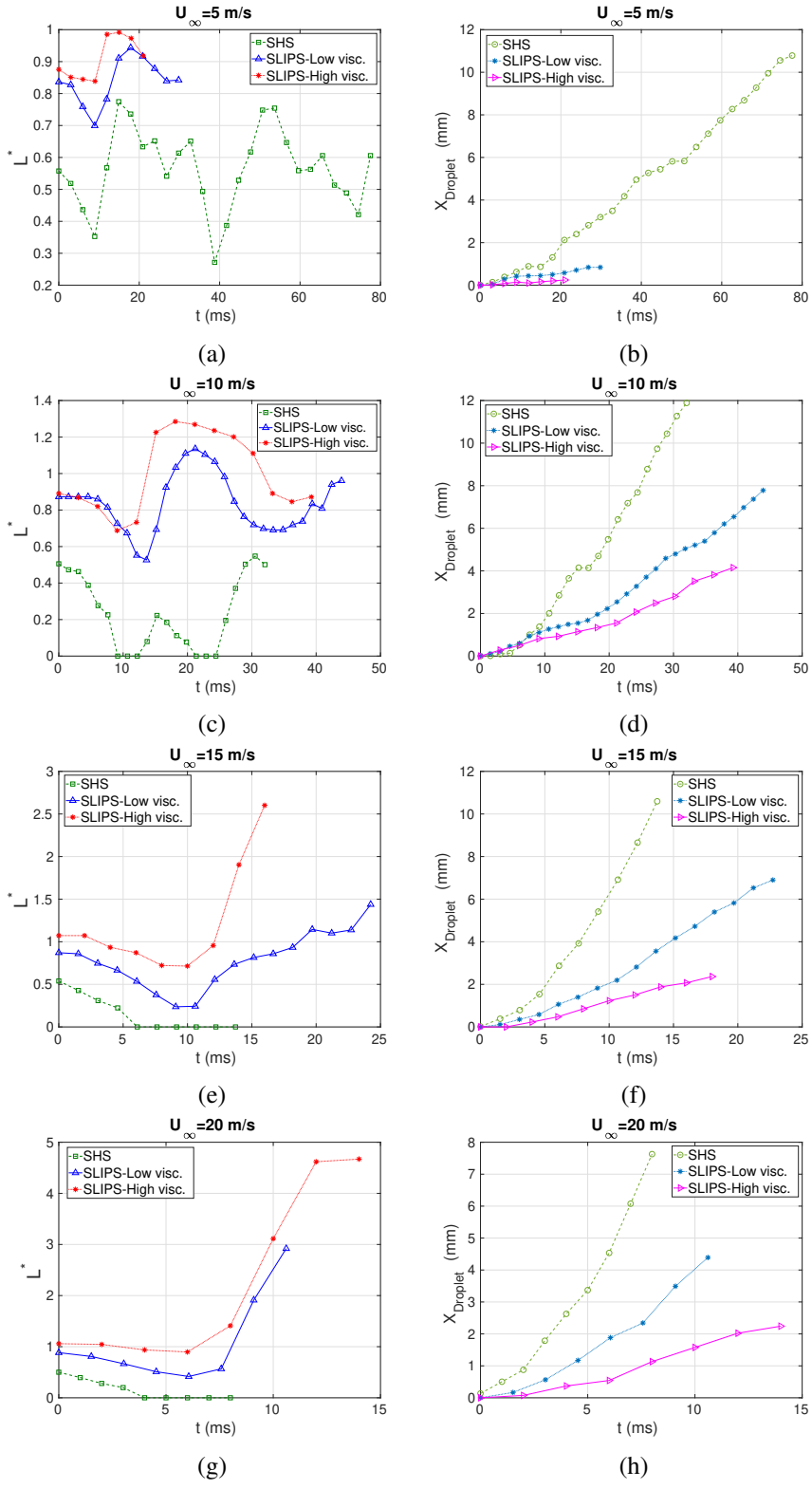

Figure 4.13: Dimensionless wetting length (L^*) and droplet position (X_{Droplet}) in experimental study of droplet shedding for different air flow velocities of 5 m/s (a, b), 10 m/s (c, d), 15 m/s (e, f), 20 m/s (g, h)

As the wetting length is larger on high–viscosity surface (Figure 4.13c) during the shedding process, the adhesion force is higher than the other surfaces which leads to a slower droplet motion. Additionally, the energy loss due to the viscous dissipation as discussed earlier in Equation 4.12 renders the droplet movement. At higher air speeds ($U_\infty = 15$ and 20 (m/s)) the droplet dynamics on slippery surfaces are completely different from that of the superhydrophobic surface. The droplet starts stretching on the slippery surfaces (for instance see Figure 4.11c) which is responsible for the abrupt jump in the wetting length in Figure 4.13e and g. Although the droplet breaks down into smaller droplets, they are still able to slides due to the slipperiness feature of surfaces. Despite similar performances, slippery surfaces with lower viscosity exhibited better performance in terms of having a lower L^* and a larger speed of droplet movement.

4.5.3 Numerical results: Droplet shedding

To further support our observations in the experimental study and better understand the flow interactions during the shedding phenomena, numerical results are illustrated for superhydrophobic and slippery surfaces. The main purpose is to introduce a representation model that can describe the experimental observations and provides results that are comparable to the experimental work. The numerical simulations have been performed for two air velocities of 10 and 15 m/s on three different surfaces based on the problem set-up as discussed in section 3. Figure 4.14 and 4.15 illustrate a comparison of the numerical simulations and experimental observations of droplet shedding on superhydrophobic and slippery surfaces. Along with the velocity distribution, the line integral convolution (LIC) has been shown which is commonly used on two–dimensional vector fields, visualizing the flow motions and better present the air flow behavior and vortex shedding. Droplet dynamics in the numerical simulations present a good agreement with the experimental results. It can be seen that a small wake region is formed in front of the droplet where the flow is reversed. In the downstream, as the inertial force dominates and Re is greater than the critical ones, the separation region forms as the re-circulation and back flow develops and the pressure is dropped. Behind the droplet, the vorticities formed in the wake region, and the periodic generation of vorticities move downstream and vortex shedding occurred. The numerical results also revealed how the contact angle hysteresis can be different in the droplet shedding compared to the quasi-static measurements using a dispenser (section 2.4). As the contact angle hysteresis in the shedding problem is more accurately to define as $\theta_{\max} - \theta_{\min}$ [87, 88], the numerical simulations were modeled based on the contact angles of $\theta_{\max}$ and $\theta_{\min}$. It has been observed that despite the quasi-state measurements which are $\sim 9^\circ$ in SHS and $\sim 3 - 4^\circ$ in SLIPS, the

hysteresis were increased to $13°$, $30°$ and $50°$ for SHS, SLIPS–low and high–viscosity cases, respectively. The considered hysteresis contact angles in the numerical model were $13°$, $30°$, and $50°$ for SHS, SLIPS–low, and high–viscosity cases, respectively, which are based on the $\theta_{\max}$ and $\theta_{\min}$ [87, 88]. The values are based on the average of angles achieved during the incipient motion of the droplet. The L^* and X_{Droplet} have been also quantified with the experimental results as shown in Figure 4.16. Moreover, the effect of lubricant thicknesses on droplet mobility has been compared in the model for two different oil thicknesses ($100\ \mu m$ and $500\ \mu m$) which is demonstrated in the Supporting information.

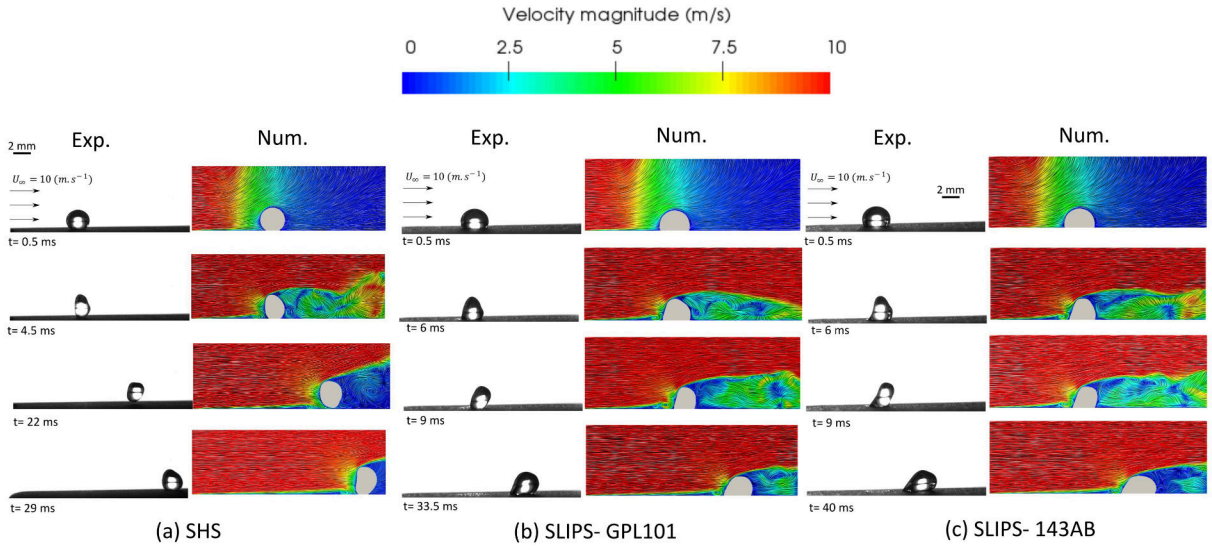

Figure 4.14: Comparison of the numerical simulations (colormaps) and experimental results (greyscale) of droplet shedding at $U_\infty = 10\ m/s$ on (a) SHS, (b) SLIPS-low viscosity and (c) SLIPS-high viscosity

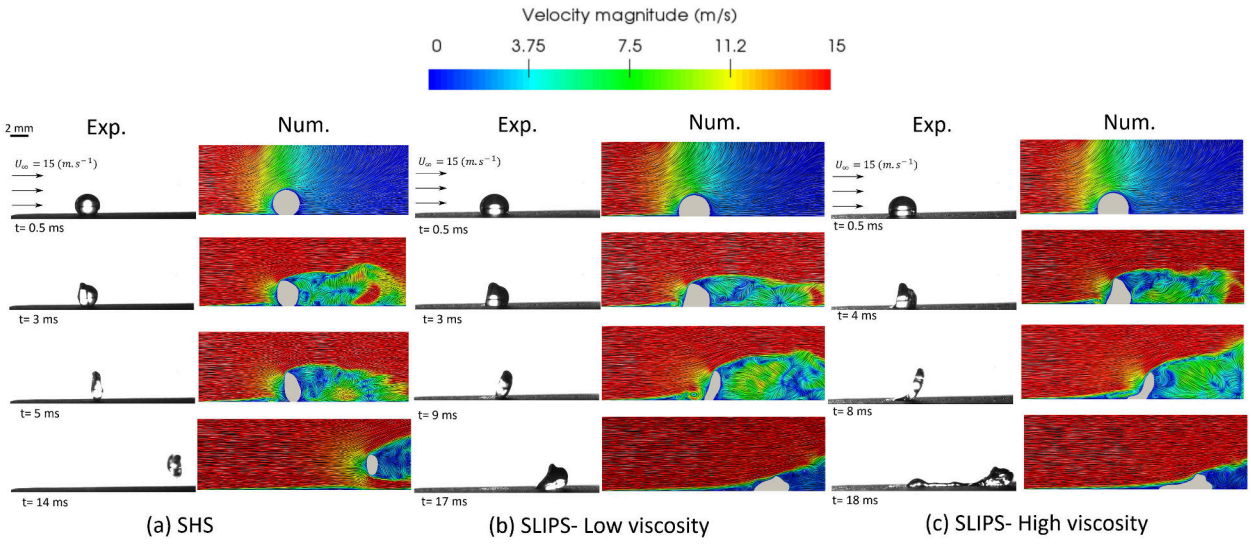

Figure 4.15: Comparison of the numerical simulations (colormaps) and experimental results (greyscale) of droplet shedding at $U_\infty = 15\ m/s$ on (a) SHS, (b) SLIPS-low viscosity and (c) SLIPS-high viscosity

Aerodynamic forces including drag and lift forces on droplet mobility under the effect of air shear flow are illustrated and compared for different surfaces ($U_\infty = 10$ and $15\ m/s$) in Figure 4.17. The drag and lift forces are determined by integrating the pressure field over the surface of the droplet ($F_P = \int_{S_{Droplet}} P(n \cdot dS)$) which is then projected in the parallel and normal components of the air flow direction, respectively. The pressure drag force is in the direction of air flow and it can be seen in Figure 4.17a that at $U_\infty = 15\ m/s$, pressure drag force is greater than $U_\infty = 10\ m/s$ in the few milliseconds of droplet shedding. The larger droplet deformation (larger surface area exposing to the air flow) and higher air flow speed led to the higher pressure drag force. At $U_\infty = 15\ m/s$, the droplet deformed substantially on all surfaces, and a large surface area of the droplet is subjected to air flow. In SHS, the droplet detached from the surface, and a spherical shape forms while on slippery surfaces, the droplet tends to spread on the surface and slide. Thus, less surface area of the droplet was exposed to air flow on slippery surfaces and the pressure drag force decreased significantly. However, the reduction in pressure drag force is less comparable between all surfaces for $U_\infty = 10\ m/s$ as the air flow was less affected the droplet deformation. At $\sim t = 10\ ms$, the lift force of droplet (Figure 4.17b) started decreasing in all cases, while in SHS started to increase and finally detached from the surface at $\sim t = 15\ ms$. For larger air speed ($U_\infty = 15\ m/s$), no significant difference in the lift force of all surfaces was observed until $\sim t = 10\ ms$. Afterward, the lift force in SHS did not change (as the droplet detached completely from the surface) while in slippery surfaces decreased (as the droplet spread and slide on the surface).

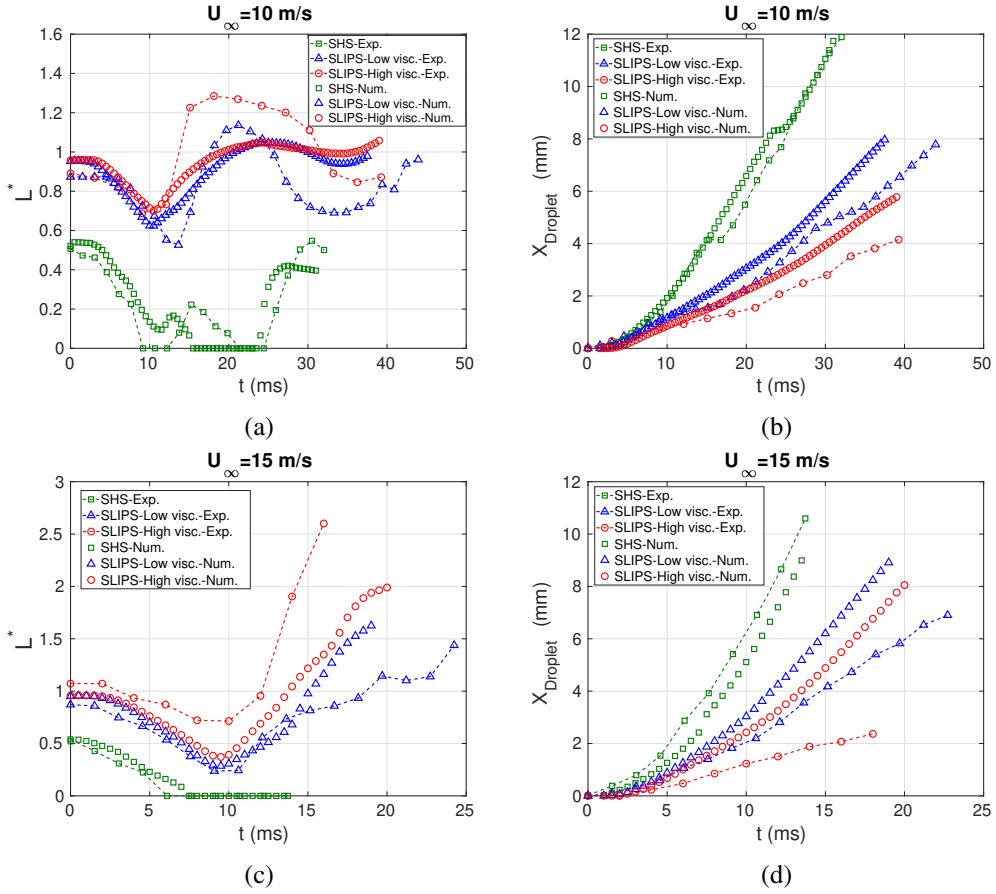

Figure 4.16: Comparison of dimensionless wetting length (L^*) and droplet position (X_{Droplet}) in numerical and experimental results for air flow velocities of 10 m/s (a, b), 15 m/s (c, d) (Error bars due to the digital image processing are not included as the values were small)

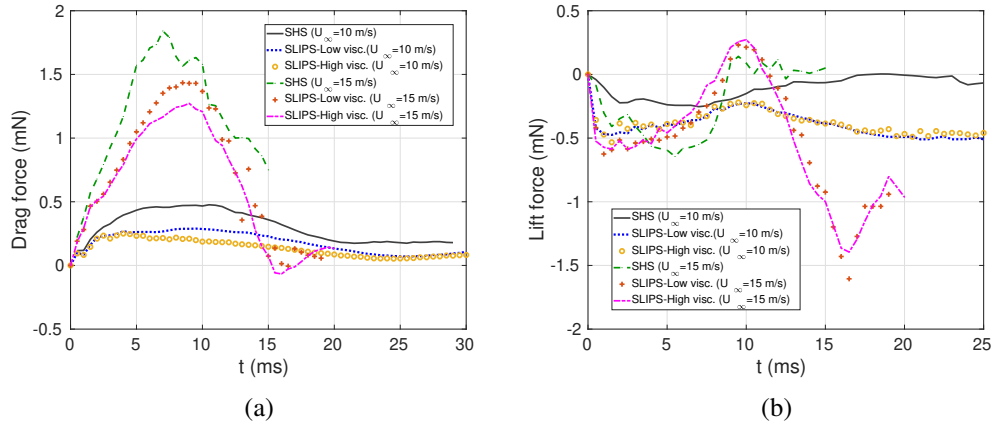

Figure 4.17: (a) Drag and (b) lift force for droplet shedding on SHS and SLIPSs at $U_\infty = 10$ and 15 m/s

4.6 Conclusions

Droplet mobility on superhydrophobic and slippery lubricant impregnated surfaces under the effect of air shear flow with different air speeds (5, 10, 15 and 20 m/s) has been investigated both experimentally and numerically. Two lubricants with different viscosities have been considered in slippery lubricant impregnated surfaces in order to compare their performance. Regarding the surface wettability and droplet mobility, the wetting length and droplet position has been also characterized. A complete droplet shedding occurred in all cases once the airflow speed meets the critical velocity. The results reveal that the droplet shedding on slippery surfaces exhibits different behavior compared to the superhydrophobic surface. Droplet rolls on SHSs while it slides and rolls on SLIPSs. The small base radius of the droplet and large contact angle on SHS led the drag force to overcome the adhesion. Although both slippery surfaces result in similar behavior, however, for the case of high viscosity oil, the droplet speed is smaller. Computational analyses of a representative model problem are conducted using the VOF model coupled with the LES turbulent model in conjunction with the Kistler dynamic contact angle method. A boundary condition on the substrate has been considered to replicate the presence of lubricants on slippery surfaces. In this regard, a velocity boundary condition based on the balance of shear stress has been implemented. A good agreement between the numerical and experimental results has been obtained. It was also observed that the contact angle hysteresis differs in droplet shedding compared to the quasi-static measurements which were also confirmed in the numerical simulation. Given the above findings, it can be concluded that although the slippery lubricant impregnated surfaces result in a complete droplet shedding, their function needs to be thoroughly evaluated. For more practical applications such as droplet freezing in the presence of humidity, the time of droplet sliding is a significant parameter that is required to be as small as possible. This work can be also extended to study the performance of SLIPS compared to SHS for droplet shedding in humid conditions under freezing conditions.

Chapter 5

Conclusions and Suggestions for Future work

5.1 Summary and Conclusions

This thesis explored the behavior of micro and macro droplet interaction with slippery lubricant impregnated surface and investigating how these surfaces can be effective in terms of non-wetting and non-repellency properties compared to superhydrophobic surfaces. In this regard, both numerical and experimental studies have been used to evaluate different parameters. A three-phase volume of fluid (VOF) numerical model has been implemented and developed for an impact of a millimeter size droplet on an immiscible liquid film, resembling the slippery surfaces. The three-phase solver was validated with the analytical model which is based on the balance of the interfacial forces. The hydrodynamics of liquid film behavior is examined for three different thicknesses to evaluate the lubricant function on inducing spontaneous droplet bouncing. Three different Weber numbers $We = 1.5$, 5, and 10 are investigated. It was observed that,

- A noticeable change in droplet spontaneous bouncing occurred because of the air layer entrapment as a result of deformation in liquid film and water droplet dimple formation during the impingement, especially at the few milliseconds of impact.
- The liquid film deformation has been also observed in the thin thickness of the lubricant. Droplet hydrodynamics on the liquid surface is similar to spontaneous bouncing from a solid surface at a low Weber number, $We = 1.5$. This is because the liquid film is more constrained by a solid surface. The

immiscible liquid film deformation is more visible by increasing its thickness to a liquid pool surface.

- The position of the droplet and liquid film has been calculated quantitatively for all cases. The quantitative data showed the air layer entrapment between the droplet and liquid layer during the whole impact process. Moreover, an air bubble is trapped within the droplet in some cases (where the droplet deformation is more affected by the impact velocity or liquid film deformation) during the retracting stage. This is also more noticeable for impact on thick and pool liquid film thicknesses.

- For a higher Weber number ($We = 10$), droplet sticks to the solid surface whereas it was be obtained that due to the presence of an immiscible liquid surface, the probability of droplet bouncing increased.

Then, the effect of surface morphology is taken into account. A micro-droplet impact on slippery lubricant impregnated surfaces has been evaluated as the effect of structures in micro-pillars is more highlighted once it contacts with the micro-scale droplets. A numerical simulation is conducted with a three-phase solver in conjunction with a Kistler dynamic contact angle that has been applied for three-phase flow. The surface topology is evaluated by changing the pitches of micro-pillars. Additionally, different impact velocities have been considered to see the durability and pinning effects. The results obtained are as follows,

- The numerical simulation showed that the dynamics of droplet impact can be significantly affected by the structure of surfaces since both the droplet and surface pillars were on a micro-scale.

- The anti-wetting behavior in superhydrophobic surfaces was restricted to specific surface structures and droplet impact conditions. However, slippery lubricant impregnated surfaces were able to enhance the anti-wetting properties in conditions where SHS failed in droplet repellency.

- The results indicated that the hydrodynamics of a droplet in high-density of micro–pillars ($\xi = 0.1$) was analogous to impact on a solid surface while with low-density micro–pillars ($\xi = 0.23$), droplet dynamics acted like an impact on a thin liquid film surface. Droplet bouncing and partial-bouncing are higher in SLIPS with low-density micro–pillars structures.

- Different dimensionless parameters such a spreading factor, droplet penetration depth within the asperities, and an average of droplet velocity during impingement (β, δ^* and U^*) have been measured to characterize the effect of surface morphology in SLIPS and SHS on droplet dynamics. It was demonstrated that in all our studied superhydrophobic surface cases (except for $2w3p$ at $We = 10.4$), the

droplet was completely pinned to all SHS substrate, while in SLIPS the pinning was less affected by the surface morphologies. In cases with a high Weber number ($We = 166.7$) that no recoiling occurred in SLIPS, the pinning within the micro-pillars still significantly small compared to SHS.

- The results illustrated that this investigation can be used in applications where it is required to avoid the droplet from pinning to the textured surface and the probability of droplet bouncing is higher.

Finally, the mobility of a droplet on slippery lubricant impregnated surfaces (coated with two different lubricants) under the effect of air shear flow with different air speeds have been evaluated both experimentally and numerically. The results were also compared with the shedding on superhydrophobic surfaces. In the experimental work, superhydrophobic surfaces have been prepared by creating a micro/nano-structured of TiO_2 suspension plasma spray method and a final coating of the stearic acid layer. Two lubricants (Krytox GPL101 and Krytox143AB) with different viscosities have been used for slippery surfaces. The numerical simulation has been performed based on the Volume of Fluid method coupled with the Large Eddy Simulation turbulent model in conjunction with the dynamic contact angle method. Additionally, a shear stress boundary condition has been developed and implemented to imitate the effect of lubricant viscosity in the slippery surface in the simulation model. Our findings in both experimental and numerical studies revealed that,

- At the same experimental conditions, the critical velocity for droplet movement on the SHS is lower than SLIPS due to the lower base droplet diameter and a higher contact angle.

- The hydrodynamics of droplet mobility on SHS exhibit rolling behavior that led to droplet detachment while in SLIPS is the combination of rolling and sliding.

- Beyond the critical air flow, a complete droplet shedding on all surfaces occurred. The wetting length and position of a droplet on all surfaces have been measured. The trend of wetting length on both slippery surfaces is approximately similar, while the speed of droplets is greatly affected by the lubricant properties.

- In both numerical simulation and experimental analysis, the maximum and minimum contact angles due to droplet deformation under the effect of air shear flow are different than the advancing and receding contact angle in quasi–static measurements.

5.2 Future work

In addition to the fundamental study on the slippery lubricant impregnated for droplet impact and shedding, the development of slippery lubricant impregnated and superomniphobic surfaces have been classified as new techniques in generating non-wetting surfaces. Thus, numerous works can be done to modify their challenges. A list of proposed future research work is suggested as follows that can be interesting to the readers.

- Investigating the durability and performances of droplet mobility under the effect of air shear flow in slippery surfaces generating by porous substrates which produce more reservoirs for holding the immiscible lubricant.

- Evaluating the slippery surface in encapsulated conditions for micro-droplet impact and compare it with the impregnated condition using the numerical simulation. It would be interesting to observe that on what conditions (such as impact velocity), the encapsulated situation might collapse.

- Studying the impact of a droplet on SLIPS and finding a critical velocity in which the lubricants remain stable and durable. The numerical simulation might provide information on the durability of the liquid film layer on slippery surfaces.

- Investigating an experimental study of droplet impact on SLIPS at freezing conditions and compared their performance with SHS. This study can be extended to droplets impact and shedding on an airfoil surface under freezing conditions in a wind tunnel to evaluate the film thickness. The durability of surfaces can be evaluated by several icing/de-icing processes.

- Experimental study on shedding of droplet liquids with low surface tension and high viscous properties such as complex fluids. This would give us a better perspective of the conditions that the SHS or SLIPS starts collapsing. The durability of lubricant can be evaluated after several experimental studies. Additionally, the self-healing of slippery surfaces can be evaluated.

Appendix A

According to the Neumann's relation and the summation of contact angles at a phase triple junction, the contact angles of each phase can be written as

$$\frac{\sin\theta_w}{\sigma_{oa}} = \frac{\sin\theta_a}{\sigma_{wo}} = \frac{\sin\theta_o}{\sigma_{wa}} \tag{A.1}$$

$$\theta_w + \theta_o + \theta_a = 2\pi \tag{A.2}$$

where θ_w, θ_o and θ_a are the contact angles of the water, oil, and air phases, respectively. By balancing the volume of the droplet at the initial and final states (which contains two spherical caps), the final diameter of the droplet is given by

$$D = D_0 \sqrt[3]{4/a}$$

where D_0 is the initial diameter of the droplet and a is a coefficient that is a function of the contact angles of two other phases, defined as

$$\begin{aligned} a = &\left[\frac{2}{\sin(\pi-\theta_o)} + \frac{1}{tan(\pi-\theta_o)}\right]\left[\frac{1}{\sin(\pi-\theta_o)} - \frac{1}{tan(\pi-\theta_o)}\right]^2 \\ &+ \left[\frac{2}{\sin(\pi-\theta_a)} + \frac{1}{tan(\pi-\theta_a)}\right]\left[\frac{1}{\sin(\pi-\theta_a)} - \frac{1}{tan(\pi-\theta_a)}\right]^2 \end{aligned} \tag{A.3}$$

Two cases were considered: Case 1 (σ_{wa} ; σ_{oa} ; σ_{wo})=(1; 1; 1) and Case 2 (σ_{wa} ; σ_{oa} ; σ_{wo})=(0.8; 1; 1.4). In both cases, the interfacial tensions were scaled by the interfacial tension between oil and air, σ_{oa}. Parameters that were compared included the final diameter of the droplet and the contact angle of each

phase at the triple line. In both cases 1 and 2, the interfacial tensions were scaled by the interfacial tension between oil and air, σ_{oa}. The axisymmetric numerical simulation was performed and the resulting states were compared with the analytical solutions. Parameters that were compared included the final diameter of the droplet and the contact angle of each phase at the triple line. For a droplet with a diameter of 1 mm, the final diameters (D) for cases 1 and 2 can be analytically calculated to be 1.276 mm and 1.074 mm, respectively. In our numerical model, the equilibrium diameters in cases of 1 and 2 reached 1.2 mm and 1.08 mm, respectively, giving errors of about 6% and 1%, respectively, that can be treated as negligible. In order to assess the grid independence of the results for a three-phase flow, numerical simulations were performed at different levels of cell size and the error of final states of steady equilibrium diameter of droplet comparing to the analytical results have been measured as shown in Figure A.1.

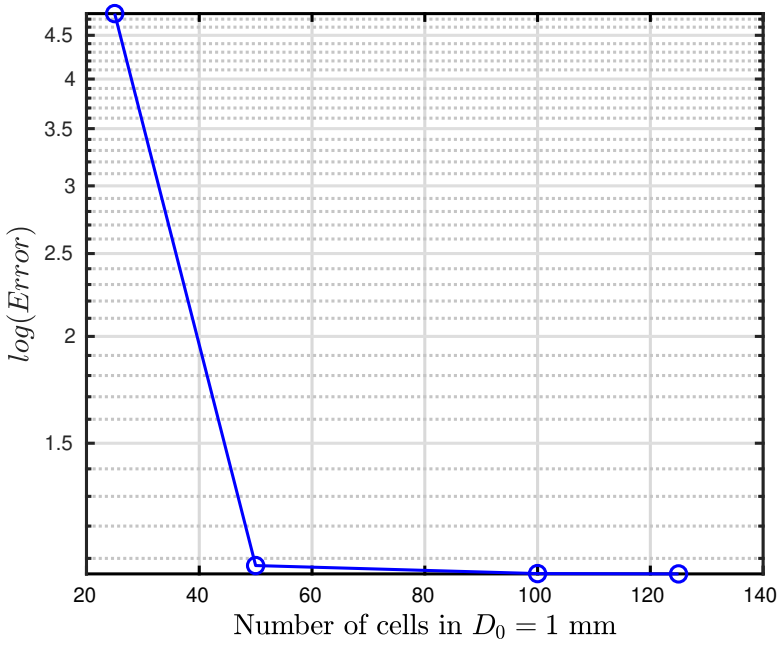

Figure A.1: Error of numerical results for different level of refinement

For the numerical calculation performed at the cell size of 40 μm, the error of the final diameter solution did not compatible with other cell sizes. For finer cell sizes, following the regime of droplet oscillations, the final diameters reached a size approximately equal to the analytical solution. This showed that cell sizes smaller than 40 μm possessed grid independence, and were acceptable cell sizes for use in the model.

The contact angle of phases at the stable conditions are shown for two cases in Figure A.2. The contact angles were measured and compared with the analytical force balance at the triple line, as summarized in

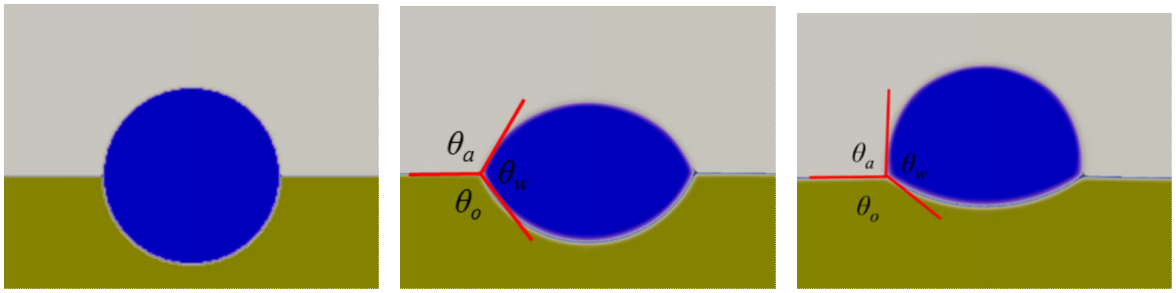

(a) (b) (c)

Figure A.2: Droplet lens at (a) t=0 ms, initial conditions, (b) t=40 ms, similar interfacial tensions (σ_{wa} ; σ_{oa} ; σ_{wo})=(1; 1; 1), (c) t=40 ms, different interfacial tensions (σ_{wa} ; σ_{oa} ; σ_{wo})=(0.8; 1; 1.4)

Table A.1.

Table A.1: The numerical and analytical comparison of contact angle for a droplet lens, case 1: (σ_{wa} ; σ_{oa} ; σ_{wo})=(1; 1; 1) and case 2: (σ_{wa} ; σ_{oa} ; σ_{wo})=(0.8; 1; 1.4)

Contact angle	θ_w		θ_o		θ_a	
Case	1	2	1	2	1	2
Numerical	120°	128°	120°	145°	120°	87°
analytical	120°	136°	120°	146°	120°	78°

To assess the grid independence of the final steady results of contact angles, three-phase flow numerical simulations were performed at different levels of cell size.The errors of final states have been measured (as shown in FigureA.3) comparing to the analyrical values.

It can be seen that the cell size of 40 μm brings significant error to the model, especially in the second case. Increasing the number of cells resulted in reducing the error of the contact angle for different phases comparing to the analytical results.

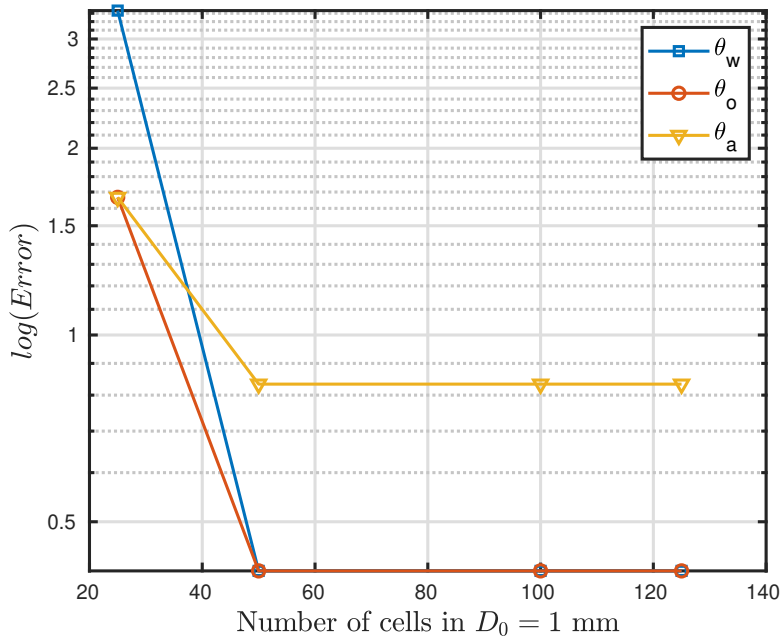

(a)

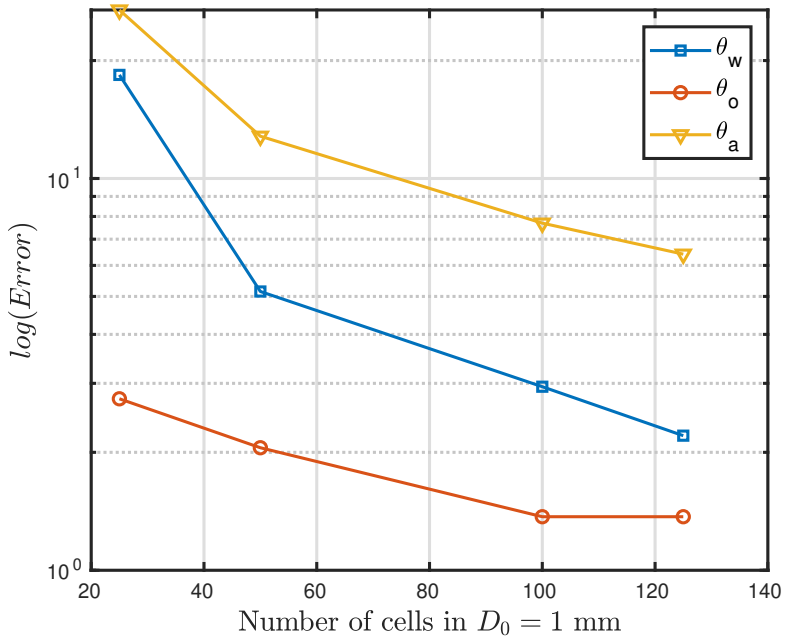

(b)

Figure A.3: Error of predicting contact angle comparing to analytical results for (a) case 1: Same interfacial tensions, (b) case 2: Different interfacial tension

Appendix B

Validation of contact angle model

The Kistler dynamic contact angle solver has been extended and validated for static and dynamic contact angle of three immicible liquid phases. For this purpose, the static contact angle of two immiscible droplets (water and oil) that are exposed to the air has been evaluated. Droplets with the initial diameter of 2 mm were placed on the flat surface as shown in Figure B.1 ($t = 0$). The equilibrium contact angles for water and oil droplets were set as $\theta_{E,w} = 40°$ and $\theta_{E,o} = 120°$. The evolution of the droplet deformation is shown in Figure B.1. It can be seen in Figure B.1 that droplets oscillate until they reached their final equilibrium contact angles. To assess the quantitative data, the equilibrium diameter of a water droplet in the numerical study (Figure B.2) is compared with the final theoretical equilibrium diameter ($\sim 3.83\ mm$) [45]. It can be seen that droplet oscillations reduced until the average oscillation approached the theoretical result.

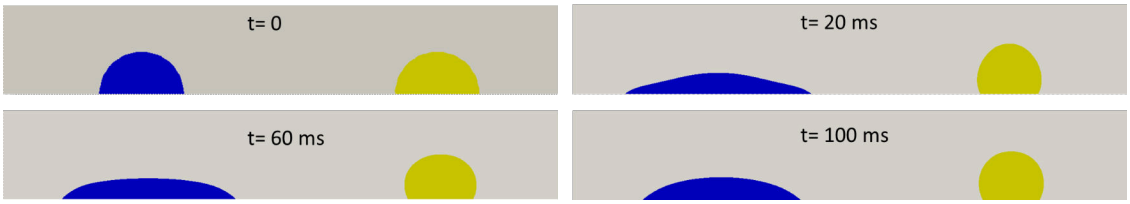

Figure B.1: Evolution of immiscible droplets of water (blue) and oil (yellow) with $\theta_{E,w} = 40°$ and $\theta_{E,o} = 120°$

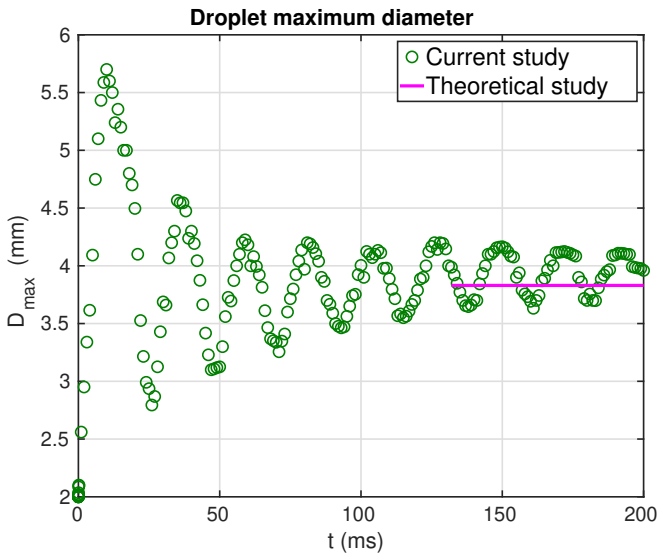

Figure B.2: Comparison of theoretical equilibrium droplet diameter with the numerical oscillation of maximum diameter of water droplet

The performance of the contact angle solver has been also studied for dynamic contact angle problem. A numerical simulation of droplet impact on a smooth flat surface with advancing and receding contact angles of $\theta_A = 107°$ and $\theta_R = 77°$ was modeled using similar initial conditions in the experimental study by Yokoi et al. [171]. A droplet with an initial diameter of $D_0 = 2.28\ mm$ and impact velocity of $V = 1\ m/s$ has been considered. The snapshots of numerical and experimental results of droplet impact are illustrated in Figure B.3 which indicated similar hydrodynamics of droplet. The spreading factor of the droplet during impact is analyzed and compared with the experimental results ([171]) in Figure B.4. The spreading factor is defined as the ratio of maximum droplet diameter during the impingement to the initial droplet diameter ($\beta = {}^{D}/_{D_0}$). The quantitative results indicated also a good agreement in Figure B.4. The multiphase solver in conjunction with the dynamic contact angle model was then employed for the impact of a droplet on slippery lubricant impregnated surfaces that comprise three immiscible liquids.

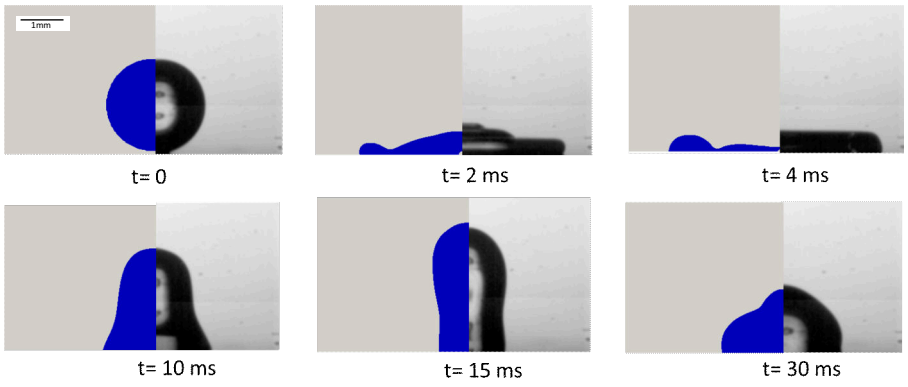

Figure B.3: Evolution of droplet impact on a flat surface (Qualitative evaluation of contact angle method), left (blue): present study and right (grey): experimental study which is reproduced from Yokoi et al. [171], with the permission of AIP Publishing

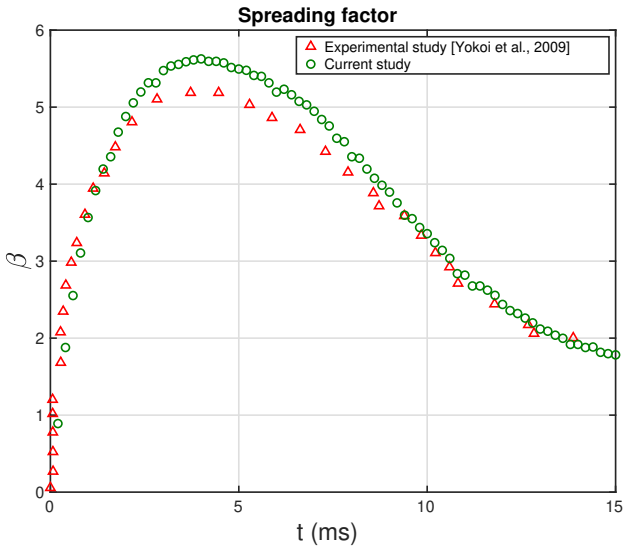

Figure B.4: Comparing of numerical study of maximum droplet spreading factor ($\beta_{\max}$) during impact on a flat surface with the experimental study which is reproduced from Yokoi et al. [171], with the permission of AIP Publishing (Quantitative evaluation of contact angle method)

Appendix C

Validation of shear stress boundary condition

In order to validate the boundary condition of the solver based on the balance of the shear stress equation, a Couette flow problem is considered. As shown in Figure C.1, the Couette flow problem is solved based on modeling the fluid 1 instead of modeling both fluids 1 and 2 such that an appropriate boundary condition is implemented on a substrate. In this regard, a two-dimensional geometry of $0.4 \times 0.1\, m^2$ has been studied where the top surface is moving with the velocity of $V_0 = 1\, m/s$. The schematic of the Couette flow problem is illustrated in Figure C.1. For this purpose, two fluids with viscosities of $\mu_1 = 0.01$ and $\mu_2 = 0.05$ and thicknesses of $\delta_1 = 0.1$ and δ_2 (where δ_2 varied for 0.1, 0.5, 1 and 1.5) has been investigated. The U_I is the interface velocity between two fluids ($\tau_1 = \tau_2$) which is derived based on the balance of shear stress of two fluids at the interface ($U_I = \frac{V_0}{(1+\frac{\mu_2 \delta_1}{\mu_1 \delta_2})}$).

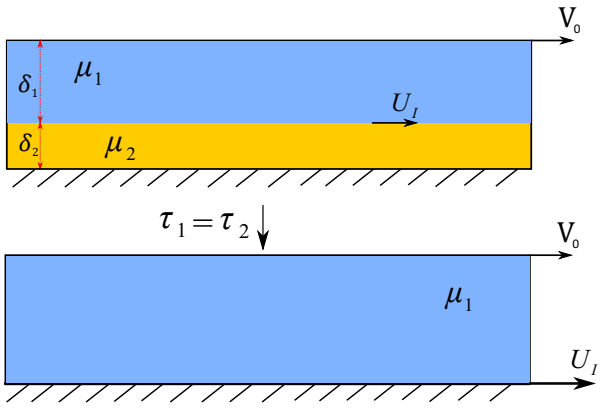

Figure C.1: A schematic of Couette flow problem for the validation of boundary condition

Based on the boundary conditions where the surface velocity is implemented as a result of shear stress balance (Figure 4.6), the numerical model is validated with the theoretical interface velocity U_I, as shown in Figure C.2. It can be seen that the U_I resulted from the numerical study (by implementing the boundary condition) is completely matched with the theoretical values for different thicknesses (δ_2) of the second fluid (μ_2). The velocity distributions based on the boundary conditions for different thicknesses of δ_2 are also illustrated in Figure C.3.

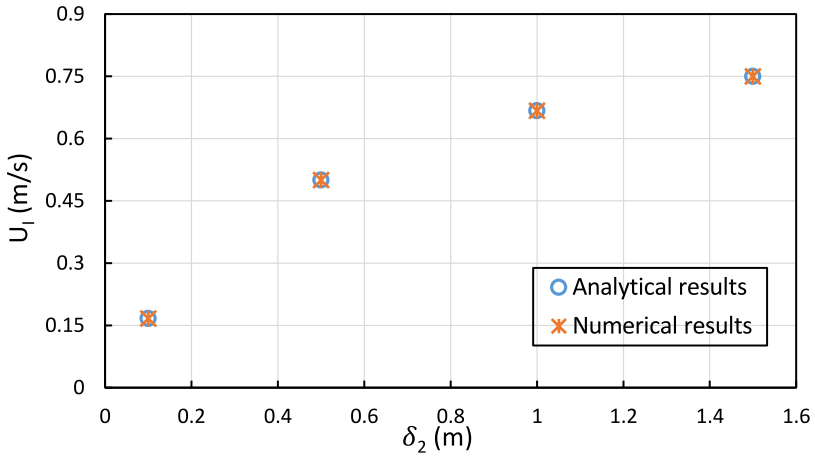

Figure C.2: Comparison of interface velocity (U_I) in numerical study with the analytical results for different δ_2

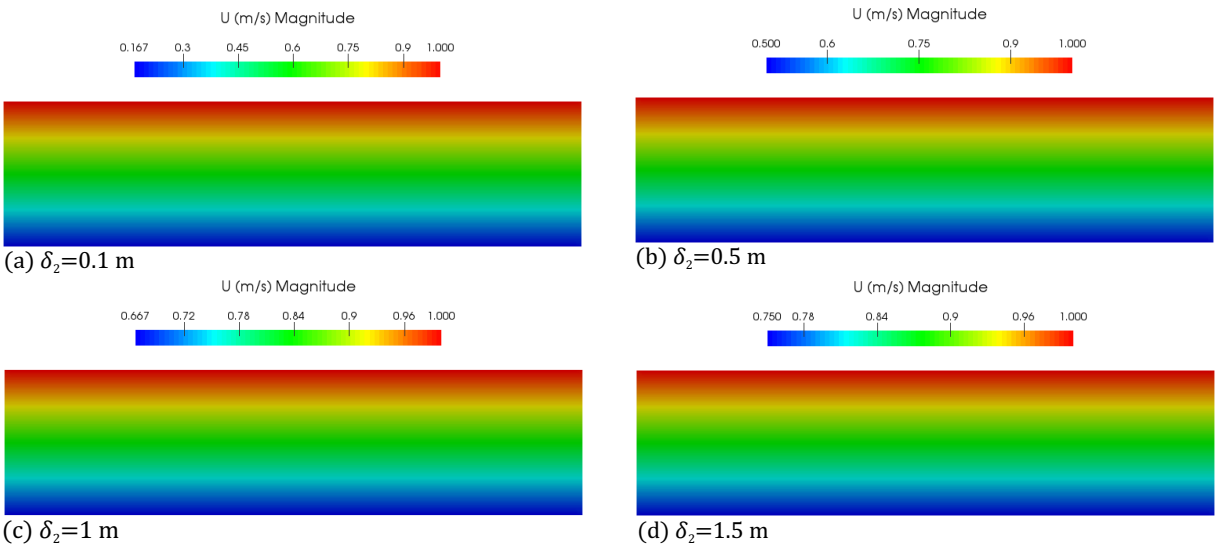

(a) δ_2=0.1 m (b) δ_2=0.5 m

(c) δ_2=1 m (d) δ_2=1.5 m

Figure C.3: Velocity distribution of Couette flow by implementing the boundary condition for different δ_2

C.1 Effect of Oil thickness on droplet mobility

To observe how the oil thickness can affect the droplet motion, two oil thicknesses of $\delta_{\text{oil}} = 100\ \mu m$ and $500\ \mu m$ have been evaluated as shown in Figure C.4. It was observed that the, while the speed of droplet is slightly larger in $\delta_{\text{oil}} = 500\ \mu m$ thickness than $100 \mu m$, while the hydrodynamics of droplet is similar for a $D =\sim 3\ mm$ droplet. Thus, the effect of increasing the thickness of lubricant from $100\ \mu m$ to $500\ \mu m$ on droplet movement is not significant enough.

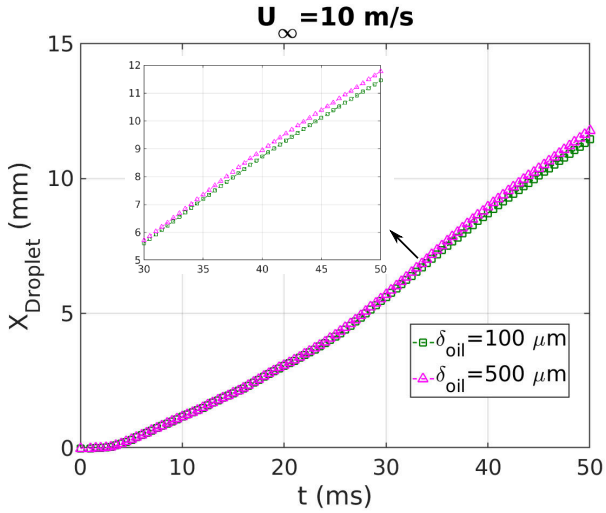

Figure C.4: Effect of low-viscous lubricant thickness on droplet mobility (X_{Droplet})

Bibliography

[1] X. Zhu, J. Lu, X. Li, B. Wang, Y. Song, X. Miao, Z. Wang, and G. Ren. "Simple way to a slippery lubricant impregnated coating with ultrastability and self-replenishment property". In: *Industrial & Engineering Chemistry Research* 58.19 (2019), pp. 8148–8153.

[2] S. S. Latthe, R. S. Sutar, V. S. Kodag, A. Bhosale, A. M. Kumar, K. K. Sadasivuni, R. Xing, and S. Liu. "Self–cleaning superhydrophobic coatings: Potential industrial applications". In: *Progress in Organic Coatings* 128 (2019), pp. 52–58.

[3] A. K. Epstein, T.-S. Wong, R. A. Belisle, E. M. Boggs, and J. Aizenberg. "Liquid-infused structured surfaces with exceptional anti-biofouling performance". In: *Proceedings of the National Academy of Sciences* 109.33 (2012), pp. 13182–13187.

[4] H. Li, X. Feng, Y. Peng, and R. Zeng. "Durable lubricant-infused coating on a magnesium alloy substrate with anti-biofouling and anti-corrosion properties and excellent thermally assisted healing ability". In: *Nanoscale* 12.14 (2020), pp. 7700–7711.

[5] G. B. Hwang, K. Page, A. Patir, S. P. Nair, E. Allan, and I. P. Parkin. "The anti-biofouling properties of superhydrophobic surfaces are short-lived". In: *ACS nano* 12.6 (2018), pp. 6050–6058.

[6] S. S. Latthe, R. S. Sutar, A. K. Bhosale, S. Nagappan, C.-S. Ha, K. K. Sadasivuni, S. Liu, and R. Xing. "Recent developments in air-trapped superhydrophobic and liquid-infused slippery surfaces for anti-icing application". In: *Progress in Organic Coatings* 137 (2019), p. 105373.

[7] T.-B. Nguyen, S. Park, Y. Jung, and H. Lim. "Effects of hydrophobicity and lubricant characteristics on anti-icing performance of slippery lubricant-infused porous surfaces". In: *Journal of Industrial and Engineering Chemistry* 69 (2019), pp. 99–105.

[8] C. Tao, S. Bai, X. Li, C. Li, L. Ren, Y. Zhao, and X. Yuan. “Formation of zwitterionic coatings with an aqueous lubricating layer for antifogging/anti-icing applications”. In: *Progress in Organic Coatings* 115 (2018), pp. 56–64.

[9] H. Luo, S. Yin, S. Huang, F. Chen, Q. Tang, and X. Li. “Fabrication of slippery Zn surface with improved water-impellent, condensation and anti-icing properties”. In: *Applied Surface Science* 470 (2019), pp. 1139–1147.

[10] C. Stamatopoulos, A. Milionis, N. Ackerl, M. Donati, P. Leudet de la Vallee, P. Rudolf von Rohr, and D. Poulikakos. “Droplet self-propulsion on superhydrophobic microtracks”. In: *ACS nano* 14.10 (2020), pp. 12895–12904.

[11] D. Paulssen, S. Hardt, and P. A. Levkin. “Droplet Sorting and Manipulation on Patterned Two-Phase Slippery Lubricant-Infused Surface”. In: *ACS applied materials & interfaces* 11.17 (2019), pp. 16130–16138.

[12] S. R. Yazdi, P. Agrawal, E. Morales, C. A. Stevens, L. Oropeza, P. L. Davies, C. Escobedo, and R. D. Oleschuk. “Facile actuation of aqueous droplets on a superhydrophobic surface using magnetotactic bacteria for digital microfluidic applications”. In: *Analytica chimica acta* 1085 (2019), pp. 107–116.

[13] D. Seo, J. Shim, C. Lee, and Y. Nam. “Brushed lubricant-impregnated surfaces (BLIS) for long-lasting high condensation heat transfer”. In: *Scientific reports* 10.1 (2020), pp. 1–13.

[14] Y. Maeda, F. Lv, P. Zhang, Y. Takata, and D. Orejon. “Condensate droplet size distribution and heat transfer on hierarchical slippery lubricant infused porous surfaces”. In: *Applied Thermal Engineering* 176 (2020), p. 115386.

[15] X. Gao and L. Jiang. “Water-repellent legs of water striders”. In: *Nature* 432.7013 (2004), pp. 36–36.

[16] J.-S. Koh, E. Yang, G.-P. Jung, S.-P. Jung, J. H. Son, S.-I. Lee, P. G. Jablonski, R. J. Wood, H.-Y. Kim, and K.-J. Cho. “Jumping on water: Surface tension–dominated jumping of water striders and robotic insects”. In: *Science* 349.6247 (2015), pp. 517–521.

[17] W. Barthlott and C. Neinhuis. “Purity of the sacred lotus, or escape from contamination in biological surfaces”. In: *Planta* 202.1 (1997), pp. 1–8.

[18] X. Yao, Y. Song, and L. Jiang. “Applications of bio-inspired special wettable surfaces”. In: *Advanced Materials* 23.6 (2011), pp. 719–734.

[19] T.-S. Wong, S. H. Kang, S. K. Tang, E. J. Smythe, B. D. Hatton, A. Grinthal, and J. Aizenberg. “Bioinspired self-repairing slippery surfaces with pressure-stable omniphobicity”. In: *Nature* 477.7365 (2011), p. 443.

[20] S. J. Kim, H. N. Kim, S. J. Lee, and H. J. Sung. “A lubricant-infused slip surface for drag reduction”. In: *Physics of Fluids* 32.9 (2020), p. 091901.

[21] X. Zhang, F. Shi, J. Niu, Y. Jiang, and Z. Wang. “Superhydrophobic surfaces: from structural control to functional application”. In: *Journal of Materials Chemistry* 18.6 (2008), pp. 621–633.

[22] J. B. Boreyko and C. P. Collier. “Delayed frost growth on jumping-drop superhydrophobic surfaces”. In: *ACS nano* 7.2 (2013), pp. 1618–1627.

[23] K. K. Varanasi, T. Deng, J. D. Smith, M. Hsu, and N. Bhate. “Frost formation and ice adhesion on superhydrophobic surfaces”. In: *Applied Physics Letters* 97.23 (2010), p. 234102.

[24] L. Cao, A. K. Jones, V. K. Sikka, J. Wu, and D. Gao. “Anti-icing superhydrophobic coatings”. In: *Langmuir* 25.21 (2009), pp. 12444–12448.

[25] L. Mishchenko, B. Hatton, V. Bahadur, J. A. Taylor, T. Krupenkin, and J. Aizenberg. “Design of ice-free nanostructured surfaces based on repulsion of impacting water droplets”. In: *ACS nano* 4.12 (2010), pp. 7699–7707.

[26] K. A. Wier and T. J. McCarthy. “Condensation on ultrahydrophobic surfaces and its effect on droplet mobility: ultrahydrophobic surfaces are not always water repellant”. In: *Langmuir* 22.6 (2006), pp. 2433–2436.

[27] S. Jung, M. Dorrestijn, D. Raps, A. Das, C. M. Megaridis, and D. Poulikakos. “Are superhydrophobic surfaces best for icephobicity?” In: *Langmuir* 27.6 (2011), pp. 3059–3066.

[28] C. Wang and Z. Guo. “The comparasion between superhydrophobic surfaces (SHS) and slippery liquid infused porous surfaces (SLIPS) in application”. In: *Nanoscale* (2020).

[29] J. Li, E. Ueda, D. Paulssen, and P. A. Levkin. “Slippery lubricant-infused surfaces: properties and emerging applications”. In: *Advanced Functional Materials* 29.4 (2019), p. 1802317.

[30] J. D. Smith, R. Dhiman, S. Anand, E. Reza-Garduno, R. E. Cohen, G. H. McKinley, and K. K. Varanasi. “Droplet mobility on lubricant-impregnated surfaces”. In: *Soft Matter* 9.6 (2013), pp. 1772–1780.

[31] S. Anand, A. T. Paxson, R. Dhiman, J. D. Smith, and K. K. Varanasi. “Enhanced condensation on lubricant-impregnated nanotextured surfaces”. In: *ACS nano* 6.11 (2012), pp. 10122–10129.

[32] K. Rykaczewski, T. Landin, M. L. Walker, J. H. J. Scott, and K. K. Varanasi. “Direct imaging of complex nano-to microscale interfaces involving solid, liquid, and gas phases”. In: *ACS nano* 6.10 (2012), pp. 9326–9334.

[33] F. Schellenberger, J. Xie, N. Encinas, A. Hardy, M. Klapper, P. Papadopoulos, H.-J. Butt, and D. Vollmer. “Direct observation of drops on slippery lubricant-infused surfaces”. In: *Soft Matter* 11.38 (2015), pp. 7617–7626.

[34] J. H. Guan, G. G. Wells, B. Xu, G. McHale, D. Wood, J. Martin, and S. Stuart-Cole. “Evaporation of sessile droplets on slippery liquid-infused porous surfaces (slips)”. In: *Langmuir* 31.43 (2015), pp. 11781–11789.

[35] C. Semprebon, G. McHale, and H. Kusumaatmaja. “Apparent contact angle and contact angle hysteresis on liquid infused surfaces”. In: *Soft matter* 13.1 (2017), pp. 101–110.

[36] B. Derby. “Inkjet printing of functional and structural materials: fluid property requirements, feature stability, and resolution”. In: *Annual Review of Materials Research* 40 (2010), pp. 395–414.

[37] M. Rein. “Phenomena of liquid drop impact on solid and liquid surfaces”. In: *Fluid Dynamics Research* 12.2 (1993), pp. 61–93.

[38] M. Marengo, C. Antonini, I. V. Roisman, and C. Tropea. “Drop collisions with simple and complex surfaces”. In: *Current Opinion in Colloid & Interface Science* 16.4 (2011), pp. 292–302.

[39] R. Rioboo, M. Marengo, and C. Tropea. “Time evolution of liquid drop impact onto solid, dry surfaces”. In: *Experiments in fluids* 33.1 (2002), pp. 112–124.

[40] Y. Couder, E. Fort, C.-H. Gautier, and A. Boudaoud. “From bouncing to floating: noncoalescence of drops on a fluid bath”. In: *Physical review letters* 94.17 (2005), p. 177801.

[41] J. M. Kolinski, L. Mahadevan, and S. Rubinstein. “Drops can bounce from perfectly hydrophilic surfaces”. In: *EPL (Europhysics Letters)* 108.2 (2014), p. 24001.

[42] J. de Ruiter, D. van den Ende, and F. Mugele. “Air cushioning in droplet impact. II. Experimental characterization of the air film evolution”. In: *Physics of fluids* 27.1 (2015), p. 012105.

[43] J. de Ruiter, R. Lagraauw, F. Mugele, and D. van den Ende. “Bouncing on thin air: how squeeze forces in the air film during non-wetting droplet bouncing lead to momentum transfer and dissipation”. In: *Journal of fluid mechanics* 776 (2015), pp. 531–567.

[44] H. Shetabivash and A. Dolatabadi. “Numerical investigation of air mediated droplet bouncing on flat surfaces”. In: *AIP Advances* 7.9 (2017), p. 095003.

[45] F. Yeganehdoust, R. Attarzadeh, I. Karimfazli, and A. Dolatabadi. “A numerical analysis of air entrapment during droplet impact on an immiscible liquid film”. In: *International Journal of Multiphase Flow* 124 (2020), p. 103175.

[46] T. Tran, H. J. Staat, A. Prosperetti, C. Sun, and D. Lohse. “Drop impact on superheated surfaces”. In: *Physical review letters* 108.3 (2012), p. 036101.

[47] R. L. Vander Wal, G. M. Berger, and S. D. Mozes. “Droplets splashing upon films of the same fluid of various depths”. In: *Experiments in fluids* 40.1 (2006), pp. 33–52.

[48] G. Liang and I. Mudawar. “Review of mass and momentum interactions during drop impact on a liquid film”. In: *International Journal of Heat and Mass Transfer* 101 (2016), pp. 577–599.

[49] Z. Che and O. K. Matar. “Impact of droplets on immiscible liquid films”. In: *Soft matter* 14.9 (2018), pp. 1540–1551.

[50] X. Tang, A. Saha, C. K. Law, and C. Sun. “Bouncing drop on liquid film: Dynamics of interfacial gas layer”. In: *Physics of Fluids* 31.1 (2019), p. 013304.

[51] N. Chen, H. Chen, and A. Amirfazli. “Drop impact onto a thin film: Miscibility effect”. In: *Physics of Fluids* 29.9 (2017), p. 092106.

[52] J. Genzer and K. Efimenko. “Recent developments in superhydrophobic surfaces and their relevance to marine fouling: a review”. In: *Biofouling* 22.5 (2006), pp. 339–360.

[53] D. Khojasteh, M. Kazerooni, S. Salarian, and R. Kamali. “Droplet impact on superhydrophobic surfaces: A review of recent developments”. In: *Journal of Industrial and Engineering Chemistry* 42 (2016), pp. 1–14.

[54] J. Li, Y. Hou, Y. Liu, C. Hao, M. Li, M. K. Chaudhury, S. Yao, and Z. Wang. “Directional transport of high-temperature Janus droplets mediated by structural topography”. In: *Nature Physics* 12.6 (2016), pp. 606–612.

[55] N. D. Patil, R. Bhardwaj, and A. Sharma. “Droplet impact dynamics on micropillared hydrophobic surfaces”. In: *Experimental Thermal and Fluid Science* 74 (2016), pp. 195–206.

[56] C. Antonini, A. Amirfazli, and M. Marengo. “Drop impact and wettability: From hydrophilic to superhydrophobic surfaces”. In: *Physics of fluids* 24.10 (2012), p. 102104.

[57] R. Zhang, P. Hao, X. Zhang, and F. He. “Supercooled water droplet impact on superhydrophobic surfaces with various roughness and temperature”. In: *International Journal of Heat and Mass Transfer* 122 (2018), pp. 395–402.

[58] S. Baek, H. S. Moon, W. Kim, S. Jeon, and K. Yong. “Effect of liquid droplet surface tension on impact dynamics over hierarchical nanostructure surfaces”. In: *Nanoscale* 10.37 (2018), pp. 17842–17851.

[59] D. Bartolo, F. Bouamrirene, E. Verneuil, A. Buguin, P. Silberzan, and S. Moulinet. “Bouncing or sticky droplets: Impalement transitions on superhydrophobic micropatterned surfaces”. In: *EPL (Europhysics Letters)* 74.2 (2006), p. 299.

[60] P. G. Bange and R. Bhardwaj. “Computational study of bouncing and non-bouncing droplets impacting on superhydrophobic surfaces”. In: *Theoretical and Computational Fluid Dynamics* 30.3 (2016), pp. 211–235.

[61] M. Tembely, R. Attarzadeh, and A. Dolatabadi. “On the numerical modeling of supercooled microdroplet impact and freezing on superhydrophobic surfaces”. In: *International Journal of Heat and Mass Transfer* 127 (2018), pp. 193–202.

[62] R. Attarzadeh and A. Dolatabadi. “Icephobic performance of superhydrophobic coatings: A numerical analysis”. In: *International Journal of Heat and Mass Transfer* 136 (2019), pp. 1327–1337.

[63] D. Hee Kwon and S. Joon Lee. “Impact and wetting behaviors of impinging microdroplets on superhydrophobic textured surfaces”. In: *Applied Physics Letters* 100.17 (2012), p. 171601.

[64] T. Bobinski, G. Sobieraj, M. Psarski, G. Celichowski, and J. Rokicki. “Droplet bouncing on the surface with micro-structure”. In: *Arch. Mech* 69 (2017), pp. 177–193.

[65] H. Gomaa, M. Tembely, N. Esmail, and A. Dolatabadi. “Bouncing of cloud-sized microdroplets on superhydrophobic surfaces”. In: *Physics of Fluids* 32.12 (2020), p. 122118.

[66] R. Chen, L. Jiao, X. Zhu, Q. Liao, D. Ye, B. Zhang, W. Li, Y. Lei, and D. Li. “Cassie-to-Wenzel transition of droplet on the superhydrophobic surface caused by light induced evaporation”. In: *Applied Thermal Engineering* 144 (2018), pp. 945–959.

[67] A. Sudeepthi, L. Yeo, and A. Sen. “Cassie–Wenzel wetting transition on nanostructured superhydrophobic surfaces induced by surface acoustic waves”. In: *Applied Physics Letters* 116.9 (2020), p. 093704.

[68] T. Deng, K. K. Varanasi, M. Hsu, N. Bhate, C. Keimel, J. Stein, and M. Blohm. “Nonwetting of impinging droplets on textured surfaces”. In: *Applied Physics Letters* 94.13 (2009), p. 133109.

[69] S. Dash, M. T. Alt, and S. V. Garimella. “Hybrid surface design for robust superhydrophobicity”. In: *Langmuir* 28.25 (2012), pp. 9606–9615.

[70] M. Abolghasemibizaki and R. Mohammadi. “Droplet impact on superhydrophobic surfaces fully decorated with cylindrical macrotextures”. In: *Journal of colloid and interface science* 509 (2018), pp. 422–431.

[71] L. Bocquet and E. Lauga. “A smooth future?” In: *Nature materials* 10.5 (2011), pp. 334–337.

[72] D. Quéré. “Wetting and roughness”. In: *Annu. Rev. Mater. Res.* 38 (2008), pp. 71–99.

[73] S. Bengaluru Subramanyam, V. Kondrashov, J. Ruhe, and K. K. Varanasi. “Low ice adhesion on nano-textured superhydrophobic surfaces under supersaturated conditions”. In: *ACS applied materials & interfaces* 8.20 (2016), pp. 12583–12587.

[74] K. Tsujii, T. Yamamoto, T. Onda, and S. Shibuichi. “Super oil-repellent surfaces”. In: *Angewandte Chemie International Edition in English* 36.9 (1997), pp. 1011–1012.

[75] A. K. Kota, W. Choi, and A. Tuteja. “Superomniphobic surfaces: Design and durability”. In: *MRS bulletin* 38.5 (2013), pp. 383–390.

[76] M. Ezazi, B. Shrestha, N. Klein, D. H. Lee, S. Seo, and G. Kwon. “Self-healable superomniphobic surfaces for corrosion protection”. In: *ACS applied materials & interfaces* 11.33 (2019), pp. 30240–30246.

[77] D. Quéré. “Non-sticking drops”. In: *Reports on Progress in Physics* 68.11 (2005), p. 2495.

[78] Z. Wang, L. Heng, and L. Jiang. “Effect of lubricant viscosity on the self-healing properties and electrically driven sliding of droplets on anisotropic slippery surfaces”. In: *Journal of Materials Chemistry A* 6.8 (2018), pp. 3414–3421.

[79] X. Chen, G. Wen, and Z. Guo. “What are the design principles, from the choice of lubricants and structures to the preparation method, for a stable slippery lubricant-infused porous surface?” In: *Materials Horizons* 7.7 (2020), pp. 1697–1726.

[80] B. Shang, M. Chen, and L. Wu. “Fabrication of UV-triggered liquid-repellent coatings with long-term self-repairing performance”. In: *ACS applied materials & interfaces* 10.37 (2018), pp. 31777–31783.

[81] J.-H. Kim and J. P. Rothstein. “Droplet impact dynamics on lubricant-infused superhydrophobic surfaces: The role of viscosity ratio”. In: *Langmuir* 32.40 (2016), pp. 10166–10176.

[82] C. Lee, H. Kim, and Y. Nam. “Drop impact dynamics on oil-infused nanostructured surfaces”. In: *Langmuir* 30.28 (2014), pp. 8400–8407.

[83] F. Yeganehdoust, I. Karimfazli, and A. Dolatabadi. “Numerical Analysis of Droplet Impact on a Smooth Slippery Surface”. In: *ASME 2018 5th Joint US-European Fluids Engineering Division Summer Meeting*. American Society of Mechanical Engineers. 2018, V001T15A005–V001T15A005.

[84] C. Hao, J. Li, Y. Liu, X. Zhou, Y. Liu, R. Liu, L. Che, W. Zhou, D. Sun, L. Li, et al. “Superhydrophobic-like tunable droplet bouncing on slippery liquid interfaces”. In: *Nature communications* 6 (2015), p. 7986.

[85] G. Minor. “Experimental study of water droplet flows in a model PEM fuel cell gas microchannel”. PhD thesis. 2007.

[86] S. Hodges and O. Jensen. “Spreading and peeling dynamics in a model of cell adhesion”. In: *Journal of Fluid Mechanics* 460 (2002), p. 381.

[87] S. Moghtadernejad, M. Tembely, M. Jadidi, N. Esmail, and A. Dolatabadi. “Shear driven droplet shedding and coalescence on a superhydrophobic surface”. In: *Physics of Fluids* 27.3 (2015), p. 032106.

[88] A. Milne and A. Amirfazli. “Drop shedding by shear flow for hydrophilic to superhydrophobic surfaces”. In: *Langmuir* 25.24 (2009), pp. 14155–14164.

[89] A. Razzaghi, S. Banitabaei, and A. Amirfazli. “Shedding of multiple sessile droplets by an airflow”. In: *Physics of Fluids* 30.8 (2018), p. 087104.

[90] A. Razzaghi and A. Amirfazli. “Shedding of a pair of sessile droplets”. In: *International Journal of Multiphase Flow* 110 (2019), pp. 59–68.

[91] S. Moghtadernejad, M. Jadidi, K. T. Ahmmed, C. Lee, A. Dolatabadi, and A.-M. Kietzig. “Experimental study of droplet shedding on laser-patterned substrates”. In: *Physics of Fluids* 31.12 (2019), p. 122107.

[92] C. Stamatopoulos, T. M. Schutzius, C. J. Köppl, N. El Hayek, T. Maitra, J. Hemrle, and D. Poulikakos. “On the shedding of impaled droplets: The role of transient intervening layers”. In: *Scientific reports* 6.1 (2016), pp. 1–9.

[93] D. Daniel, M. N. Mankin, R. A. Belisle, T.-S. Wong, and J. Aizenberg. “Lubricant-infused micro/nano-structured surfaces with tunable dynamic omniphobicity at high temperatures”. In: *Applied Physics Letters* 102.23 (2013), p. 231603.

[94] G. Mistura and M. Pierno. “Drop mobility on chemically heterogeneous and lubricant-impregnated surfaces”. In: *Advances in Physics: X* 2.3 (2017), pp. 591–607.

[95] B. V. Orme, G. McHale, R. Ledesma-Aguilar, and G. G. Wells. “Droplet retention and shedding on slippery substrates”. In: *Langmuir* 35.28 (2019), pp. 9146–9151.

[96] L. Guo, G. Tang, and S. Kumar. “Droplet morphology and mobility on lubricant-impregnated surfaces: a molecular dynamics study”. In: *Langmuir* 35.49 (2019), pp. 16377–16387.

[97] B. R. Solomon, K. S. Khalil, and K. K. Varanasi. “Drag reduction using lubricant-impregnated surfaces in viscous laminar flow”. In: *Langmuir* 30.36 (2014), pp. 10970–10976.

[98] A. McDonald, M. Lamontagne, C. Moreau, and S. Chandra. “Impact of plasma-sprayed metal particles on hot and cold glass surfaces”. In: *Thin Solid Films* 514.1-2 (2006), pp. 212–222.

[99] S. D. Aziz and S. Chandra. “Impact, recoil and splashing of molten metal droplets”. In: *International journal of heat and mass transfer* 43.16 (2000), pp. 2841–2857.

[100] A. Davanlou and R. Kumar. “Thermally induced collision of droplets in an immiscible outer fluid”. In: *Scientific reports* 5 (2015), p. 9531.

[101] F. Blanchette and T. P. Bigioni. “Partial coalescence of drops at liquid interfaces”. In: *Nature Physics* 2.4 (2006), p. 254.

[102] A.-B. Wang and C.-C. Chen. “Splashing impact of a single drop onto very thin liquid films”. In: *Physics of fluids* 12.9 (2000), pp. 2155–2158.

[103] T. Gilet and J. W. Bush. “Droplets bouncing on a wet, inclined surface”. In: *Physics of Fluids* 24.12 (2012), p. 122103.

[104] C. Tropea and M. Marengo. “The impact of drops on walls and films”. In: *Multiphase Science and Technology* 11.1 (1999).

[105] S. Howison, J. Ockendon, J. Oliver, R. Purvis, and F. Smith. “Droplet impact on a thin fluid layer”. In: *Journal of Fluid Mechanics* 542 (2005), pp. 1–23.

[106] S. Chandra and C. Avedisian. “On the collision of a droplet with a solid surface”. In: *Proceedings of the Royal Society of London. Series A: Mathematical and Physical Sciences* 432.1884 (1991), pp. 13–41.

[107] J. De Ruiter, R. Lagraauw, D. Van Den Ende, and F. Mugele. “Wettability-independent bouncing on flat surfaces mediated by thin air films”. In: *Nature physics* 11.1 (2015), p. 48.

[108] C. Josserand and S. T. Thoroddsen. “Drop impact on a solid surface”. In: *Annual review of fluid mechanics* 48 (2016), pp. 365–391.

[109] V. Mehdi-Nejad, J. Mostaghimi, and S. Chandra. “Air bubble entrapment under an impacting droplet”. In: *Physics of fluids* 15.1 (2003), pp. 173–183.

[110] M. Cao, D. Guo, C. Yu, K. Li, M. Liu, and L. Jiang. “Water-repellent properties of superhydrophobic and lubricant-infused “slippery” surfaces: A brief study on the functions and applications”. In: *ACS applied materials & interfaces* 8.6 (2015), pp. 3615–3623.

[111] F. Marcotte, G.-J. Michon, T. Séon, and C. Josserand. “Ejecta, corolla, and splashes from drop impacts on viscous fluids”. In: *Physical review letters* 122.1 (2019), p. 014501.

[112] H. M. Kittel, I. V. Roisman, and C. Tropea. “Splash of a drop impacting onto a solid substrate wetted by a thin film of another liquid”. In: *Physical Review Fluids* 3.7 (2018), p. 073601.

[113] H. M. Kittel, E. Alam, I. V. Roisman, C. Tropea, and T. Gambaryan-Roisman. “Splashing of a Newtonian drop impacted onto a solid substrate coated by a thin soft layer”. In: *Colloids and Surfaces A: Physicochemical and Engineering Aspects* 553 (2018), pp. 89–96.

[114] X. Tang, A. Saha, C. K. Law, and C. Sun. “Nonmonotonic response of drop impacting on liquid film: mechanism and scaling”. In: *Soft Matter* 12.20 (2016), pp. 4521–4529.

[115] T. Tran, H. de Maleprade, C. Sun, and D. Lohse. “Air entrainment during impact of droplets on liquid surfaces”. In: *Journal of fluid mechanics* 726 (2013).

[116] R. Attarzadeh and A. Dolatabadi. “Coalescence-induced jumping of micro-droplets on heterogeneous superhydrophobic surfaces”. In: *Physics of Fluids* 29.1 (2017), p. 012104.

[117] J. Klostermann, K. Schaake, and R. Schwarze. “Numerical simulation of a single rising bubble by VOF with surface compression”. In: *International Journal for Numerical Methods in Fluids* 71.8 (2013), pp. 960–982.

[118] G. Son. “Efficient implementation of a coupled level-set and volume-of-fluid method for three-dimensional incompressible two-phase flows”. In: *Numerical Heat Transfer: Part B: Fundamentals* 43.6 (2003), pp. 549–565.

[119] N. Tofighi and M. Yildiz. “Numerical simulation of single droplet dynamics in three-phase flows using ISPH”. In: *Computers & Mathematics with Applications* 66.4 (2013), pp. 525–536.

[120] N. Weber, P. Beckstein, W. Herreman, G. M. Horstmann, C. Nore, F. Stefani, and T. Weier. “Sloshing instability and electrolyte layer rupture in liquid metal batteries”. In: *Physics of Fluids* 29.5 (2017), p. 054101.

[121] F. Boyer, C. Lapuerta, S. Minjeaud, B. Piar, and M. Quintard. “Cahn–Hilliard/Navier–Stokes model for the simulation of three-phase flows”. In: *Transport in Porous Media* 82.3 (2010), pp. 463–483.

[122] K. A. Smith, F. J. Solis, and D. Chopp. “A projection method for motion of triple junctions by level sets”. In: *Interfaces and free boundaries* 4.3 (2002), pp. 263–276.

[123] G. Tryggvason, B. Bunner, A. Esmaeeli, D. Juric, N. Al-Rawahi, W. Tauber, J. Han, S. Nas, and Y.-J. Jan. “A front-tracking method for the computations of multiphase flow”. In: *Journal of computational physics* 169.2 (2001), pp. 708–759.

[124] C. W. Hirt and B. D. Nichols. “Volume of fluid (VOF) method for the dynamics of free boundaries”. In: *Journal of computational physics* 39.1 (1981), pp. 201–225.

[125] F. Yeganehdoust, M. Yaghoubi, H. Emdad, and M. Ordoubadi. “Numerical study of multiphase droplet dynamics and contact angles by smoothed particle hydrodynamics”. In: *Applied Mathematical Modelling* 40.19-20 (2016), pp. 8493–8512.

[126] M. Ordoubadi, M. Yaghoubi, and F. Yeganehdoust. “Surface tension simulation of free surface flows using smoothed particle hydrodynamics”. In: *Scientia Iranica* 24.4 (2017), pp. 2019–2033.

[127] J. U. Brackbill, D. B. Kothe, and C. Zemach. “A continuum method for modeling surface tension”. In: *Journal of computational physics* 100.2 (1992), pp. 335–354.

[128] *OpenFOAM*. `http://openfoam.com`. 2011.

[129] L. Chen, J. Wu, Z. Li, and S. Yao. “Evolution of entrapped air under bouncing droplets on viscoelastic surfaces”. In: *Colloids and Surfaces A: Physicochemical and Engineering Aspects* 384.1-3 (2011), pp. 726–732.

[130] L. Chen, E. Bonaccurso, P. Deng, and H. Zhang. “Droplet impact on soft viscoelastic surfaces”. In: *Physical Review E* 94.6 (2016), p. 063117.

[131] S. Lin, B. Zhao, S. Zou, J. Guo, Z. Wei, and L. Chen. “Impact of viscous droplets on different wettable surfaces: Impact phenomena, the maximum spreading factor, spreading time and post-impact oscillation”. In: *Journal of colloid and interface science* 516 (2018), pp. 86–97.

[132] W. Bouwhuis, R. C. van der Veen, T. Tran, D. L. Keij, K. G. Winkels, I. R. Peters, D. van der Meer, C. Sun, J. H. Snoeijer, and D. Lohse. “Maximal air bubble entrainment at liquid-drop impact”. In: *Physical review letters* 109.26 (2012), p. 264501.

[133] P. Kim, T.-S. Wong, J. Alvarenga, M. J. Kreder, W. E. Adorno-Martinez, and J. Aizenberg. “Liquid-infused nanostructured surfaces with extreme anti-ice and anti-frost performance”. In: *ACS nano* 6.8 (2012), pp. 6569–6577.

[134] M. J. Kreder, J. Alvarenga, P. Kim, and J. Aizenberg. “Design of anti-icing surfaces: smooth, textured or slippery?” In: *Nature Reviews Materials* 1.1 (2016), pp. 1–15.

[135] Y. H. Yeong, C. Wang, K. J. Wynne, and M. C. Gupta. “Oil-infused superhydrophobic silicone material for low ice adhesion with long-term infusion stability”. In: *ACS applied materials & interfaces* 8.46 (2016), pp. 32050–32059.

[136] J. Jiang, H. Zhang, W. He, T. Li, H. Li, P. Liu, M. Liu, Z. Wang, Z. Wang, and X. Yao. “Adhesion of microdroplets on water-repellent surfaces toward the prevention of surface fouling and pathogen spreading by respiratory droplets”. In: *ACS applied materials & interfaces* 9.7 (2017), pp. 6599–6608.

[137] P. Zhang, L. Lin, D. Zang, X. Guo, and M. Liu. “Designing Bioinspired Anti-Biofouling Surfaces based on a Superwettability Strategy”. In: *Small* 13.4 (2017), p. 1503334.

[138] M. Nenad, X. Rong, D. J. Preston, R. Enright, I. McKay, and E. N. Wang. “Condensation on hydrophilic, hydrophobic, nanostructured superhydrophobic and oil-infused surfaces”. In: (2013).

[139] R. Xiao, N. Miljkovic, R. Enright, and E. N. Wang. “Immersion condensation on oil-infused heterogeneous surfaces for enhanced heat transfer”. In: *Scientific reports* 3 (2013), p. 1988.

[140] S. Chaudhuri, S. Basu, P. Kabi, V. R. Unni, and A. Saha. “Modeling the role of respiratory droplets in Covid-19 type pandemics”. In: *Physics of Fluids* 32.6 (2020), p. 063309.

[141] A. Lafuma and D. Quéré. “Slippery pre-suffused surfaces”. In: *EPL (Europhysics Letters)* 96.5 (2011), p. 56001.

[142] S. B. Subramanyam, K. Rykaczewski, and K. K. Varanasi. “Ice adhesion on lubricant-impregnated textured surfaces”. In: *Langmuir* 29.44 (2013), pp. 13414–13418.

[143] J. S. Wexler, A. Grosskopf, M. Chow, Y. Fan, I. Jacobi, and H. A. Stone. “Robust liquid-infused surfaces through patterned wettability”. In: *Soft Matter* 11.25 (2015), pp. 5023–5029.

[144] A. Al-Azawi, C. Hörenz, T. Tupasela, O. Ikkala, V. Jokinen, S. Franssila, and R. H. Ras. “Slippery and magnetically responsive micropillared surfaces for manipulation of droplets and beads”. In: *AIP Advances* 10.8 (2020), p. 085021.

[145] S. J. Lee, H. N. Kim, W. Choi, G. Y. Yoon, and E. Seo. “A nature-inspired lubricant-infused surface for sustainable drag reduction”. In: *Soft Matter* 15.42 (2019), pp. 8459–8467.

[146] M. Villegas, Y. Zhang, N. Abu Jarad, L. Soleymani, and T. F. Didar. “Liquid-Infused Surfaces: A Review of Theory, Design, and Applications”. In: *ACS nano* 13.8 (2019), pp. 8517–8536.

[147] B. Jin, M. Liu, Q. Zhang, X. Zhan, and F. Chen. “Silicone oil swelling slippery surfaces based on mussel-inspired magnetic nanoparticles with multiple self-healing mechanisms”. In: *Langmuir* 33.39 (2017), pp. 10340–10350.

[148] M. Muschi, B. Brudieu, J. Teisseire, and A. Sauret. “Drop impact dynamics on slippery liquid-infused porous surfaces: influence of oil thickness”. In: *Soft Matter* 14.7 (2018), pp. 1100–1107.

[149] R. Feng, C. Xu, F. Song, F. Wang, X.-L. Wang, and Y.-Z. Wang. “A Bioinspired Slippery Surface with Stable Lubricant Impregnation for Efficient Water Harvesting”. In: *ACS Applied Materials & Interfaces* 12.10 (2020), pp. 12373–12381.

[150] Q. N. Pham, S. Zhang, K. Montazeri, and Y. Won. “Droplets on Slippery Lubricant-Infused Porous Surfaces: A Macroscale to Nanoscale Perspective”. In: *Langmuir* 34.47 (2018), pp. 14439–14447.

[151] D. J. Preston, Y. Song, Z. Lu, D. S. Antao, and E. N. Wang. “Design of lubricant infused surfaces”. In: *ACS applied materials & interfaces* 9.48 (2017), pp. 42383–42392.

[152] N. Sharifi, M. Pugh, C. Moreau, and A. Dolatabadi. “Developing hydrophobic and superhydrophobic TiO2 coatings by plasma spraying”. In: *Surface and Coatings Technology* 289 (2016), pp. 29–36.

[153] N. Sharifi, F. B. Ettouil, C. Moreau, A. Dolatabadi, and M. Pugh. “Engineering surface texture and hierarchical morphology of suspension plasma sprayed TiO2 coatings to control wetting behavior and superhydrophobic properties”. In: *Surface and Coatings Technology* 329 (2017), pp. 139–148.

[154] H. Ding and P. D. Spelt. “Inertial effects in droplet spreading: a comparison between diffuse-interface and level-set simulations”. In: *Journal of fluid mechanics* 576 (2007), p. 287.

[155] N. D. Patil, V. H. Gada, A. Sharma, and R. Bhardwaj. “On dual-grid level-set method for contact line modeling during impact of a droplet on hydrophobic and superhydrophobic surfaces”. In: *International Journal of Multiphase Flow* 81 (2016), pp. 54–66.

[156] H. Rusche. “Computational fluid dynamics of dispersed two-phase flows at high phase fractions”. PhD thesis. 2002.

[157] S. F. Kistler. “Hydrodynamics of wetting”. In: *Wettability* 6 (1993), pp. 311–430.

[158] J. Göhl, A. Mark, S. Sasic, and F. Edelvik. “An immersed boundary based dynamic contact angle framework for handling complex surfaces of mixed wettabilities”. In: *International Journal of Multiphase Flow* 109 (2018), pp. 164–177.

[159] S. Nishimoto and B. Bhushan. “Bioinspired self-cleaning surfaces with superhydrophobicity, superoleophobicity, and superhydrophilicity”. In: *Rsc Advances* 3.3 (2013), pp. 671–690.

[160] Y. Lu, S. Sathasivam, J. Song, C. R. Crick, C. J. Carmalt, and I. P. Parkin. “Robust self-cleaning surfaces that function when exposed to either air or oil”. In: *Science* 347.6226 (2015), pp. 1132–1135.

[161] Q. Ma, W. Wang, and G. Dong. “Facile fabrication of biomimetic liquid-infused slippery surface on carbon steel and its self-cleaning, anti-corrosion, anti-frosting and tribological properties”. In: *Colloids and Surfaces A: Physicochemical and Engineering Aspects* 577 (2019), pp. 17–26.

[162] K. Han, L. Heng, Y. Zhang, Y. Liu, and L. Jiang. “Slippery surface based on photoelectric responsive nanoporous composites with optimal wettability region for droplets’ multifunctional manipulation”. In: *Advanced Science* 6.1 (2019), p. 1801231.

[163] S. Mettu and M. K. Chaudhury. “Motion of drops on a surface induced by thermal gradient and vibration”. In: *Langmuir* 24.19 (2008), pp. 10833–10837.

[164] M. Moradi, M. H. Rahimian, and S. F. Chini. “Numerical investigation of vibration-induced droplet shedding on smooth surfaces with large contact angles”. In: *Physical Review E* 100.2 (2019), p. 023105.

[165] E. D. Wikramanayake, J. Perry, and V. Bahadur. “AC electrowetting promoted droplet shedding on hydrophobic surfaces”. In: *Applied Physics Letters* 116.19 (2020), p. 193701.

[166] F. Yeganehdoust, R. Attarzadeh, A. Dolatabadi, and I. Karimfazli. “A comparison of bioinspired slippery and superhydrophobic surfaces: Micro-droplet impact”. In: *Physics of Fluids* 33.2 (2021), p. 022105.

[167] D. Waldbillig and O. Kesler. “Effect of suspension plasma spraying process parameters on YSZ coating microstructure and permeability”. In: *Surface and Coatings Technology* 205.23-24 (2011), pp. 5483–5492.

[168] H. Jazaerli. “Development of Slippery Liquid-Infused Porous Surfaces (SLIPS) using Suspension Plasma Spray”. PhD thesis. Concordia University, 2019.

[169] J. Smagorinsky. “General circulation experiments with the primitive equations: I. The basic experiment”. In: *Monthly weather review* 91.3 (1963), pp. 99–164.

[170] J. W. Deardorff et al. “A numerical study of three-dimensional turbulent channel flow at large Reynolds numbers”. In: *J. Fluid Mech* 41.2 (1970), pp. 453–480.

[171] K. Yokoi, D. Vadillo, J. Hinch, and I. Hutchings. “Numerical studies of the influence of the dynamic contact angle on a droplet impacting on a dry surface”. In: *Physics of Fluids* 21.7 (2009), p. 072102.